National Transportation Safety Board
Office of Research and Engineering
Washington, DC 20594

PLD22FR002

MATERIALS LABORATORY

Factual Report 22-038

September 25, 2023

(This page intentionally left blank)

A. ACCIDENT INFORMATION

Location:	Edwardsville, Illinois
Date:	March 11, 2022
Time:	8:15 central daylight time 14:15 coordinated universal time
Vehicle:	Marathon crude oil pipeline
Investigator:	Sara Lyons, RPH-20

B. COMPONENTS EXAMINED

Sections of crude oil pipeline

C. EXAMINATION PARTICIPANTS

Specialist	Erik Mueller, Ph.D., P.E. Office of Research and Engineering – Materials Laboratory Division NTSB, Washington, DC

D. DETAILS OF THE EXAMINATION

On March 11, 2022, the Woodpat pipeline, a 22-inch-diameter hazardous liquids pipeline operated by Marathon Pipe Line, LLC (Marathon), ruptured in Edwardsville, IL. About 3500 barrels of crude oil were released, some of which entered Cahokia Creek, a tributary of the Mississippi River. No injuries occurred, and the crude oil did not ignite.

The Woodpat pipeline was constructed in 1949 and purchased by Marathon in 1968. The pipeline pressure immediately before the rupture was about 479 psig, under the maximum operating pressure of 881 psig. At the time of the incident, the pipeline was being used to transport a batch of heavy, sour crude oil. Prior to the rupture, there were no noted issues or alarms with the batch movement, and no evidence was found to indicate any outside parties were near the rupture site at the time of the accident.

Previous in-line inspections and field studies performed for Marathon by various contractors had identified erosion, pipeline movement, and soil subsidence near the rupture site. The pipeline was most recently hydrostatically tested in 2018.

While on scene, NTSB investigators observed complete circumferential separation at a girth weld at the rupture origin. The NTSB retained both sides of the fractured girth weld and an adjacent section of girth weld as evidence for laboratory testing. These pipe sections, labeled Pipe 1, Pipe 2, and Pipe 3 for this report, were first sent to the

NTSB Materials Laboratory. Destructive testing was performed at DNV per a contract awarded by the NTSB.[1] The details of these results are outlined in this report.

1.1 Initial Visual Observations

Figure 1 and Figure 2 show the two mating pipeline sections about the fractured girth weld. These figures show Pipe 1 and Pipe 2, respectively. These figures are annotated at DNV, with the four prominent clock positions (12, 3, 6, and 9 o'clock) written directly on the pipe surfaces, along with the product flow direction at the time of the accident (towards the right). The 12 o'clock position is equivalent to top dead center. The Pipe 1 and Pipe 2 segments each measured approximately 52 inches long.

Figure 3 through Figure 6 show the mating sides of the girth weld that fractured between Pipe 1 and Pipe 2. The fracture, viewed from the outer diameter surface, shows the fracture occurred along the girth weld without extending into the pipe plate material. In most of the circumference, the fracture was present along the midline of the weld, as exemplified in Figure 4. The fracture exhibited sharp, jagged edges, with the most prominent areas being in Figure 3 and Figure 5, where the fracture was located toward the side of the heat affected zone. Figure 7 shows an angled view of this fractured region, with the fracture located toward either the side with Pipe 1 or the side with Pipe 2.

Figure 7 through Figure 9 show some of the areas marked for later sectioning. These specimens were later examined in optical or electron microscopy. Figure 10 through Figure 14 show selected fracture surface areas from the Pipe 1 side. These figures demonstrate some of the more typical features present on the fracture. Typically, the surface along the fractured girth weld exhibited a rough, fibrous texture with areas of localized ductile tearing and shear lips. The surface showed a dull luster.

A visual inspection of the pipe exterior surfaces was performed by a certified American Welding Society (AWS) inspector. The noted visual indications are tabulated in Table I. These describe the types and locations of several kinds of features, some of which are described in API 1104, which were:[2]

- Arc strike: areas where the weld arc made excessive electrical contact with the base metal and filler, resulting in underlying deposits, typically from excessive weld starts/stops
- Undercut: a depression of notch formed at the toe of a weld
- Low cap: areas where the weld face is below the weld toe (not described in API 1104)

[1] DNV (Det Norske Veritas) is an international accredited registrar and classification society headquartered in Høvik, Norway, with the Dublin, OH, USA facility performing the testing and evaluation for this investigation.
[2] API 1104 – *Welding of Pipelines and Related Facilities*, published by the American Petroleum Institute, headquartered in Washington, DC.

- Repair: areas consistent with previous weld repairs after initial joining of the pipe (not described in API 1104)
- Excessive cap height: areas where the weld face extended far above and over the weld toe (not described in API 1104)

1.2 Coating Evaluation

Figure 15 and Figure 16 show closer views of the exterior coating on the Pipe 1 and 2 sections. This coating, exhibiting a rough-textured light and tan coloring, was consistent with the asbestos-based coating applied at the installation date. The areas outlined in chalk on the coatings in the figures were later sectioned and removed to confirm the composition and makeup of the coating.

The coating was visually examined and then later tested using Fourier-transform infrared spectroscopy (FTIR) performed at PSN Labs.[3] Figure 17 shows a typical spectrum of the base material, exhibiting peaks consistent with a type of coal tar, based on the following peak wavenumbers:

- C-H stretching: 3048 and 3034 cm^{-1}
- C-H bending, out of plane: 882, 840, 813, 746 and 618 cm^{-1}
- C-H rocking: 718 cm^{-1}

The dispersion was consistent with chrysotile, a type of asbestos. The asbestos content was confirmed to be 5% of the coating volume.

The thickness of the coating was examined on both the Pipe 1 and Pipe 2 sections using a magnetic and eddy current detector. The results are summarized in Table II. In addition, the coating was examined for holidays, or areas where the coating was absent, breached, or nonadherent to the pipe outer surface. The results from the direct current detector are summarized in Table III, and show more discrepancies (12) with the coating on the downstream Pipe 2 section, versus the single holiday detected on the upstream Pipe 1 section.

1.3 Dimensional Measurements and Laser Scanning

The dimensions of the pipe sections were measured both manually using ultrasonic and manual thickness gauges, as well as from using laser scanning with a FAROArm scanning instrument. Of note were the thicknesses of the pipe sections and the outer diameter consistency to determine if the pipe exhibited significant out-of-round or concentricity issues.

[3] PSN Labs is a design, processing, and testing laboratory based in Erie, PA.

Table IV shows more of the circumference measurements of the pipe sections at their respective upstream and downstream ends. Note that the upstream end of Pipe 2 and the downstream end of Pipe 1 were the fracture girth weld faces. The outside diameter of the pipe ranged from 22.0 to 22.1 inches.

Figure 18 shows the laser scanned outside diameter measurements of the pipe ends near the fracture surface. This scan found diameter measurements from 21.839 inches to 22.119 inches. The diameter measurements in the vertical and horizontal directions (12 to 6 o'clock and 9 to 3 o'clock, respectively) were slightly longer than those in the 45° degree diagonals, being about 0.12 inches longer (22.02 average inches versus 21.90 average inches). These data were consistent with that collected from manual measurements in Table IV.

Figure 19 illustrates a topographical thickness map of the side of Pipe segments 1 and 2 about the fractured girth weld. The thicknesses ranged between 0.31 inches and 0.45 inches, with the thickest areas being along the fractured girth weld and intact seam welds (represented by yellow, orange, and red colors). The thinnest areas, represented by pink/purple, were at the fracture surface and pipe ends. The mean thickness on much of the pipe ranged between 0.341 and 0.347 inches. These data were within the range of the manual measurements of the pipeline thickness (after coating removal), detailed in Table V.

Figure 20 shows the circumferential wall thickness within 2 inches of the fracture surface, based on the pipe clock positions, from the Pipe 1 (upstream) and Pipe 2 (downstream) sides. Pipe 1 exhibited the greatest deviations from the nominal wall thickness (NWT) of 0.344 inches. The data showed lower thicknesses than NWT around the 6 o'clock and 12'oclock positions, with higher thicknesses near the 9 o'clock and 2 o'clock locations.

1.4 Mechanical and Chemical Testing

Chemical composition was determined by performing at NSL Analytical using optical emission spectroscopy (OES) with the carbon and sulfur analyzed with a separate LECO combustion method.[4] The chemical composition details for all three pipe sections are listed in Table VI. In summary, the chemical composition was consistent with the prescribed alloy of API 5L X46, based on the first API edition that specified chemical and mechanical property requirements for grade X46 pipe (5th edition, November 1954).

Table VII shows the chemical composition information for specimens across the fractured girth weld from the Pipe 2 section and the intact girth weld of Pipe 3 section. There were no requirements for the weld filler metal in these areas, but the

[4] NSL Analytical is an analytical and materials testing laboratory in Warrensville Heights, OH.

results were consistent with requirements for the pipe metal, and did not exhibit elevated concentrations of deleterious elements such as S or P.

Figure 21 through Figure 23 show some of the areas marked for extraction to develop specimens for mechanical testing, which were performed at Welding Consultant, LLC.[5] These included:

- For each of the segments from Pipe 1 and Pipe 2:
  - Uniaxial tensile testing
    - Three 1.5-inch gage width plate type specimens each in the transverse direction, longitudinal direction, and across the seam weld
  - Charpy impact at six temperatures using three specimens each for:
    - Pipe body, notch aligned with the axial direction
    - Pipe body, notch aligned with the circumferential direction
    - Across seam weld
    - Across seam weld heat affected zone (HAZ)
- For the segment from Pipe 3:
  - Uniaxial tensile testing
    - Three 1.5-inch gage width plate type specimens each in the transverse direction, longitudinal direction, and across the seam weld

Table VIII shows the tensile tests from the circumferential and longitudinal sections of base metal from Pipe sections 1, 2, and 3. Table IX shows the tensile strength only of specimens extracted across the seam welds from Highlighting the results from Pipe 2, the yield strength averaged 59.7 ksi in the transverse direction and 55.0 ksi in the axial direction. The respective tensile strengths in the transverse and axial directions were 88.5 and 87.2 ksi. The elongations were all over 28%. The tensile specimens across the seam exhibited comparable results, with the yield strength, tensile strength, and elongation averaging 58.4 ksi, 87.4 ksi, and 29.2%, respectively.

These data exceed the minimum requirements of this thickness of API 5L X46 pipe applicable for the year of pipe manufacture, which are:

- Yield strength = 46.4 ksi
- Tensile strength = 63.1 ksi
- % Elongation = 26.2 %

Microindentation hardness testing was performed across some of the fractured welds, to determine if there were significant hardness differences in either the weld

[5] Welding Consultants, LLC is an engineering and materials testing company located in Columbus, OH.

filler or heat-affected zones (HAZ). Figure 24 shows a cross section with hardness results, varying from 168 HV_{500} in the weld filler to 256 HV_{500} in the adjacent HAZ. The hardness in the base metal averaged 200 HV_{500}.

The Charpy V-notch testing data are compiled in Appendix A.

1.5 Visual Examination of the Girth Weld Fracture (Pipe 1 and 2)

Figure 25 shows the entire fracture surface of the girth weld, viewed from the Pipe 2 mating surface. Figure 26 through Figure 33 show closer views, at circumferential intervals approximately 8 inches per image, rotated clockwise through 360° of the fracture surface, starting at the 12 o'clock position in Figure 26.

Overall, these figures showed a dull luster and rough texture. As typified in Figure 26 and Figure 31, much of the fracture surface exhibited outwardly protruding shear lips, with a more recessed or flatter region along the centerline. Repeated jagged tearing features were present, as seen in Figure 28. These tearing marks were more concentrated on the 3 o'clock side of the pipe, as shown in Figure 27 and Figure 28. The inner area of the fracture surface between the 9 and 12 o'clock locations exhibited some protruding regions, which were more pronounced than but still consistent with the shear lip morphology seen elsewhere.

Figure 26 exhibited a pronounced fracture surface breaking feature located at the top dead center or 12 o'clock position. This feature appeared visually dark against the surrounding, maroon-colored fracture surface. This area was examined further in higher magnification scanning electron microscopy and cross-sectional metallography, locations denoted on the Figure 26.

1.6 Metallographic Examination of the Girth Weld Fracture (Pipe 1 and 2)

Several cross-sections were taken through areas of the mating fracture surfaces, as identified in Figure 3 through Figure 6. One such site, identified as M0_6a, is illustrated in Figure 34. This area shows a pipeline fracture to the left of the girth weld, with a second crack terminating under the top weld pass. This crack and the fracture exhibited features consistent with originating at the inner diameter surface (bottom of Figure 34). This crack to the right of the fracture in Figure 34 was located between the weld metal and the base metal, which exhibited a heat-affected zone typical of weld processes.

Figure 35 shows a closer view of the inner surface at M0_6a, showing smaller branched cracks emanating from the primary and second fractures. This location was around the 1 o'clock position of the fractured girth weld. Both these branching cracks had terminated at the lower surface of the outer weld pass. These features were consistent with a location lack of fusion at this location.

A closer view of the branch crack on the right showed it contained non-reflective material, consistent with nonmetallic compounds (Figure 36). These compounds exhibited a dendritic morphology, indicating they had solidified from a molten state. This morphology would be consistent with forming during welding, typical of slag formation.

Figure 37 shows the fracture cross-section at the girth weld location M0_6b, located just counterclockwise of the long seam weld that intersected the fractured girth weld (see Figure 3). This area also exhibited a fracture toward the side of the outer weld pass, with a secondary crack that terminated below the weld, located within the weld bead about 0.5 mm from the boundary between the weld and the heat affected zone. In this case, though, the second crack branched off the main fracture. Figure 38 shows a closer view of the fracture and the branching crack from the inner surface edge.

There was also a change in contrast around the area, consistent with microstructural changes from welding. Figure 39 shows an area near the crack face. The microstructure consisted of a ferrite/pearlite mixture oriented linearly in the longitudinal pipe direction. The fracture surface on the figure's left exhibited undulating nonmetallic layers, consistent with surface oxidation. Figure 40 shows the difference in the weld filler metal and the heat-affected base metal, with the base metal exhibiting more carbon-rich phases, consistent with its higher carbon content. This oxide layer on the fracture face was inconsistent with the nonmetallic material near the weld (Figure 41, from the upper left in Figure 38). This nonmetallic material exhibited a dendritic structure, indicating that it has solidified from a molten condition. These features were consistent with slag formed during welding.

Figure 42 shows a cross-section of the fractured weld at M0_6c, located just clockwise of the seam weld shown in Figure 3. This fracture completely bisected the weld filler, with a perpendicular orientation near the inner surface (figure bottom) and a curved, angled direction along the outer weld bead. Figure 43 shows the fracture on the inner side of the pipeline. This side of the fracture exhibited nonmetallic material along part of the surface closest toward the inner surface. This oxide was not layered but rather blocky and located at discontinuities in the metal surface.

Figure 44 shows a closer view of these nonmetallic materials, annotated to show their depth from the inner surface. The larger blocky oxide in the figure was 717 μm (0.028 in) from the surface, whereas the outermost oxide was found at 1.41 mm (0.056 in). Figure 45 shows a closer view of the oxide, exhibiting an alternating contrast consistent with a dendritic structure indicative of slag solidifying from the molten weld deposits. The slag manifest between the innermost weld bead and the base metal. These features were consistent with incomplete fusion at this location.

Figure 46 shows the fracture through weld location M1_5a, denoted in Figure 4 near some detected undercut around the 4 o'clock position. This fracture morphology was more angled, perpendicular to the pipe circumferential direction toward the inner surface. Figure 47 shows this inner surface corner of the fracture, along with an internal triangular-shaped feature. Figure 48 shows a closer view of the interior corner of the fracture, exhibiting rounded laps from the welding process and vertical discontinuities consistent with cracking. The crack was present between weld passes and had emanated from a pit-like feature on the interior, which exhibited nonmetallic material. The fracture surface also revealed nonmetallic material on the surfaces near the inner pipe surface, most notably on the right mating side in Figure 48.

The internal feature in location M1_5a is highlighted in Figure 49, showing its triangular and rounded compound shape. This feature exhibited black and dark gray areas consistent with void space and nonmetallic material, respectively. These features were consistent with porosity and nonmetallic slag that had formed during the welding process. Several cracks emanated from the void, as highlighted in Figure 50 the largest one. This crack had developed, growing inward in a transgranular manner. Figure 51 shows a closer view of the nonmetallic material, revealing a dendritic structure. This structure was consistent with solidification from a molten state, consistent with slag created during the welding process.

Figure 52 shows the fractured weld at location M1_5b, several inches clockwise of M1_5a. The location of this fracture was biased toward one side of the weld, located on the right in the figure. Figure 53 shows a montage of the inner part of the crack, which was located along one of the weld pass boundaries, except for a small area in the lower right. The figure also demonstrates the changing microstructure from the welding process. As indicated in Figure 54, the fracture surfaces exhibited a thin nonmetallic oxide layer, with blocky material area near the weld's inner surface. Figure 55 shows a closer view of this oxide, exhibiting a dendritic morphology. Figure 55 also shows the difference in microstructure between the weld and the HAZ, with the former exhibiting more ferrite and an acicular morphology of the carbon-rich phase and the latter having more cementite present.

Figure 56 shows the fracture of the weld at location M4_3, near the 9 o'clock position illustrated in Figure 6. This fracture exhibited a zig-zag morphology, consistent with much of the girth weld fracture exhibiting shear lips and a recessed center (see Figure 31 and Figure 32). As shown in Figure 56, this weld exhibited a lack of cap fill on the exterior, contoured consistent with the individual weld passes in that area. Figure 57 shows an elongated inclusion just outside one of the weld passes. Unlike the other slag deposits, this feature exhibited a more metallic, optically reflective quality.

Figure 58 shows a closer view of the inner diameter edge of the fracture surface, showing base metal on both sides of the fracture, indicating fracture through the

base metal, rather than solely along the interface with the weld as seen previously. Figure 59 shows a longitudinally-oriented inclusion, consistent with a manganese sulfide constituent. While near the weld, this was not located at the fracture in this location.

Figure 60 illustrates the fracture of the weld at location M5_2, located near the 11 o'clock position shown in Figure 6. The fracture location was nearly perpendicular to the pipe along the weld centerline but also exhibited a discernible crack that was present through the innermost third of the pipe thickness. Figure 61 shows a closer view of this crack alongside the inner surface corner of the fracture. The crack and fracture exhibited thin layers of nonmetallic material along the surface, consistent with oxidation after opening to the environment. The crack extended towards the lower area of the primary weld pass, measured as 2.08 mm (0.082 in).

Figure 62 shows a cross section parallel to the direction of the girth weld, taken at location M2C. This figure demonstrates the multiple weld passes performed on the girth weld. This figures also illustrates some porosity and entrained slag material between the root pass and the hot pass on the figure's lower left.

1.7 Metallographic Examination of Pipe 1 and Pipe 2 Seam Welds

Figure 63 shows a cross-section through the intact long seam weld in the Pipe 1 section. In contrast to the fractured girth welds, this long seam weld exhibited an hourglass-center, with triangular lighter regions on either side. This pattern was consistent with the reported electric resistance weld (ERW) rather than the manual shielded metal arc welds (SMAW) of the girth welds. As shown in the figure, the weld reinforcement had not been ground or machined (also known as scarf) below the pipe thickness on either side.

Figure 64 shows a typical area of the weld microstructure, elongated ferrite with more equiaxed pearlitic regions in between. In the adjacent heat-affected zone, however, the microstructure exhibited more ferrite, which, while elongated, was more equiaxed in morphology (Figure 65). The amount of pearlite was less than in the weld regions.

The seam weld along in the Pipe 2 section was cross sectioned and mounted, identified as MS_2. This seam weld is illustrated in Figure 66. The weld area exhibited a more needle-like ferrite morphology (Figure 67) than in the heat-affected zone, with more equiaxed pearlite/cementite (Figure 68). These morphological differences delineated the welded and base metal regions. In two of the figures, there were small nonmetallic compounds or inclusions, with small microcracks emanating from them (Figure 64 and Figure 67). These features were smaller than 50 μm (0.002 in).

1.8 Scanning Electron Microscopy of the Fractured Girth Weld

Selected areas of the girth weld fracture surface were examined to discern fracture features that would indicate the fracture mode. These features were cleaned sequentially with acetone, Alconox, and then Presolve.[6] This process facilitated the examination of the nascent and underlying fracture features. Figure 69 shows one such area, extracted from near the seam weld intersections in Figure 3, after cleaning with the degreasing agent. Much of the fracture surface exhibited a rough texture with a dull luster—these characteristics were consistent with overstress fracture of a ductile material. However, there were isolated areas with flatter, more reflective features, examined further as described below.

This specimen was examined using a scanning electron microscope (SEM). Figure 70 shows one area which exhibited a more reflective and flatter area. Figure 71 shows a closer view of the area, delineating between an inner and outer fracture area. Figure 72 shows a closer view of the transition area, where the outer (upper in the figure) portion exhibited dimpled rupture, consistent with ductile overstress fracture. The inner area revealed more elongated dimpled features and cleavage facets.

Several micrographs were taken to examine the inner portion of this fracture, located where annotated in Figure 74. Figure 75 shows a region nearest to the inner surface corner of the fracture surface. Much of the area exhibited surface oxidation, as demonstrated by Figure 76 and Figure 77. The oxide in this area exhibited sharp acicular layered features and more rounded globules. These morphologies were consistent with post-fracture oxidation and were thick enough to obscure the underlying fracture features. These features were consistent throughout this portion of the fracture surface.

Figure 78 shows another area on the fracture surface that exhibited a flatter, more reflective area on the inner surface corner. This thumbnail-shaped region measured about 6 mm by 3 mm (0.22 in by 0.11 in). The area was examined before and after final surface oxide removal, and the location of the micrographs taken are annotated in Figure 79 and Figure 80 for those conditions, respectively.

Figure 81 shows some of the different surface oxide morphologies on the fracture surface, with areas of small globular features in the top of the figure, and more pronounced, acicular features in the bottom. This figure was taken from the corner protruding outward in Figure 79. Neither of these oxide patterns were consistent with known underlying fracture features. Figure 82 shows the same area after oxide

[6] Alconox is a powdered cleaning detergent, containing primarily sodium bicarbonate and sodium alkylbenzene sulfonate, manufactured by Alconox, Inc., White Plains, NY. LPS Presolve Orange is an aerosol degreasing agent comprised of mineral spirits and d-limonene manufactured by LPS Laboratories, headquartered in Tucker, GA.

removal. While some of the pock-marked features were consistent with dimpled rupture, many divots were consistent with artifacts of removing the surface layer.

Figure 83 shows an area of the thumbnail feature near its edge. The figure shows an area of dimpled rupture in the upper right. After cleaning, the area appeared similar to the previous location, exhibiting underlying pockmarked features (Figure 84). Similar features were revealed in an upper area of the clamshell feature (location 13) after oxide removal. The surface showed pock marks and features consistent with underlying dimpled rupture. Figure 85 shows a nearby location post cleaning, which also exhibited the pock-mark surface morphology consistent with post-fracture corrosive attack.

The figure also displays isolated areas of parallel, linear features. These features were inconsistent with other areas and exhibited a slightly rounded morphology. These linear features were consistent with the underlying lamellar features of the pearlitic and ferritic microstructure of the weld filler. A closer view of another area with isolated linear features is illustrated in Figure 86. This shows small angles and dimples, along with localized ductile tearing. These features were consistent with overstress fracture being influenced by the microstructure of the weld where this part of the fracture had occurred.

Overall, the fracture features of the fractured girth weld between Pipe 1 and Pipe 2 exhibited characteristics consistent with overstress fracture. Most of the fractured weld was consistent with fracture from the inner surface outward, consistent with axial tensile forces along the inner surface. There were cracks at several locations along the inner surfaces of the welds. However, no features were observed on the fracture surfaces consistent with progressive cracking consistent with either fatigue or stress corrosion.

1.9 Examination of Pipe Section 3

The intact girth weld of the third pipe section was examined using radiography by a third-party contractor, Shaw Pipeline Services.[7] A montage of the complete girth weld radiographs is shown in Figure 87. This examination found areas of entrapped porosity, typically in linear concentrations of 4 to 45 inches in length. Other imperfections included:

- Burnthrough (BT): areas where the welding arc has too much penetration, resulting in molten metal pushing through the opposite surface
- Elongated slag inclusions (ESI): inclusions of nonmetallic slag entrained in the weld

[7] Shaw Pipeline Services is a subsidiary of Shawcor, Ltd., which performs ultrasonic and radiographic nondestructive testing, specializing in welds of pipelines.

- Incomplete fusion (IF): a lack of contact and joining (fusion) between the weld filler and the base metal
- Incomplete penetration (IP): areas with too little penetration, resulting in an incomplete weld leaving gaps between the joined areas in the root of the weld

Several cross-sections were taken through the girth weld in Pipe 3. Figure 88 shows a cross-section through the weld location of M3_1. This area reveals an intact weld exhibiting a lack of complete fusion. The incomplete fusion manifest as a branched crack along the inner surface corner, highlighted in Figure 89. Primarily located along the edges of the weld filler, the crack was as deep as 1.2 mm (0.047 in). The crack was filled with a nonmetallic material, consistent with oxide buildup from service since assembly. Figure 90 shows a closer view of the upper portion of the crack oxide, revealing a dendritic structure. This microstructure would be consistent with solidification from a molten state, indicative of welding slag.

Figure 91 shows a cross-section through a weld area that exhibited porosity in the radiographic inspection, labeled M3_2. This weld also shows a “high-low” mismatch between the opposite sides of the pipe joint. This mismatch was collocated with some uneven internal undercut features along the inner surface. The porosity, under 1 mm in diameter, was located within 1 to 2 mm of the outer surface of the weld.

Figure 92 shows a closer view of the inner surface of the weld at M3_2, showing the dendritic structure of the filler material and the adjacent cracks in the undercut area. The crack to the left of the weld filler had propagated to 0.16 mm (0.006 in), located along the transition between the filler and heat-affected pipe material. Figure 93 shows the tip of this crack, which had progressed in a transgranular manner. The crack also contained layered, concentric-appearing nonmetallic material consistent with surface oxide forming during crack growth.

Figure 94 shows another cross-section of the Pipe 3 weld, which exhibited a broader and deeper imperfection than in Figure 91, consistent with burn through. This location was labeled as M3_5. The amount of burn through was 5 mm by 3 mm deep (0.20 inch by 0.12 inches). Like the other imperfections of this girth weld, this cross-section showed outward-oriented sharp corners (Figure 95). However, these locations had not spawned cracks (see Figure 96). Figure 95 shows the right side of the weld filler transition to the heat-affected zone. This area exhibited some nonmetallic material, consistent with the buildup and oxidation of the metal of the pipe's inner surface.

Overall, examination of the girth weld in Pipe 3 revealed areas of incomplete welding, which displayed some cracking. The layered oxide in these cracks indicates they had been present before the accident.

Figure 97 shows a microindentation hardness map of the girth weld cross section of location M3_1. The map shows an increase in hardness values in the heat affected zone adjacent to the interface between the weld and base metal, located near the outer surface weld toes. In contrast, the center of the weld bead along the centerline exhibited the lowest hardness values. This cross-section location, however, did exhibit a root bead imperfection, which can influence the local properties of the weld and HAZ.

Submitted by:

Erik M. Mueller
Materials Research Engineer

Table I. Summary of visual features and imperfections identified on the external pipe surfaces of the fractured girth weld of Pipe sections 1 and 2, and the intact girth weld of Pipe section 3, as performed by an AWS certified inspector per API 1104.

Pipe Section	Visual Defects	Distance Clockwise from TDC (feet)		Circumferential Length (inch)	O'clock Orientations
		Start	Stop		
2	Arc Strike	1.00	1.03	0.36	2:05 - 2:09
1	Undercut	1.76	1.82	0.72	3:40 - 3:48
1	Undercut	2.25	2.42	2.04	4:41 - 5:03
2	Arc Strike	2.42	2.54	1.44	5:02 - 5:18
1	Undercut	2.81	2.83	0.24	5:51 - 5:54
2	Undercut	2.80	2.92	1.44	5:50 - 6:05
1	Undercut	3.04	3.10	0.72	6:20 - 6:28
1	Undercut	3.27	3.39	1.44	6:49 - 7:04
2	Undercut	3.30	3.40	1.20	6:53 - 7:05
1	Arc Strike	3.54	3.60	0.72	7:23 - 7:30
2	Low Cap	4.15	4.29	1.68	8:39 - 8:56
2	Arc Strike	4.16	4.22	0.72	8:40 - 8:47
1	Arc Strike	4.21	4.31	1.20	8:46 - 8:59
1	Repair	4.46	4.54	0.96	9:18 - 9:28
1	Arc Strike	4.85	5.01	1.92	10:06 - 10:26
2	Undercut	5.12	5.15	0.36	10:40 - 10:44
3	Arc Strike	2.08	2.20	1.44	4:20 - 4:35
3	Repair	2.16	2.26	1.20	4:30 - 4:43
3	Arc Strike	2.84	2.94	1.20	5:55 - 6:08
3	Low Cap	2.99	3.00	0.12	6:14 - 6:15
3	Excess Cap Width	3.02	3.32	3.60	6:17 - 6:55
3	Excess Cap Width	3.17	3.32	1.80	6:36 - 6:55
3	Undercut	3.18	3.20	0.24	6:38 - 6:40
3	Undercut	5.22	5.23	0.12	10:53 - 10:54

Table II. Coating thickness measurement performed on Pipe section 1 and Pipe Section 2 using a PosiTector 6000 Type 2 coating thickness gauge.

Pipe Section	Thickness Values at 5 o'clock orientations (inch)				
	12:00	3:00	6:00	9:00	10:30
1 (Performed 3.2 feet from Upstream Cut End)	0.2305	0.1680	0.1130	0.1775	0.1980
	0.2270	0.1970	0.1650	0.1900	0.2380
	0.2285	0.1775	0.1195	0.1825	0.1955
	0.2205	0.1705	0.1525	0.1820	0.2140
	0.2430	0.1790	0.1630	0.1840	0.1605
Average	**0.2299**	**0.1784**	**0.1426**	**0.1832**	**0.2012**
2 (Performed 3.2 feet from Upstream Girth Weld End)					
	0.0995	0.0890	0.0555	0.1365	0.0775
	0.1250	0.1165	0.1740	0.1150	0.0960
	0.0870	0.1005	0.0660	0.1100	0.0925
	0.1325	0.1275	0.0800	0.1065	0.0870
	0.0835	0.1350	0.1545	0.1425	0.0865
Average	**0.1055**	**0.1137**	**0.1060**	**0.1221**	**0.0879**

Table III. Summary of coating holiday locations of Pipe sections 1 and 2, performed using a high-voltage direct current holiday detector (Elcometer 266).

Pipe Section	Distance from Upstream End		Length (inch)	O' Clock Orientations	Width (inch)
	Upstream End	Downstream End			
1	2.99	3.76	9.24	11:23 - 12:44	7.75
2	0.51	1.09	6.96	11:21 - 12:54	8.91
2	0.90	4.30	40.80	12:00 - 1:46	10.20
2	0.44	2.01	18.80	2:45 - 4:44	11.40
2	2.12	3.19	12.80	2:29 - 4:28	11.40
2	3.19	3.68	5.88	4:13 - 4:49	3.36
2	1.69	2.08	4.68	5:54 - 8:55	17.40
2	2.08	4.28	26.40	6:33 - 8:55	13.60
2	1.17	2.09	11.00	9:33 - 10:41	6.50
2	1.90	2.03	1.56	9:09 - 9:29	1.92
2	2.24	4.17	23.20	9:47 - 10:24	3.48
2	2.75	2.92	2.04	10:24 - 10:39	1.44
2	2.82	2.91	1.08	9:05 - 9:15	0.60
2	3.10	3.35	3.00	10:26 - 10:54	2.64

Table IV. Results of the circumference and diameter measurements performed with a tape measure on the ends of the pipe sections. The tolerance from API 5LX (1st edition) were ±1%.

Pipe Section / Joint	Pipe Section End	Circumference (ft)	Diameter (inch)		
			From Circumference Measurement	3 to 9 o'clock	6 to 12 o'clock
1 / 29782	Upstream	5.79	22.1	22.0	22.0
	*Downstream**	5.75	22.0	22.0	22.0
2 / 29783	*Upstream**	5.76	22.0	22.0	22.0
	Downstream	5.78	22.1	22.0	22.0
3 / 29781	Upstream	5.78	22.1	22.0	22.0
	Downstream	5.79	22.1	22.0	22.0

Table V. Wall thickness measurement results performed by micrometers on the cut ends of the three pipe sections. The tolerance requirement from API 5LX (1st edition) was -12.5% from a minimum of 0.301 inches.

O'clock Orientation	Wall Thickness (inch)			
	Upstream end of Pipe 1 (JT 29782)	Downstream End of Pipe 2 (JT 29782)	Upstream end of Pipe 3 (JT 29781)	Downstream End of Pipe 3 (JT 29781)
12	0.349	0.346	0.352	0.352
3	0.351	0.341	0.352	0.352
6	0.349	0.340	0.350	0.351
9	0.348	0.344	0.351	0.352
Average	0.349	0.343	0.351	0.352

Table VI. Results of chemical analysis results from examination of specimens from Pipe sections 1, 2, and 3 using OES, and C and S results from C+S LECO furnace method. These results were compared to the requirements in the API 5LX 5th edition from November 1954, which was the first year tensile and chemical properties were specified for X46 pipe. The carbon equivalents were calculated based on the Dearden and O'Neill formula adopted by the IIW in 1967.

Element	Composition			
	API 5LX Grade X46	Pipe 1	Pipe 2	Pipe 3
C	0.31 (max)	0.273	0.265	0.275
S	0.005 (max)	0.018	0.021	0.022
Mn	1.45 (max)	1.065	1.108	1.102
P	0.04 (max)	0.024	0.032	0.028
Si		0.092	0.068	0.103
Cu		0.077	0.065	0.052
Sn		0.033	0.005	0.011
Ni		0.04	0.038	0.031
Cr		0.049	0.021	0.028
Mo		0.007	0.006	0.006
Al		0	0.001	0.004
V		0.003	0.004	0.003
Nb		0.001	0.001	0.001
Zr		0.001	0.001	0.001
Ti		0	0	0
B		0.0002	0.0002	0.0002
Ca		0.0001	0.0001	0.0001
Co		0.006	0.006	0.005
Fe	Balance	98.3107	98.3577	98.3277
CE_{IIW}		*0.470*	*0.463*	*0.472*
LECO C/S Furnace Method Data				
C	0.31 (max)	0.25	0.27	0.24
S	0.005 (max)	0.022	0.028	0.023

Table VII. Results of OES and chemical analyses of specimens removed from the fractured girth weld of Pipe 2 and the intact girth weld of Pipe 3, along with C and S results from C+S LECO furnace method. The carbon equivalents were calculated based on the Dearden and O'Neill formula adopted by the IIW in 1967.

Element	Composition		
	API 5LX Grade X46	Girth Weld, Pipe 2	Girth Weld, Pipe 3
C	0.31 (max)	0.182	0.146
S	0.005 (max)	0.029	0.026
Mn	1.45 (max)	0.563	0.621
P	0.04 (max)	0.015	0.016
Si		0.159	0.195
Cu		0.112	0.061
Sn		0.017	0.015
Ni		0.047	0.036
Cr		0.031	0.03
Mo		0.277	0.219
Al		0.002	0.001
V		0.003	0.003
Nb		0.003	0.002
Zr		0.002	0.001
Ti		0.012	0.014
B		0.0002	0.0002
Ca		0.0014	0.0002
Co		0.007	0.006
Fe	Balance	98.5374	98.6076
CE_{IIW}		*0.349*	*0.306*
LECO C/S Furnace Method Data			
C	0.31 (max)	0.12	0.23
S	0.005 (max)	0.026	0.024

Table VIII. Tensile test results in circumferential and longitudinal directions for Pipe Sections 1, 2, and 3, showing the individual specimen results, their averages, and requirements from API 5LX Grade X46 pipe from the 5th edition (November 1954).

Pipe 1	Circumferential Specimens				API 5LX Grade X46 Req.	Longitudinal Specimens			
	Specimen 1	Specimen 2	Specimen 3	Average		Specimen 1	Specimen 2	Specimen 3	Average
Yield Strength (ksi)	57.0	59.3	58.7	58.3	46 (min)	56.0	52.4	53.4	53.9
Tensile Strength (ksi)	83.9	84.2	84.6	84.2	63 (min)	83.6	83.2	83.7	83.5
Elongation in 2 in (%)	30.0	28.7	31.7	30.1	23.26 (min)	33.4	33.1	33.4	33.3
Reduction of Area (%)	42.4	41.6	44.8	42.9	--	56.6	54.6	49.6	53.6
Pipe 2	**Circumferential Specimens**				**API 5LX Grade X46 Req.**	**Longitudinal Specimens**			
	Specimen 1	Specimen 2	Specimen 3	Average		Specimen 1	Specimen 2	Specimen 3	Average
Yield Strength (ksi)	61.2	57.4	60.5	59.7	46 (min)	55.9	54.6	54.6	55.0
Tensile Strength (ksi)	89.4	87.9	88.3	88.5	63 (min)	86.7	87.4	87.5	87.2
Elongation in 2 in (%)	30.7	28.2	29.0	29.3	23.98 (min)	32.0	32.0	32.6	32.2
Reduction of Area (%)	44.3	39.3	40.1	41.3	--	50.6	51.8	52.2	51.6
Pipe 3	**Circumferential Specimens**				**API 5LX Grade X46 Req.**	**Longitudinal Specimens**			
	Specimen 1	Specimen 2	Specimen 3	Average		Specimen 1	Specimen 2	Specimen 3	Average
Yield Strength (ksi)	57.0	57.6	58.3	57.6	46 (min)	52.9	53.2	53.4	53.2
Tensile Strength (ksi)	82.6	82.8	82.7	82.7	63 (min)	82.0	82.2	82.2	82.1
Elongation in 2 in (%)	29.8	28.8	28.4	29.0	23.42 (min)	31.6	32.2	31.7	31.8
Reduction of Area (%)	39.9	37.5	41.2	39.5	--	52.9	50.4	41.6	48.3

Table IX. Tensile test results from specimens sectioned across longitudinal seam welds from Pipe sections 1, 2, and 3.

Pipe Section	Tensile Strength (ksi)			
	Specimen 1	Specimen 2	Specimen 3	Average
Pipe 1	87.9	87.7	88.1	87.9
Pipe 2	87.3	87.2	87.6	87.4
Pipe 3	88.4	87.9	88.0	88.1

Figure 1. Views of the Pipe 1 pipeline section from three different views, as received at DNV.

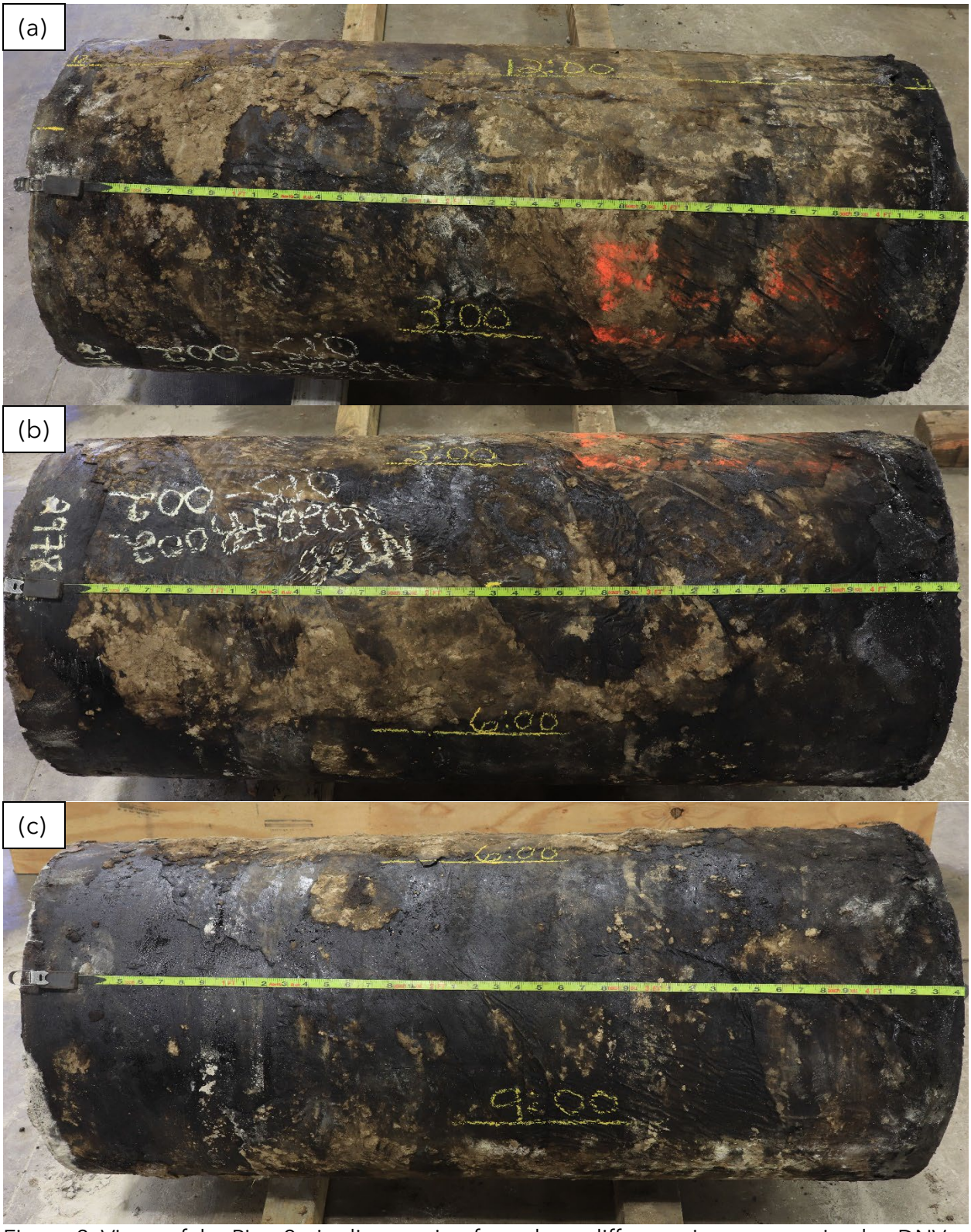

Figure 2. Views of the Pipe 2 pipeline section from three different views, as received at DNV.

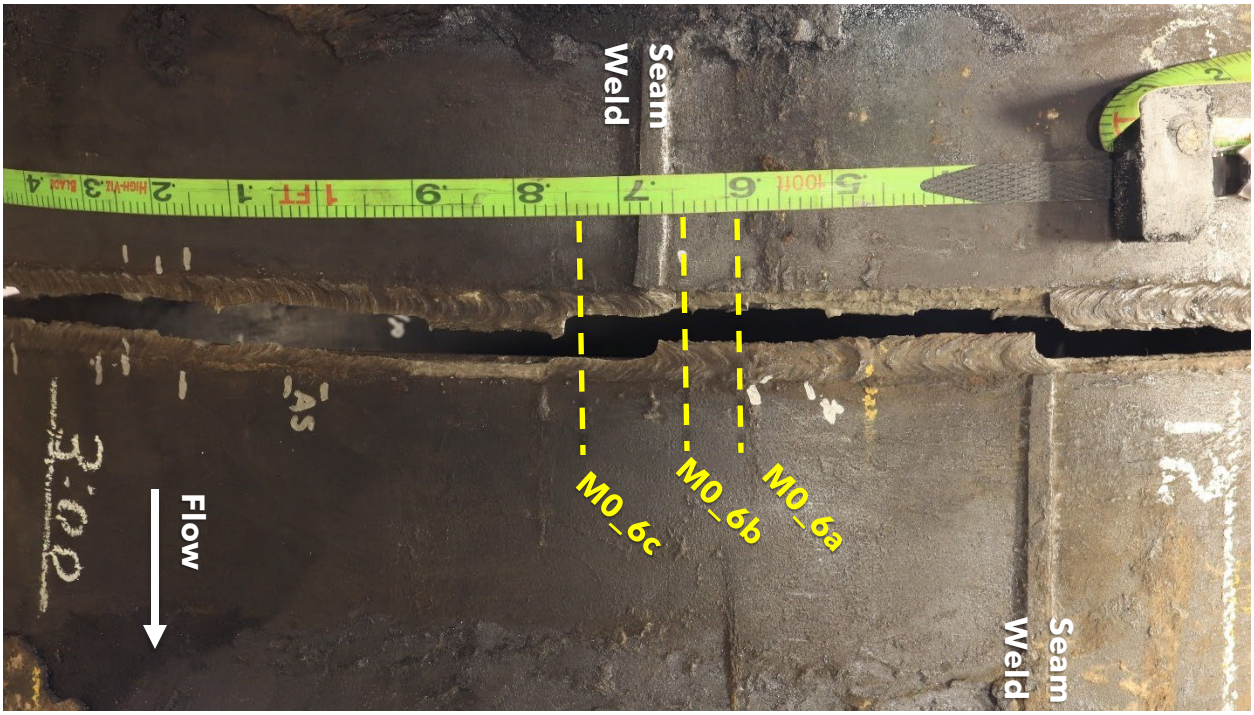

Figure 3. View of the mating fractured of Pipe 1 and 2 between the 3 and 12 o'clock position, showing a seam weld and the location of metallographic mount locations M0_6a, b, and c.

Figure 4. View of the mating fractured of Pipe 1 and 2 between the 6 and 3 o'clock positions, annotated to show metallographic mount locations and girth weld flaws: arc strike (AS) and undercut (UC).

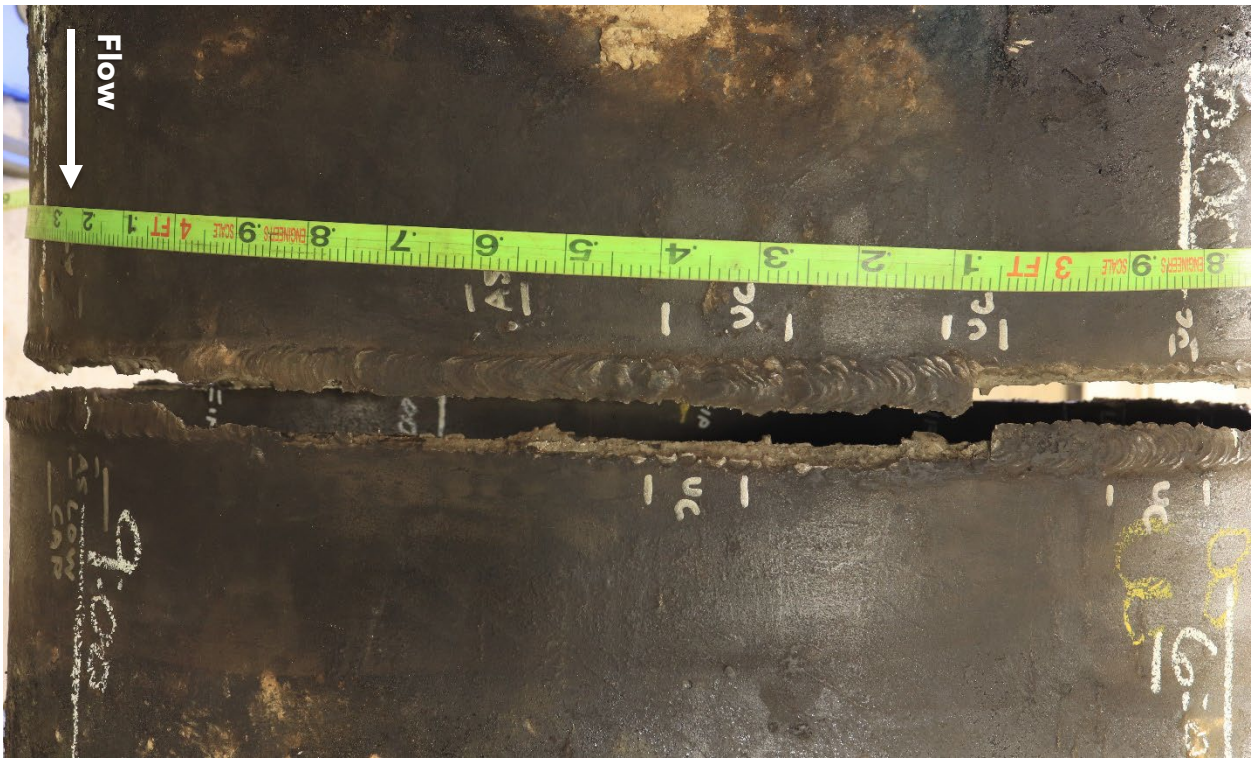

Figure 5. View of the mating fractured of Pipe 1 and 2 between the 9 and 6 o'clock position, annotated to show girth weld features, like arc strikes (AS) and undercut (UC).

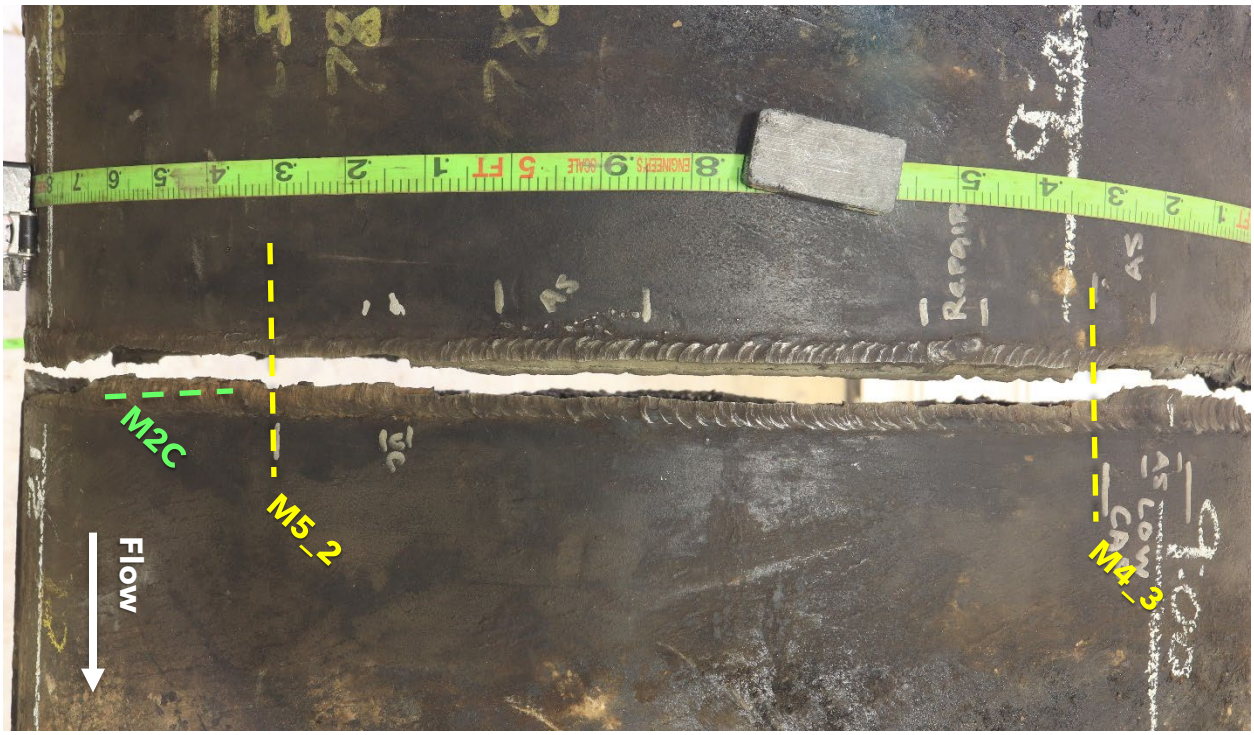

Figure 6. View of the mating fractured of Pipe 1 and 2 between the 12 and 9 o'clock position.

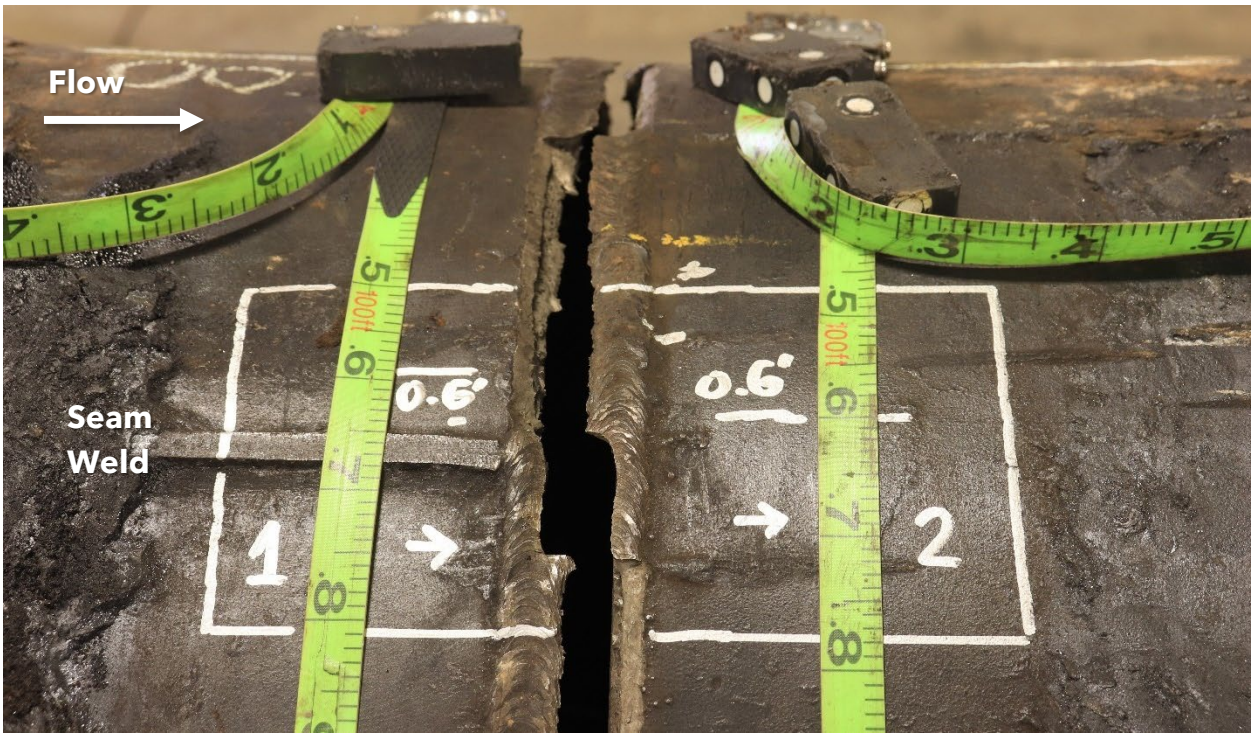

Figure 7. Mating fracture surfaces along the girth weld between Pipes 1 and 2, showing areas to be sectioned.

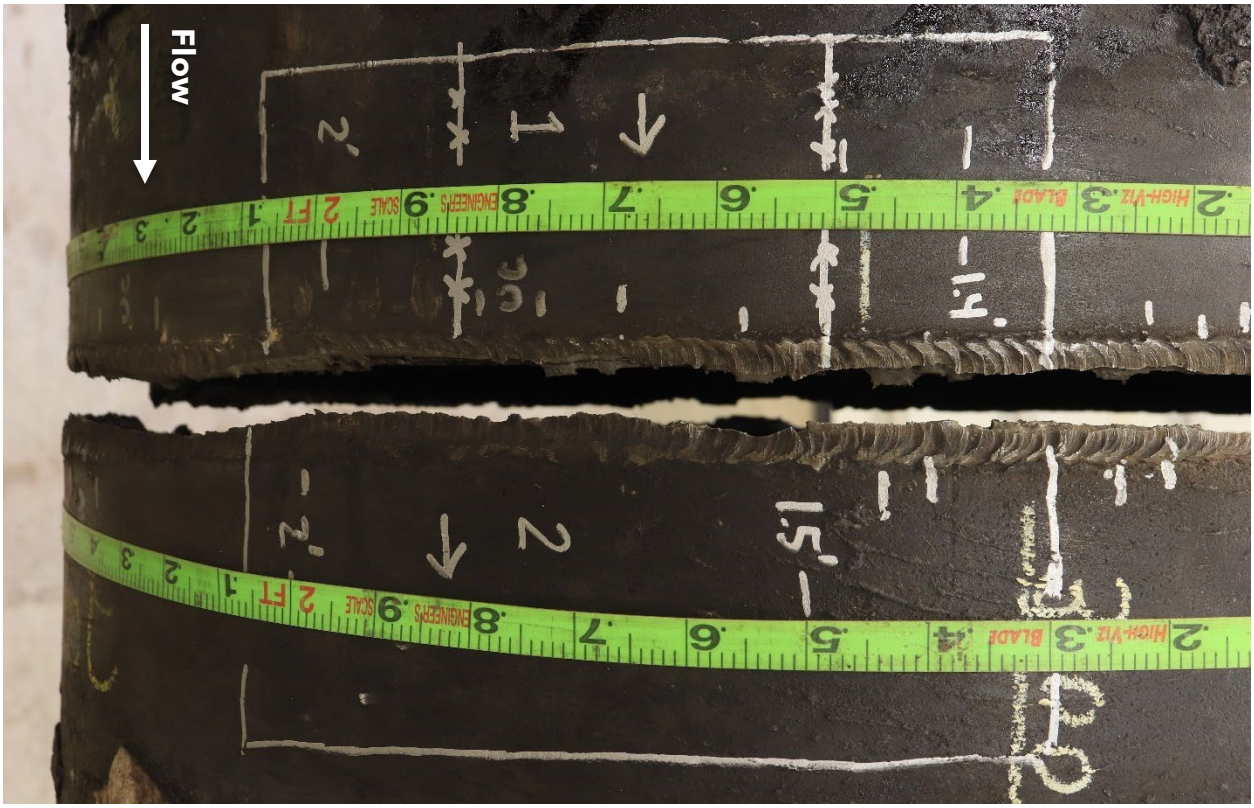

Figure 8. Mating fracture surfaces along the girth weld between Pipes 1 and 2, showing areas to be sectioned.

Figure 9. Mating fracture surfaces along the girth weld between Pipes 1 and 2, showing areas to be sectioned.

Figure 10. An (a) angled and (b) oblique view of an area of the Pipe 1 fracture surface annotated for sectioning.


Figure 11. An area of the Pipe 1 fracture surface annotated for sectioning.

Figure 12. An oblique view of an area of the Pipe 1 fracture surface annotated for sectioning.

Figure 13. An angled view of an area of the Pipe 1 fracture surface annotated for sectioning.

Figure 14. An (a) angled and (b) oblique view of an area of the Pipe 1 fracture surface annotated for sectioning.

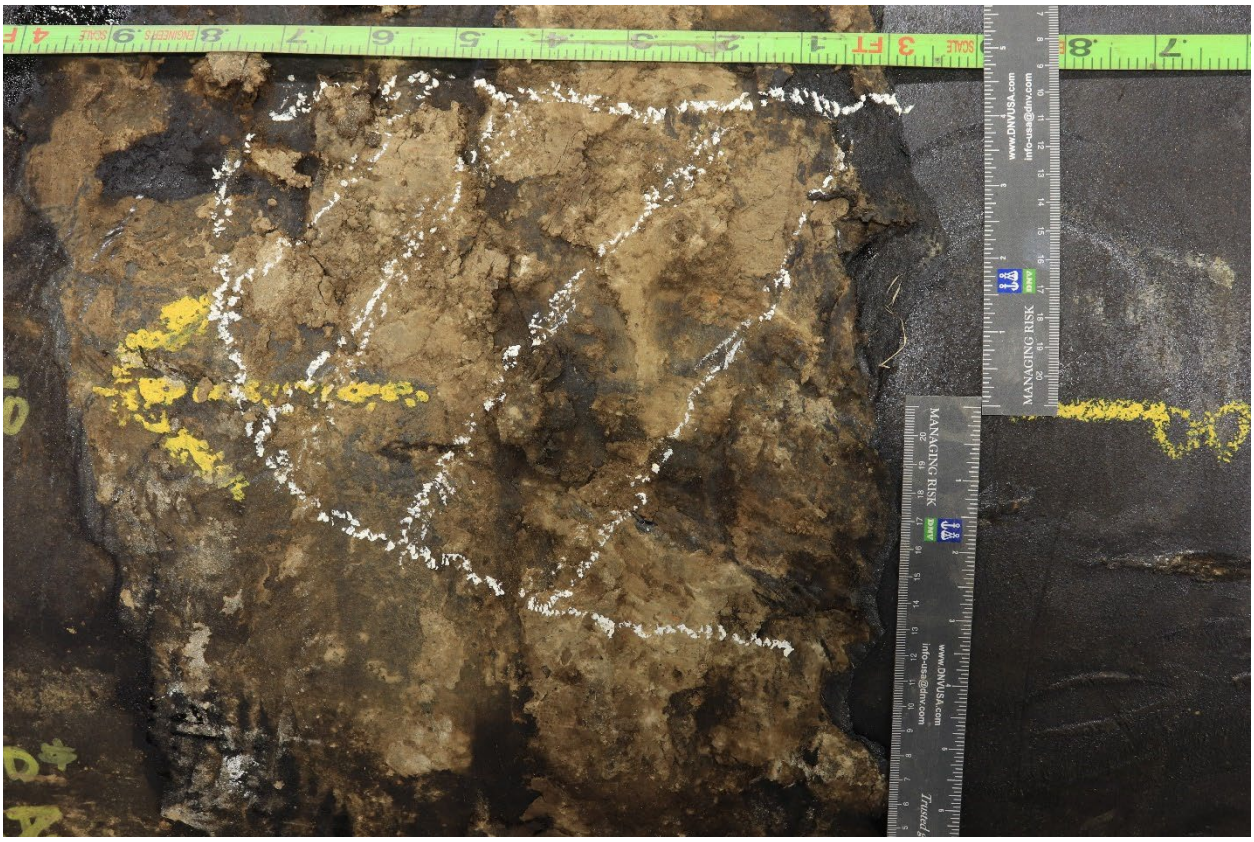

Figure 15. Area of the Pipe 1 showing locations of coating to be removed for examination.

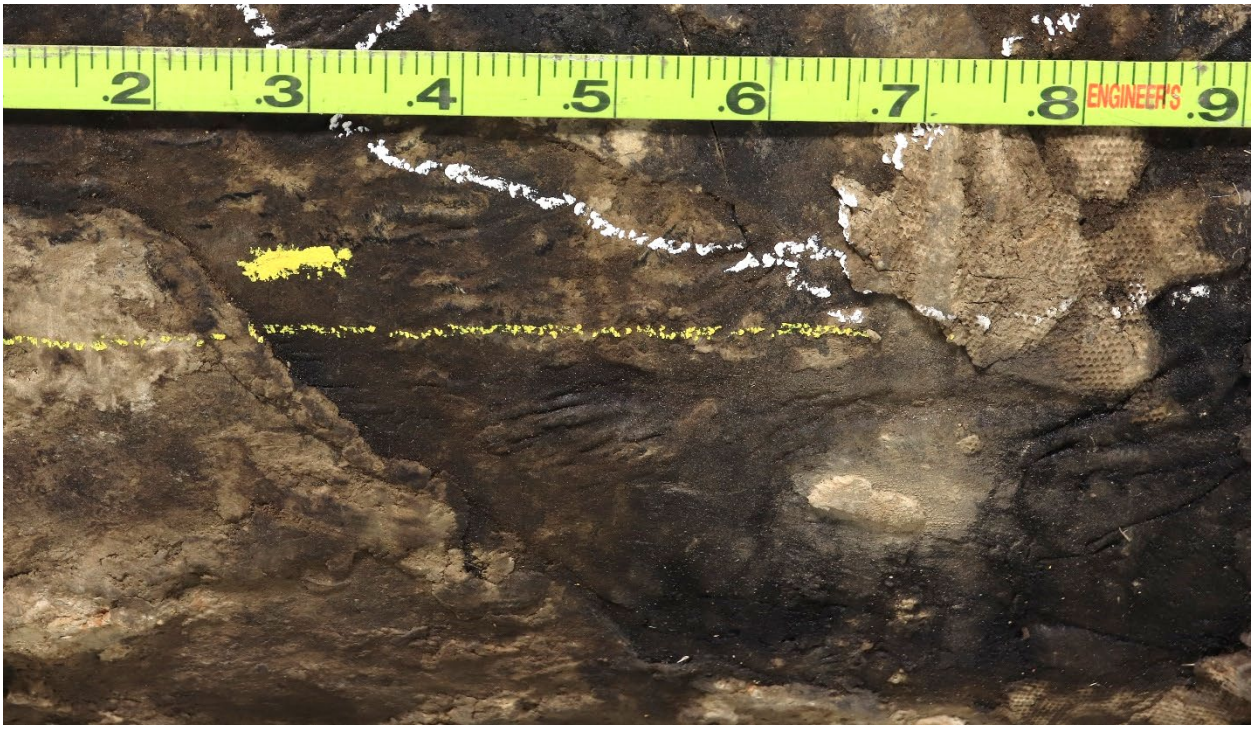

Figure 16. Area of the Pipe 2 showing locations of coating to be removed for examination.

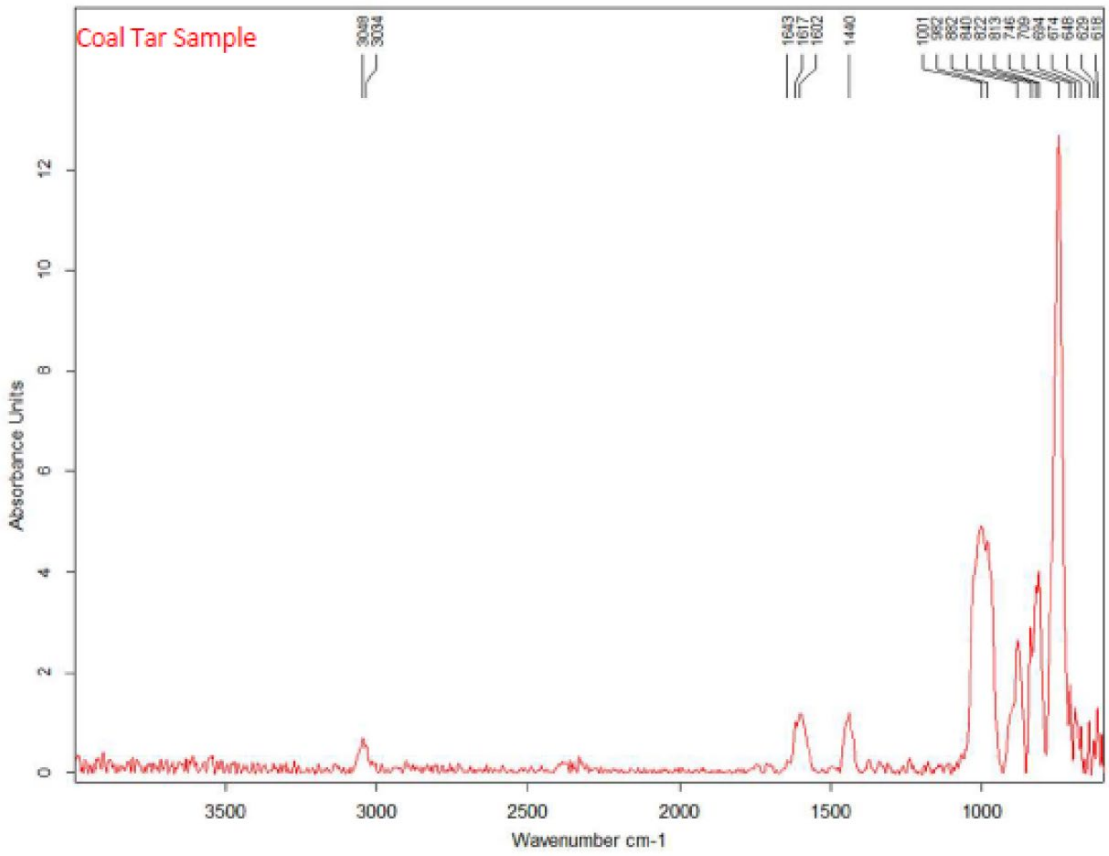

Figure 17. FTIR spectrum of a sample of the external coating removed from Pipe 2.

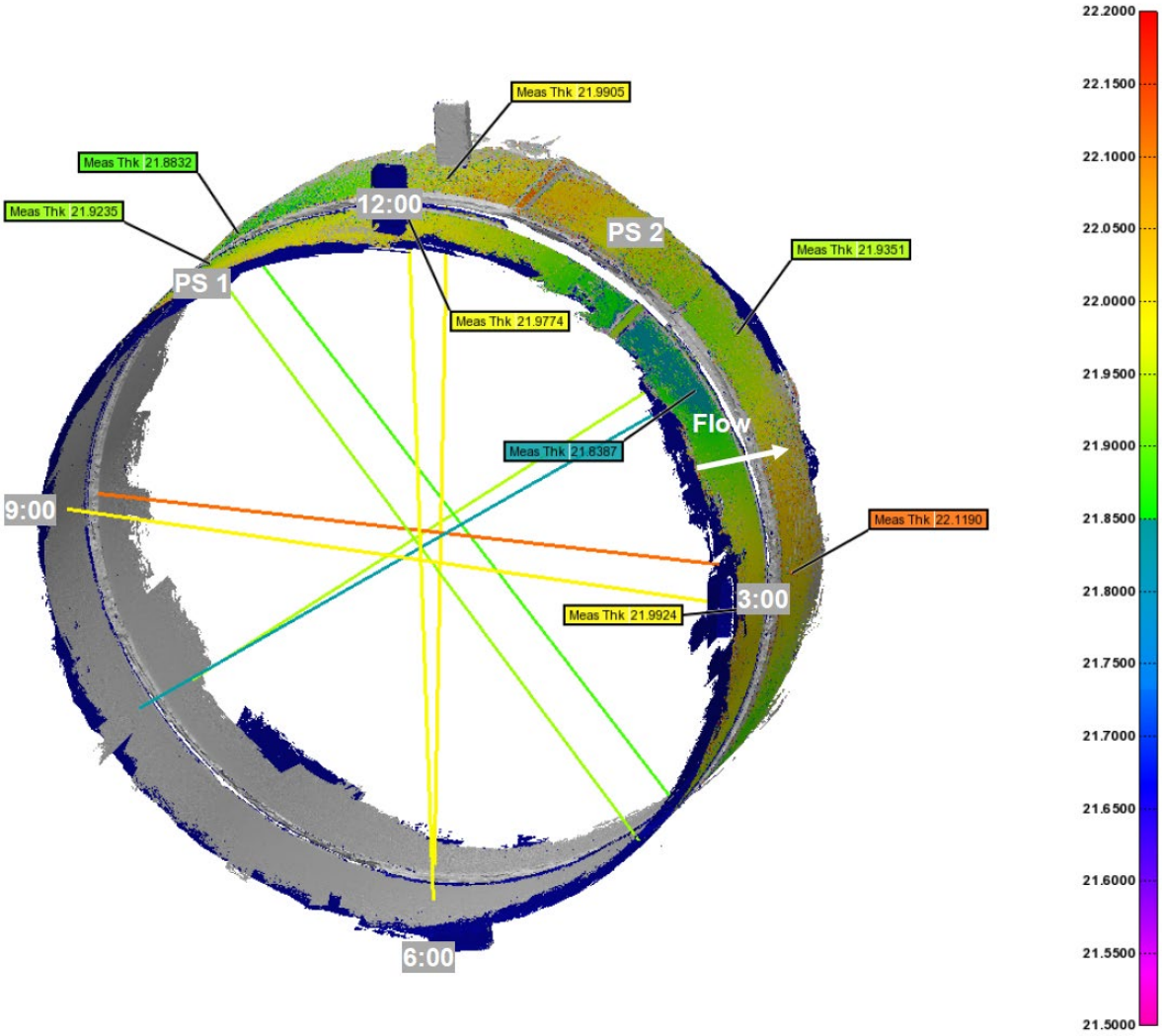

Figure 18. Outside diameter measurements in inches near the fracture surfaces between Pipe 1 and 2, based off laser scanning data. The color coding represents the diameter size from 21.5 to 22.2 inches, as denoted by the scale on the right.

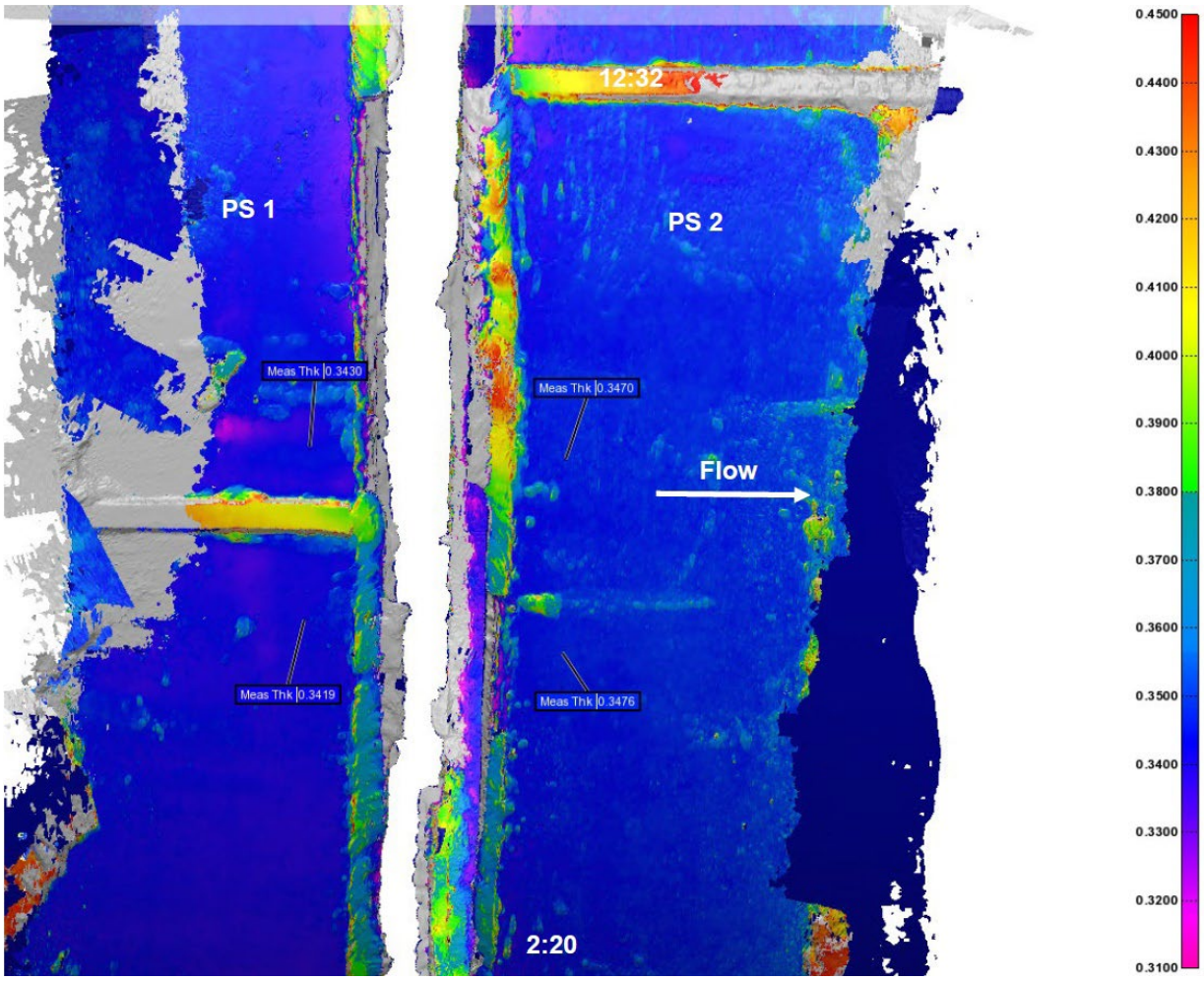

Figure 19. Thickness map representing Pipe 1 and Pipe 2 following laser scanning of the OD and ID surfaces, along with the fracture surfaces from the area shown in Figure 3. The color represents the thickness, in inches, as denoted by the scale on the right.

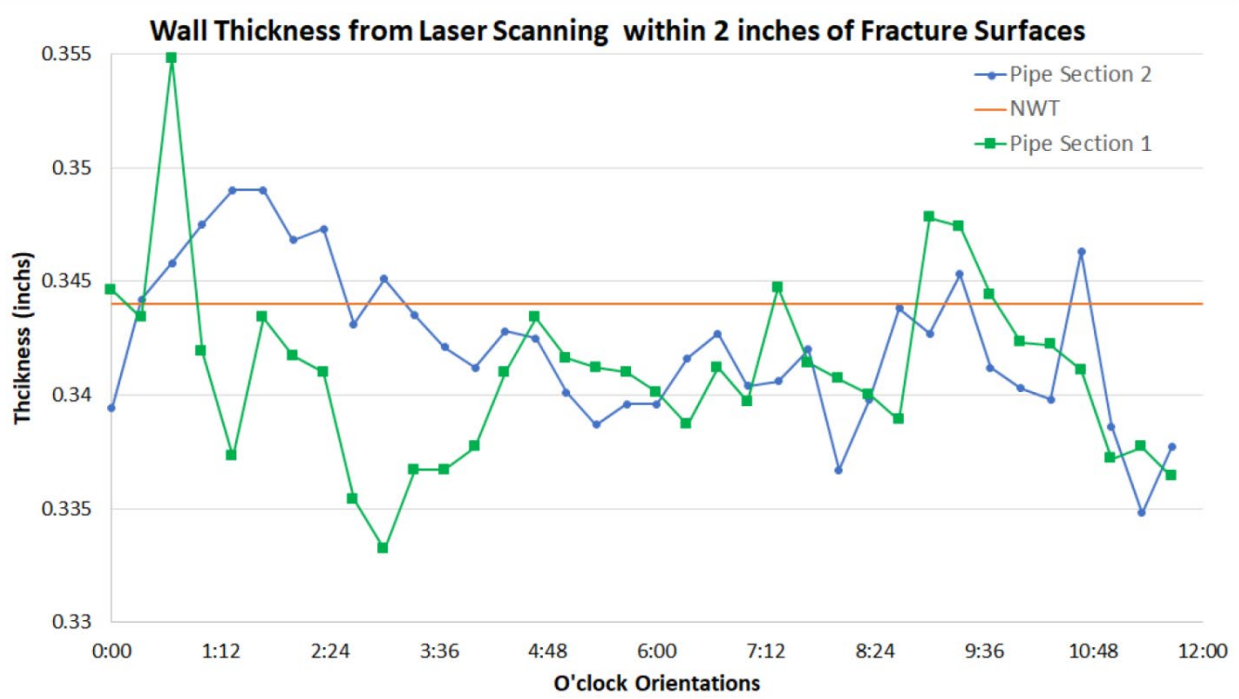

Figure 20. Laser scanning wall thicknesses measured within 2 inches of the fracture surface every 10 to 20°. The horizontal orange line represents the nominal wall thickness.

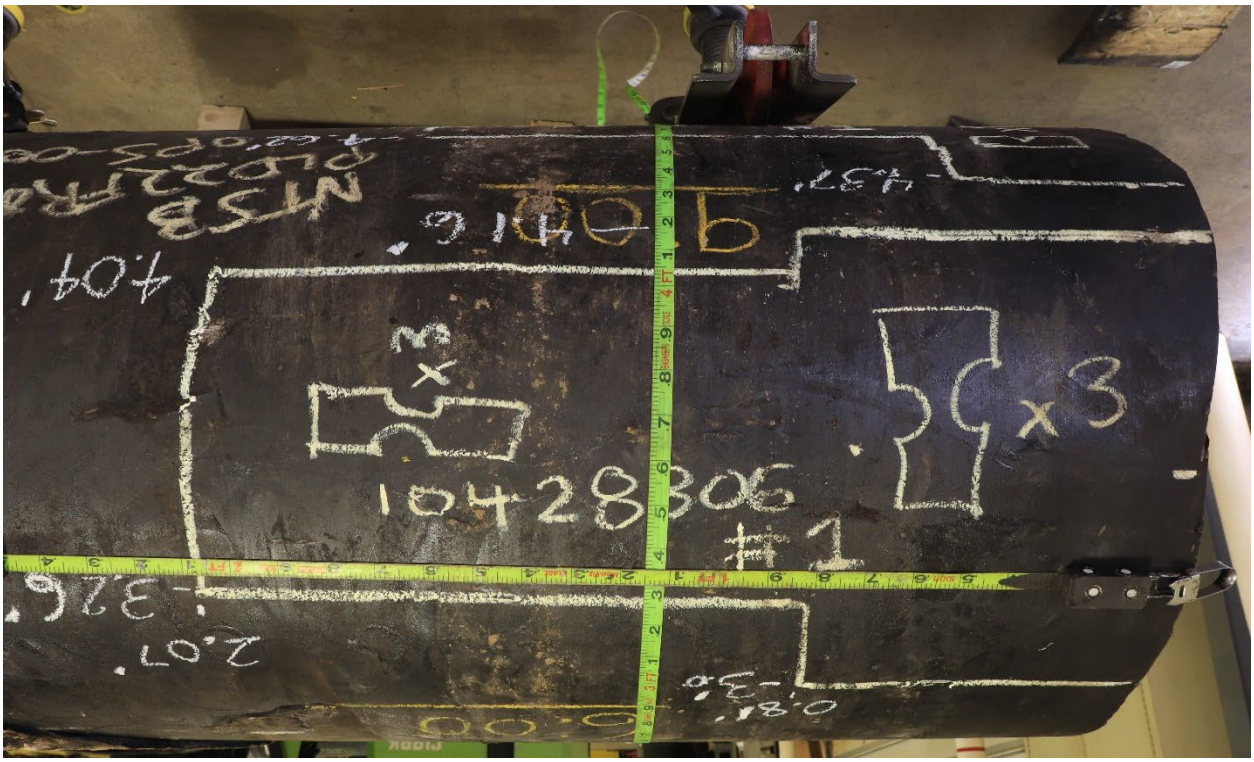

Figure 21. View of the outer surface of Pipe 1, showing areas annotated for extracting tensile test specimens, their numbers, and orientations.

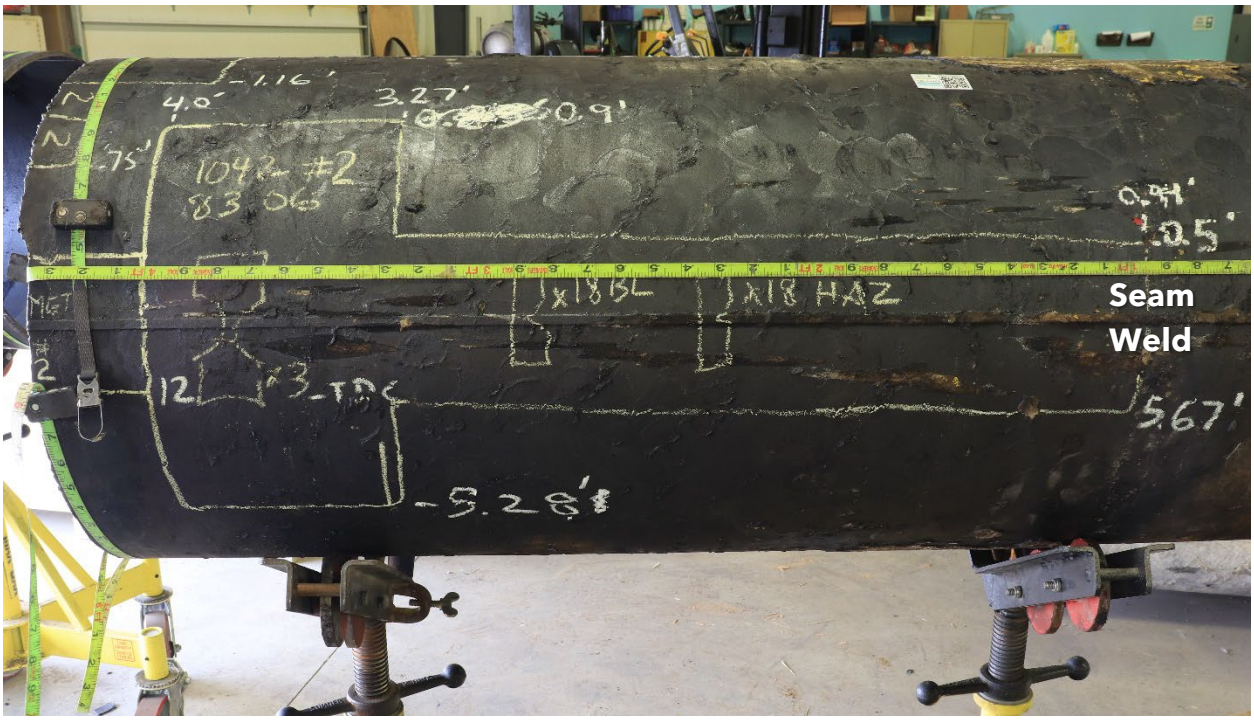

Figure 22. View of the outer surface of Pipe 1, showing areas annotated for extracting tensile impact test specimens across a seam weld, their numbers, and orientations.

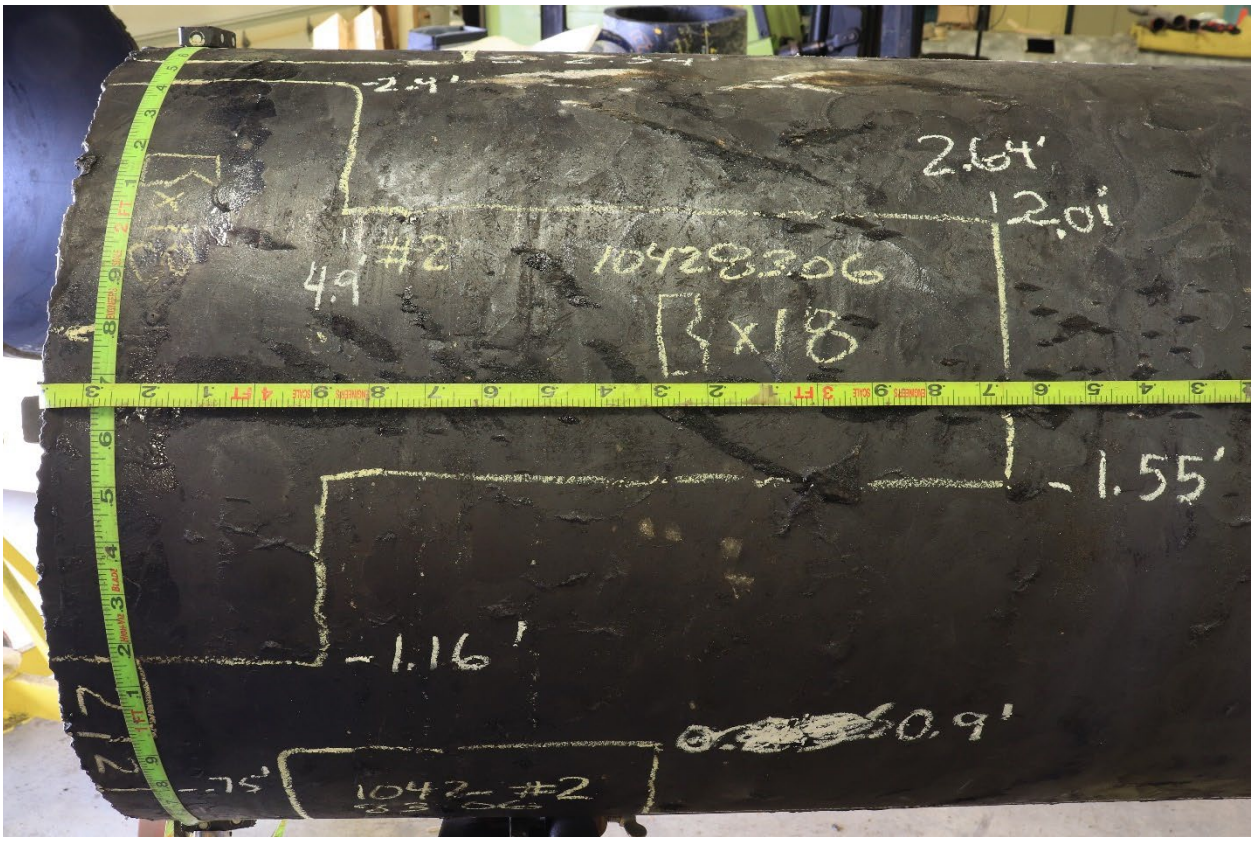

Figure 23. View of the outer surface of Pipe 1, showing areas annotated for extracting impact specimens, their numbers, and orientations.

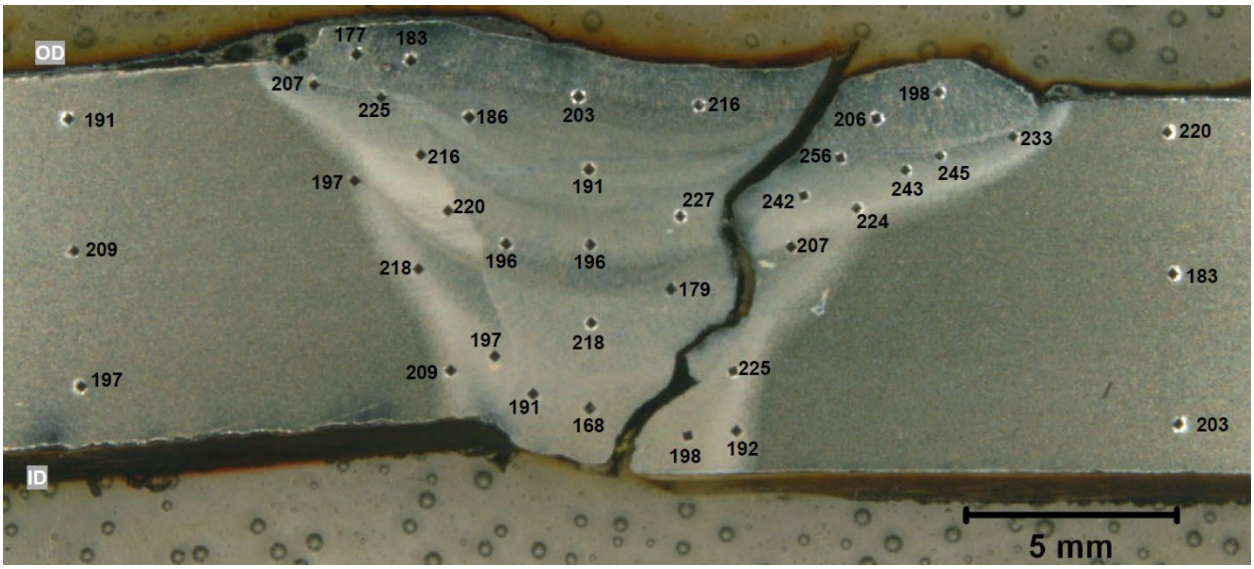

Figure 24. Bright-field (BF) optical micrograph of a cross-section through location M1_5b, showing Vickers hardness indents and their respective hardness data (etched, 2% Nital), showing hardness values from 168 HV to 256 HV.

Figure 25. View of the entire fracture surface of Pipe 2 that had mated to that of Pipe 1.

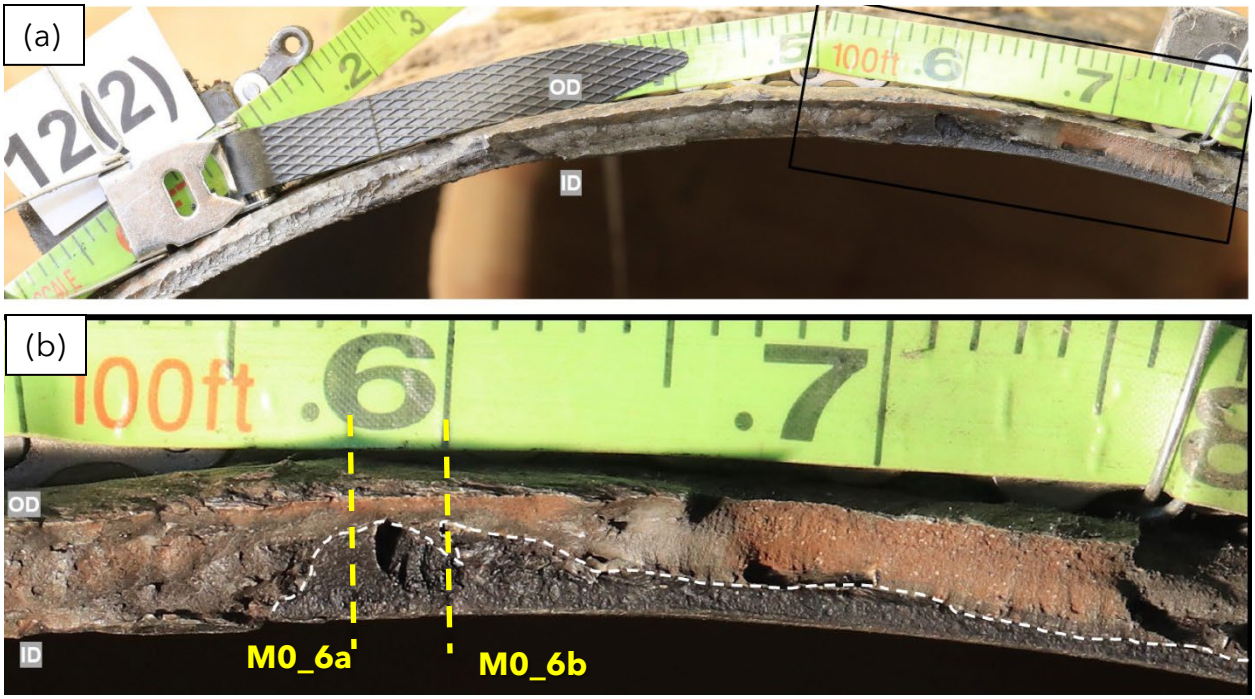

Figure 26. View of the Pipe 2 fracture surface (a) clockwise of the 12 o'clock position, post cleaning with (b) showing an inner diameter surface breaking feature, outlined by white dashed lines. Between 0.5 and 1.2 feet clockwise of TDC.

Figure 27. View of the Pipe 2 fracture surface counterclockwise of the 3 o'clock position.

Figure 28. View of the Pipe 2 fracture surface clockwise of the 3 o'clock position.

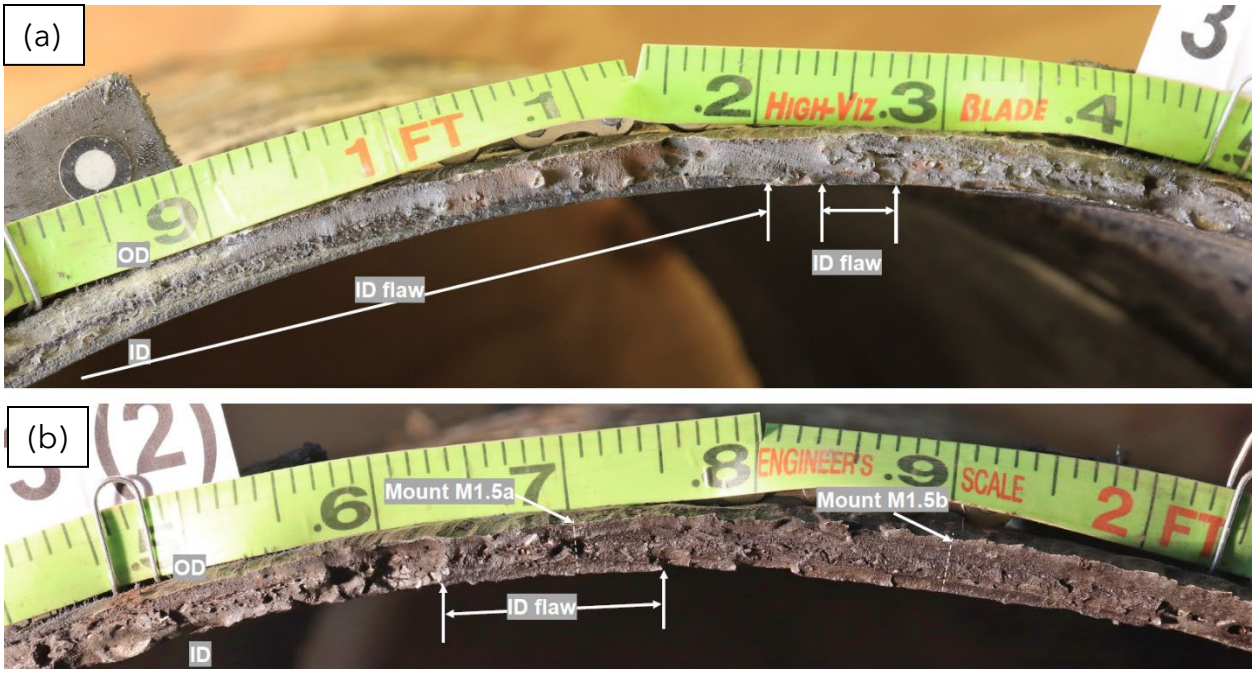

Figure 29. Closer views of Figure 27 and Figure 28, annotated to show (a) counterclockwise of 3 o'clock and two inner diameter flaws and (b) clockwise of 3 o'clock, showing a ID flaw and the location of two metallographic cross sections.


Figure 30. View of the Pipe 2 fracture surface counterclockwise of the 6 o'clock position.

Figure 31. View of the Pipe 2 fracture surface counterclockwise of the 9 o'clock position.

Figure 32. View of the Pipe 2 fracture surface clockwise of the 9 o'clock position, annotated to how the location of one of the metallographic cross section.

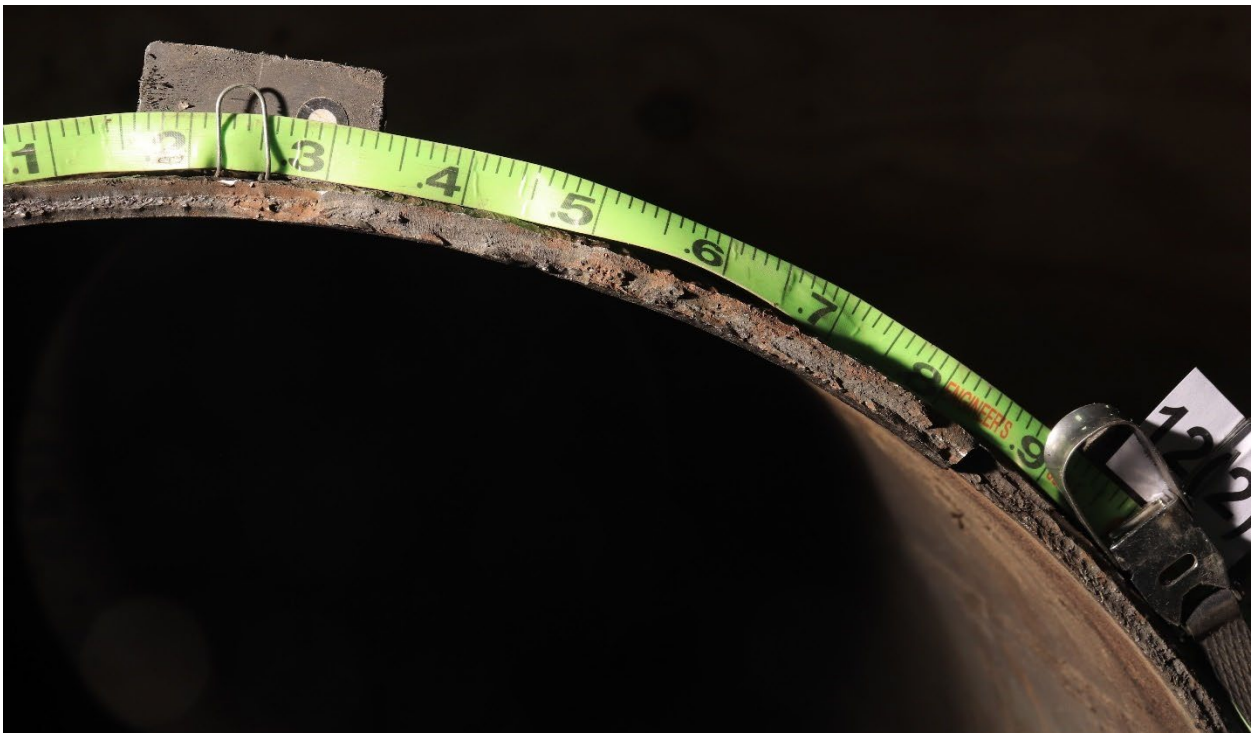

Figure 33. View of the Pipe 2 fracture surface counterclockwise of the 12 o'clock position.

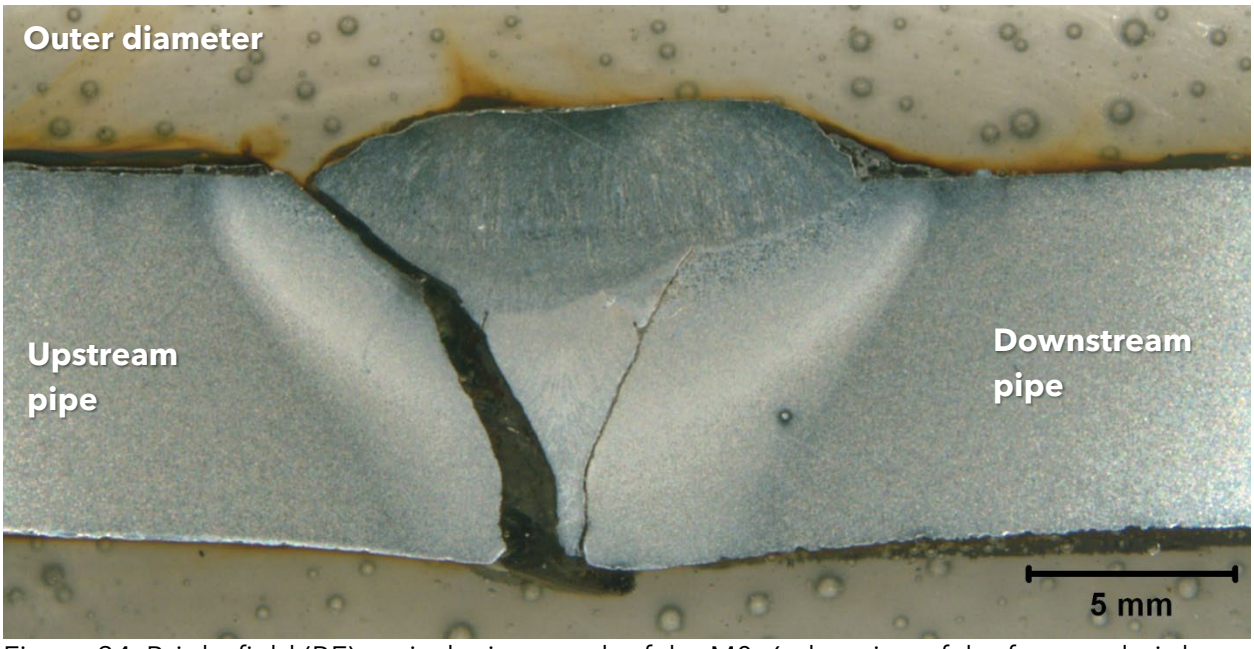

Figure 34. Bright-field (BF) optical micrograph of the M0_6a location of the fractured girth weld, sectioned 7 inches clockwise of 12 o'clock near the deepest portion of the ID surface braking flaw in Figure 26b (~5X, etched 2% Nital).

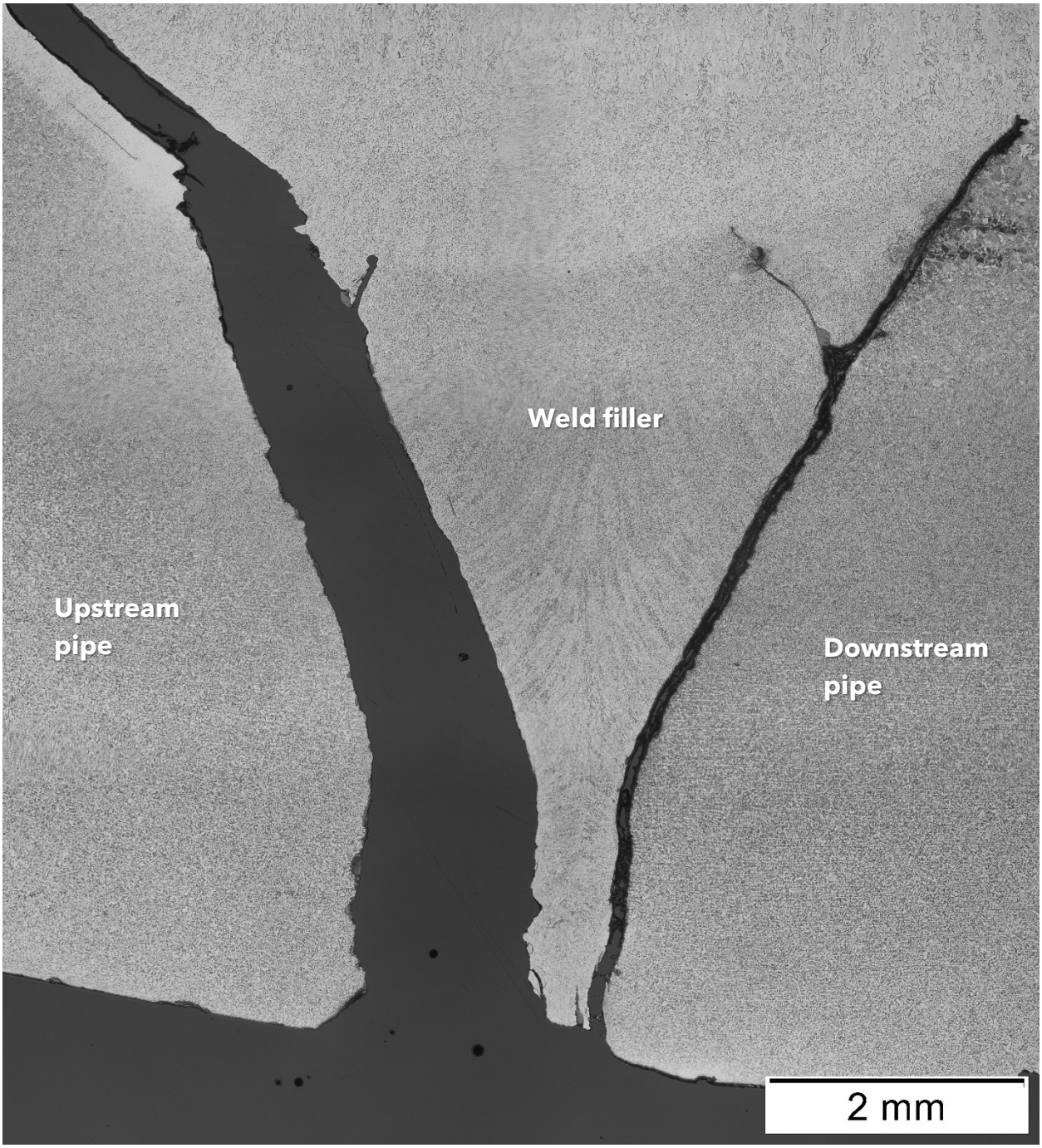

Figure 35. BF optical micrograph of the inner diameter portion of the fracture at M0_6A (~25X, etched 2% nital)

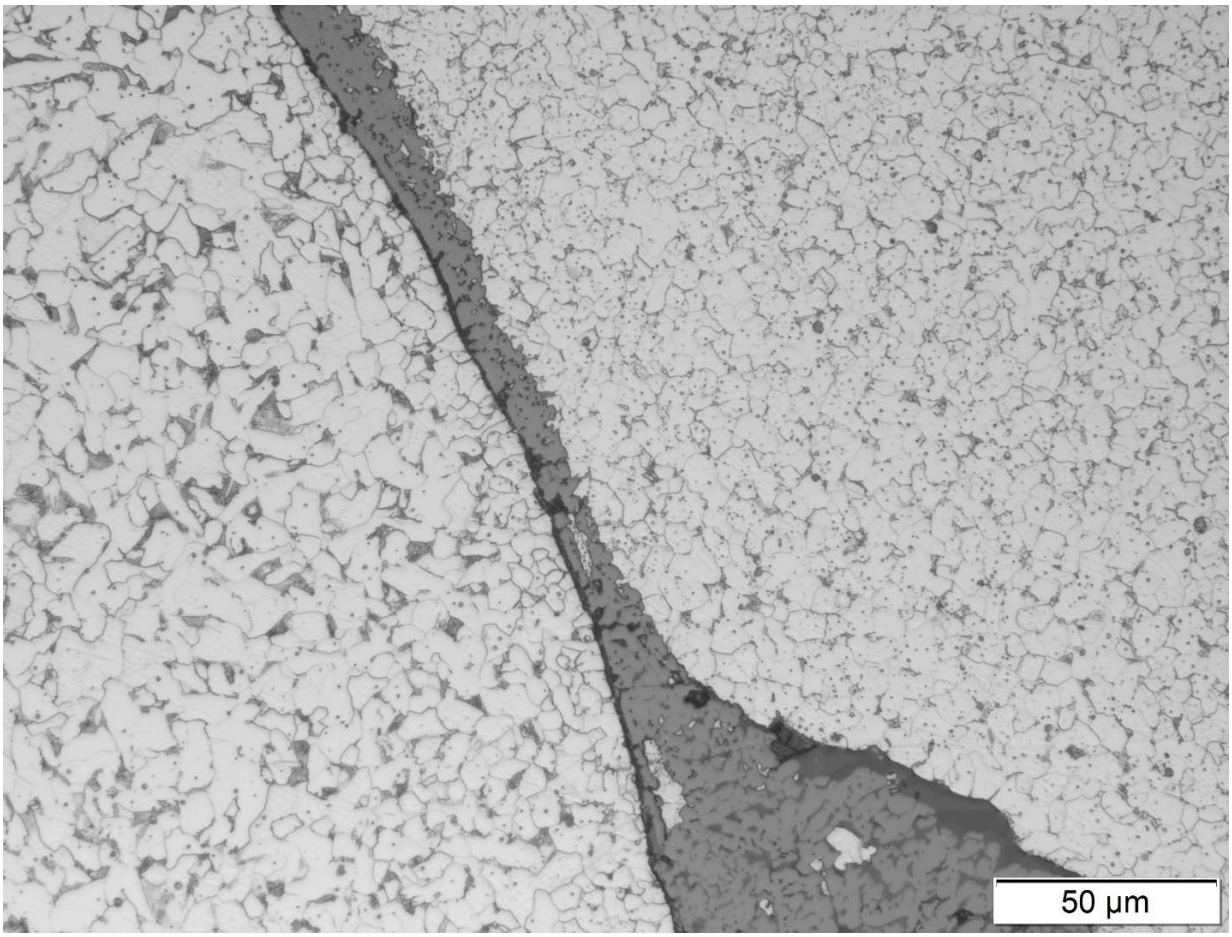

Figure 36. BF optical micrograph of the inward crack branch below the weld in M0_6a (~400X, etched 2% Nital).

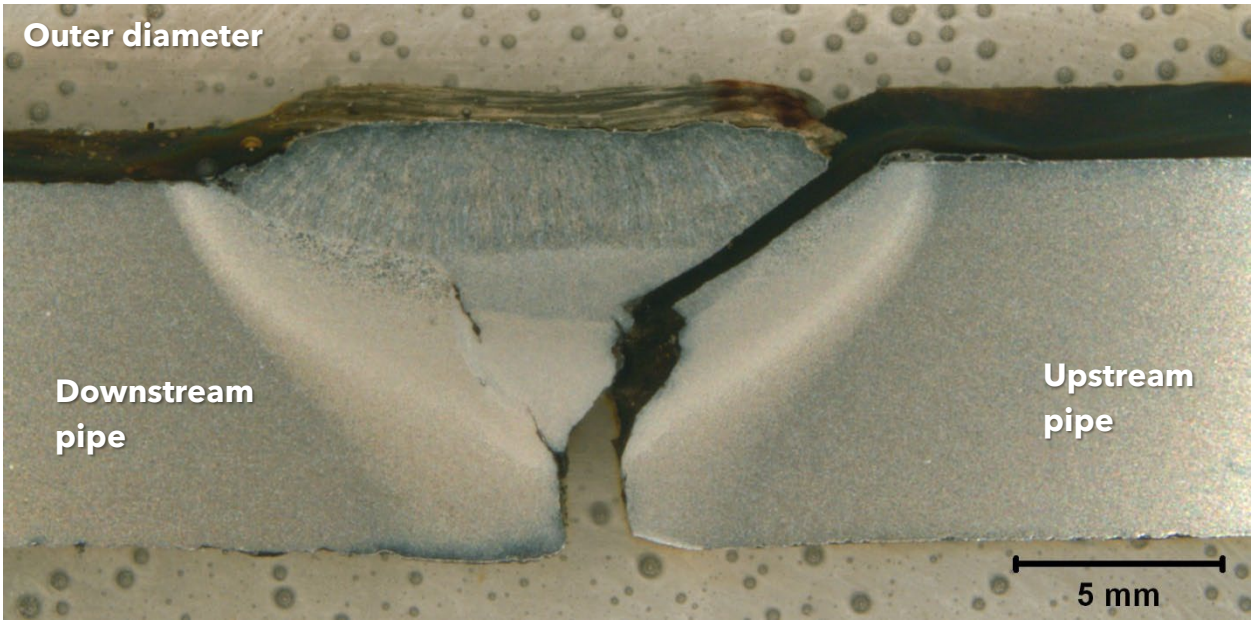

Figure 37. BF optical micrograph of the fracture at the girth weld at location M0_6b (~5X, etched 2% Nital).

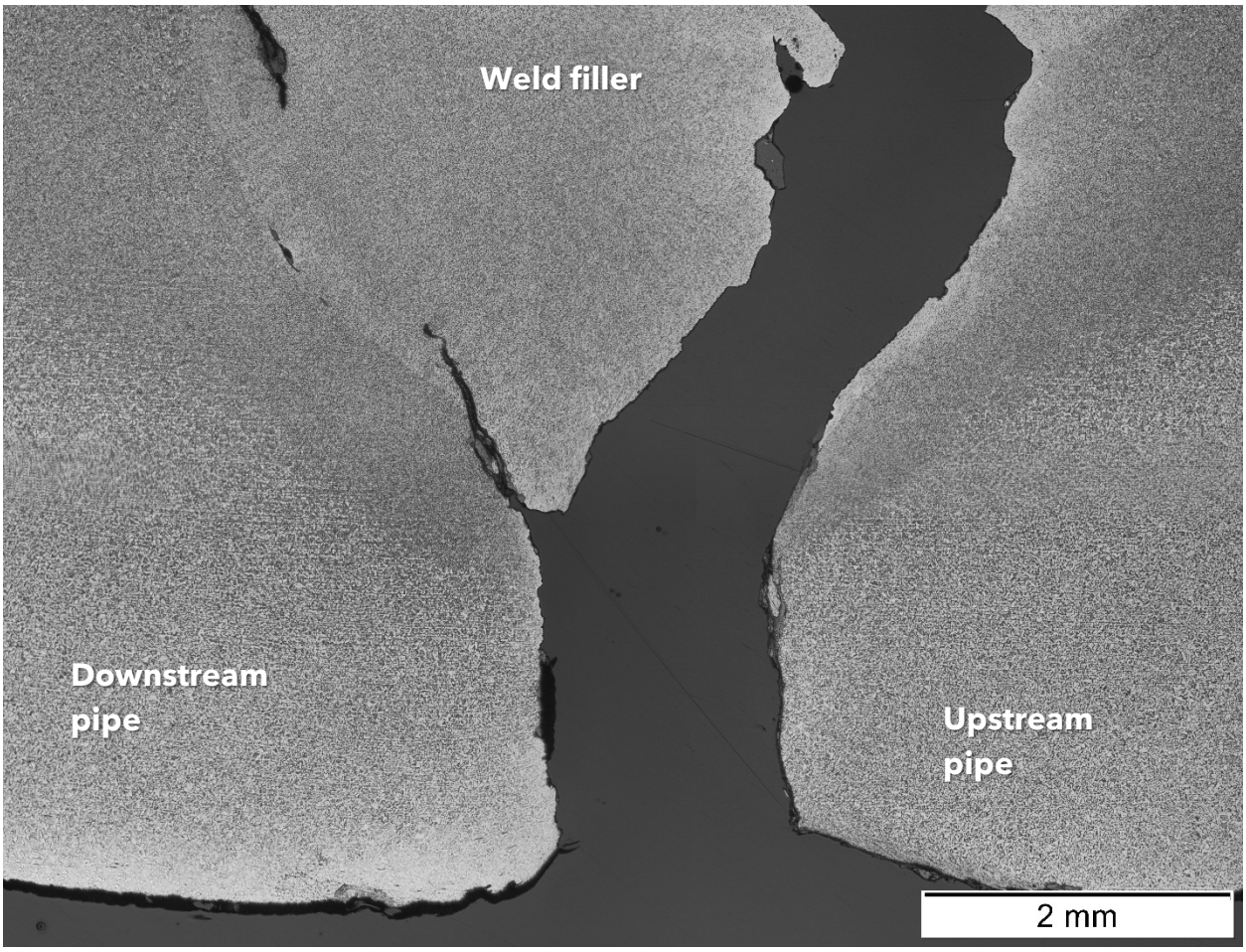

Figure 38. BF optical micrograph of the inner diameter portion of the fracture at M0_6b (~25X, etched 2% Nital)

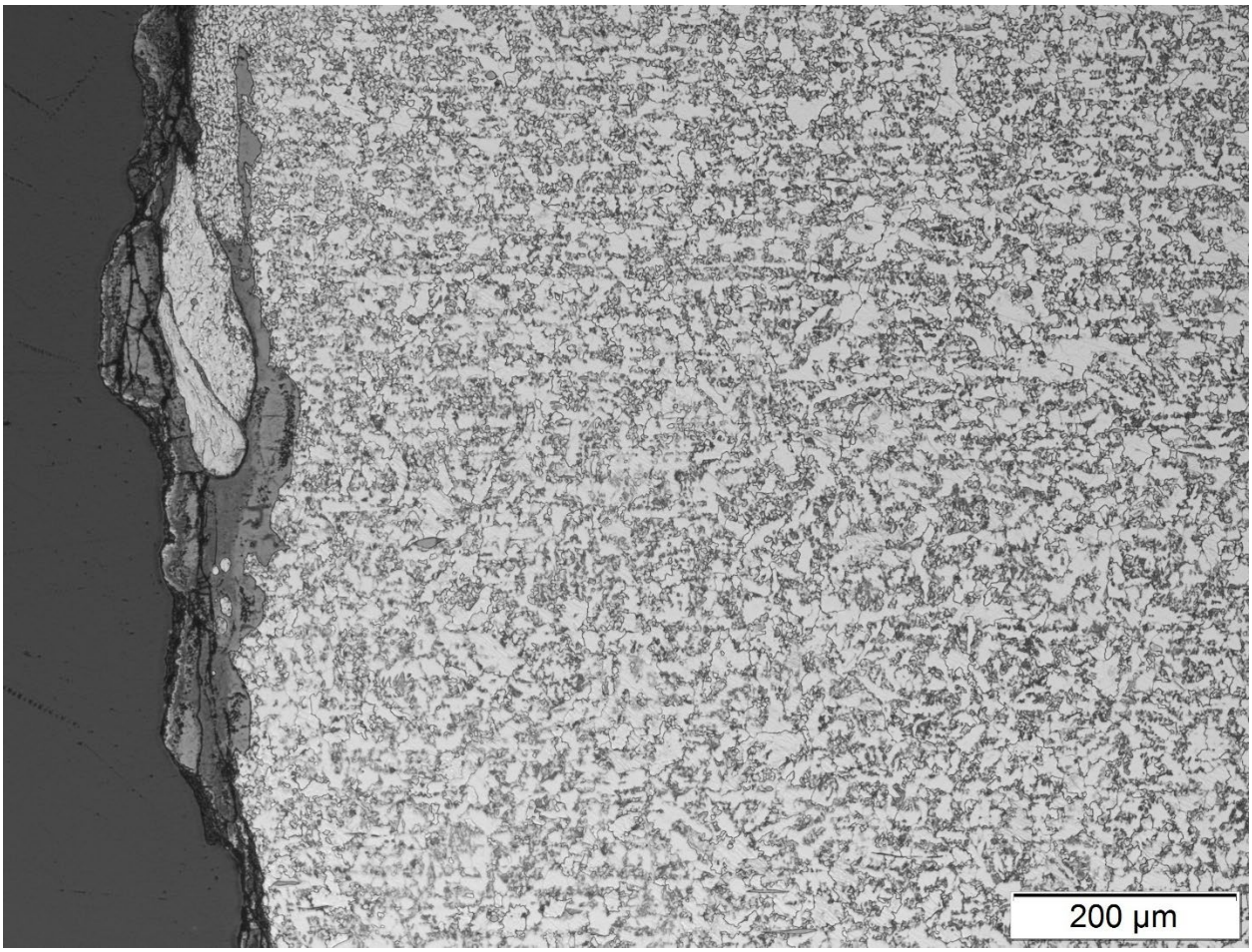

Figure 39. BF optical micrograph of the crack face on the right on M0_6b from Figure 38, near the ID, showing surface oxide (~100X, etched 2% Nital).

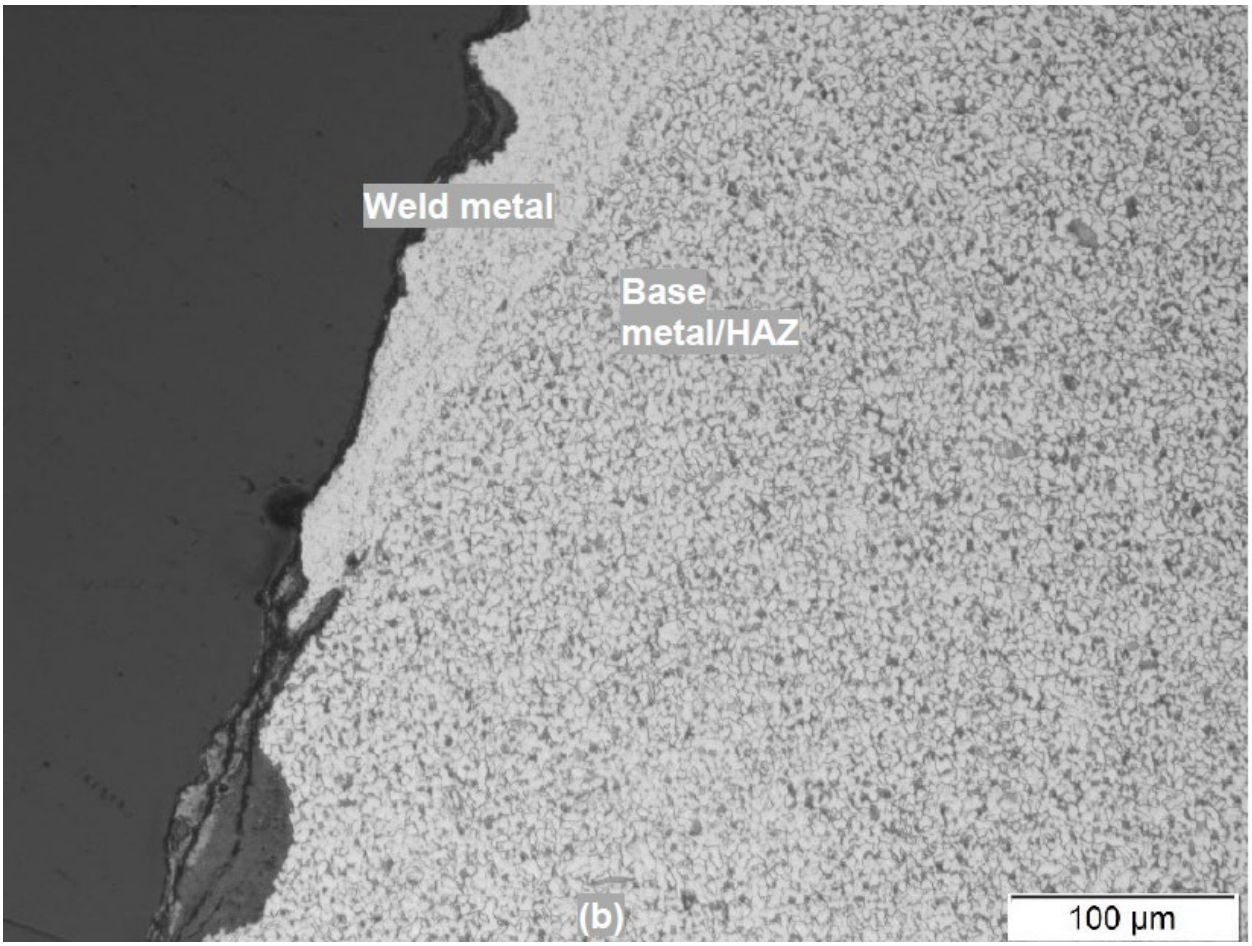

Figure 40. BF optical micrograph of the area above that in Figure 39, showing the delineation between the weld metal and the heat-affected zone of the base metal (~100X, etched 2% Nital).

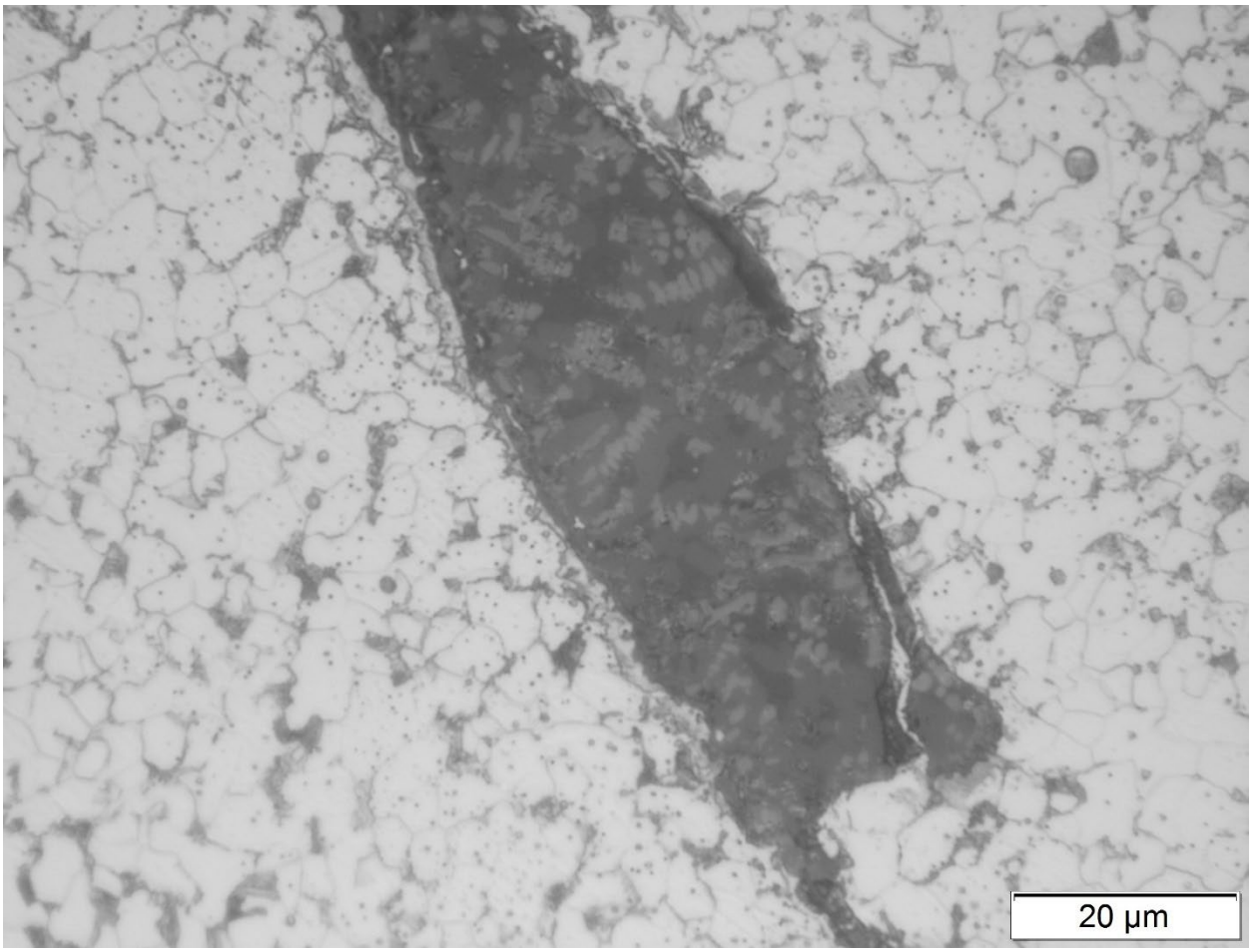

Figure 41. BF optical micrograph of an area of oxide near the weld in M0_6b, showing a dendritic structure (~400X, etched 2% Nital).

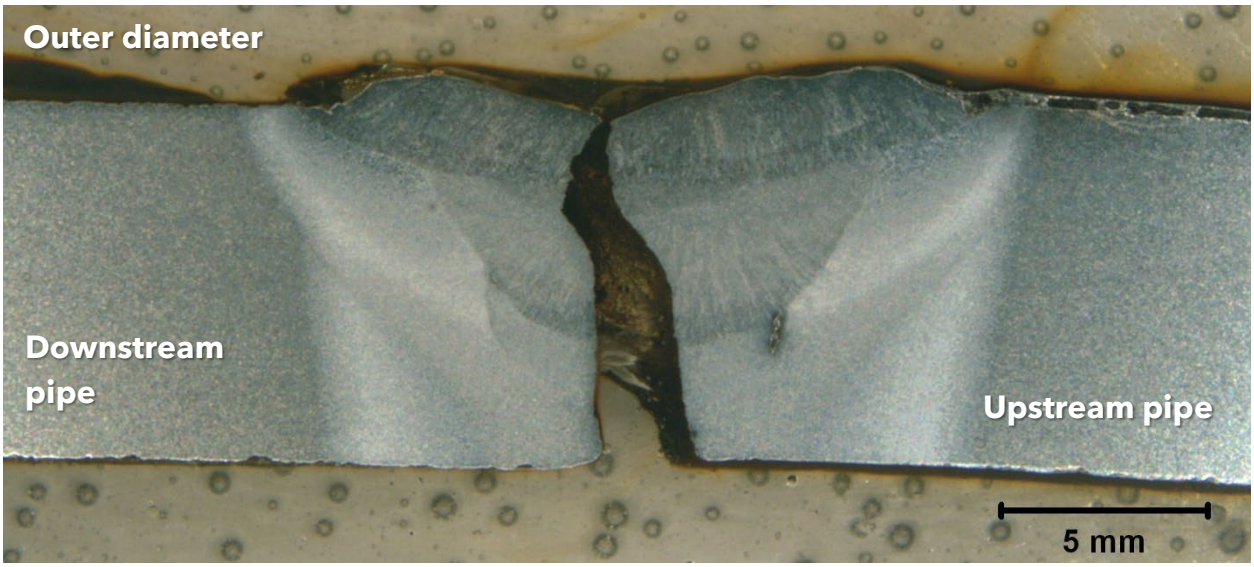

Figure 42. BF optical micrograph of the fracture at the girth weld at location M0_6c (~5X, etched 2% Nital).

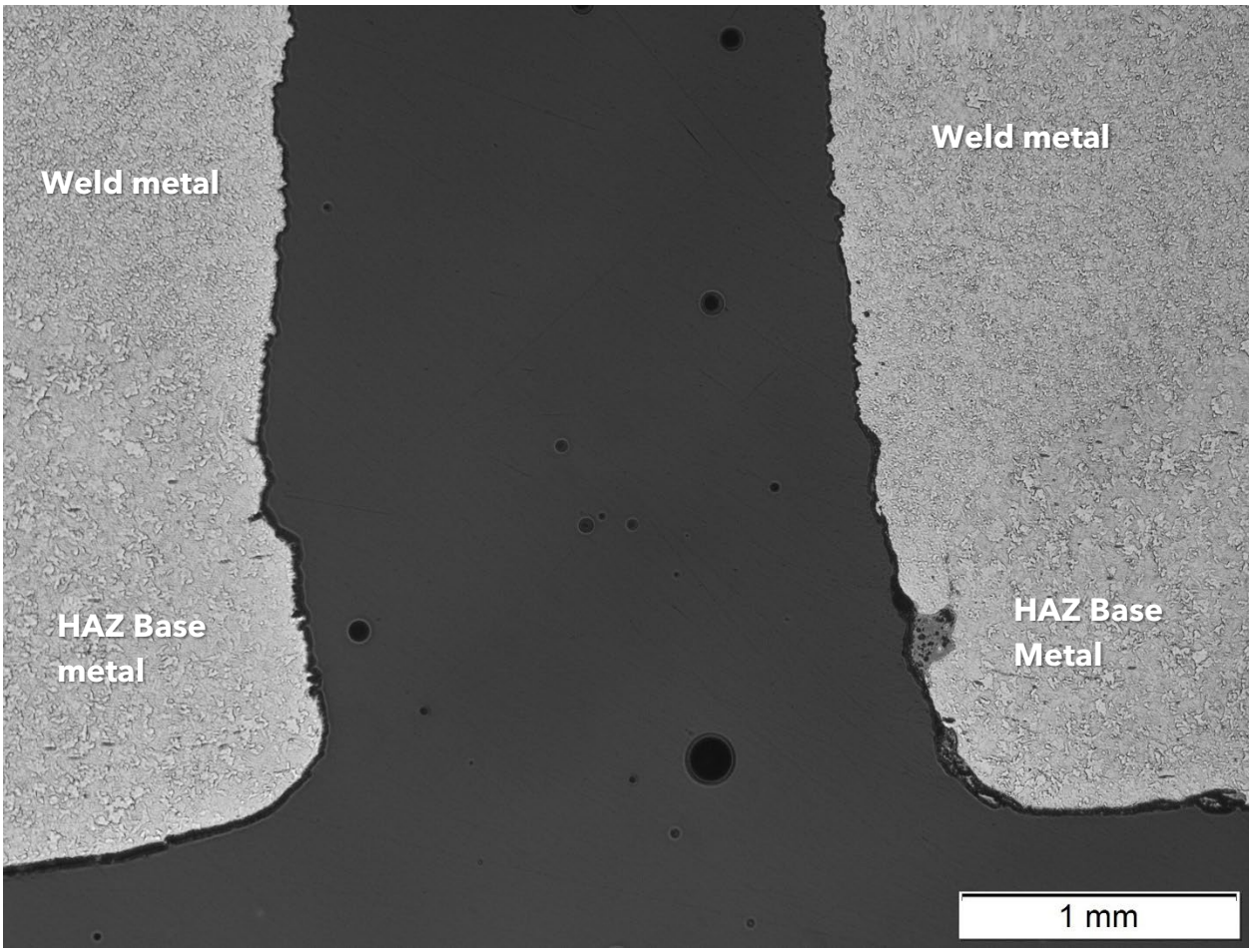

Figure 43. BF optical micrograph of the inner diameter of the fracture in location M0_6c (25X, etched 2% Nital).

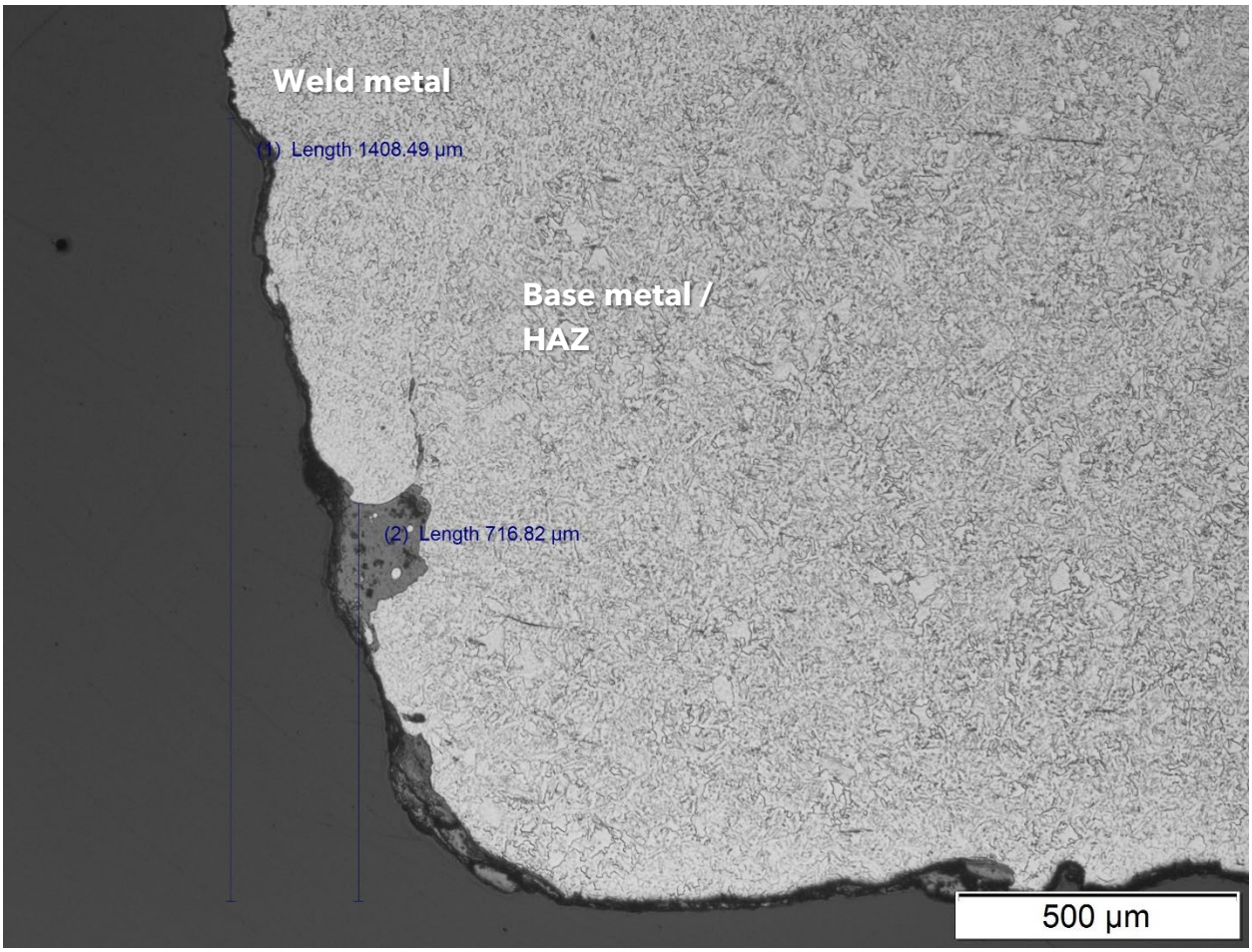

Figure 44. BF optical micrograph of surface oxides in the lower right of Figure 43, annotated with measurements from the inner diameter. (~100X, etched 2% Nital).

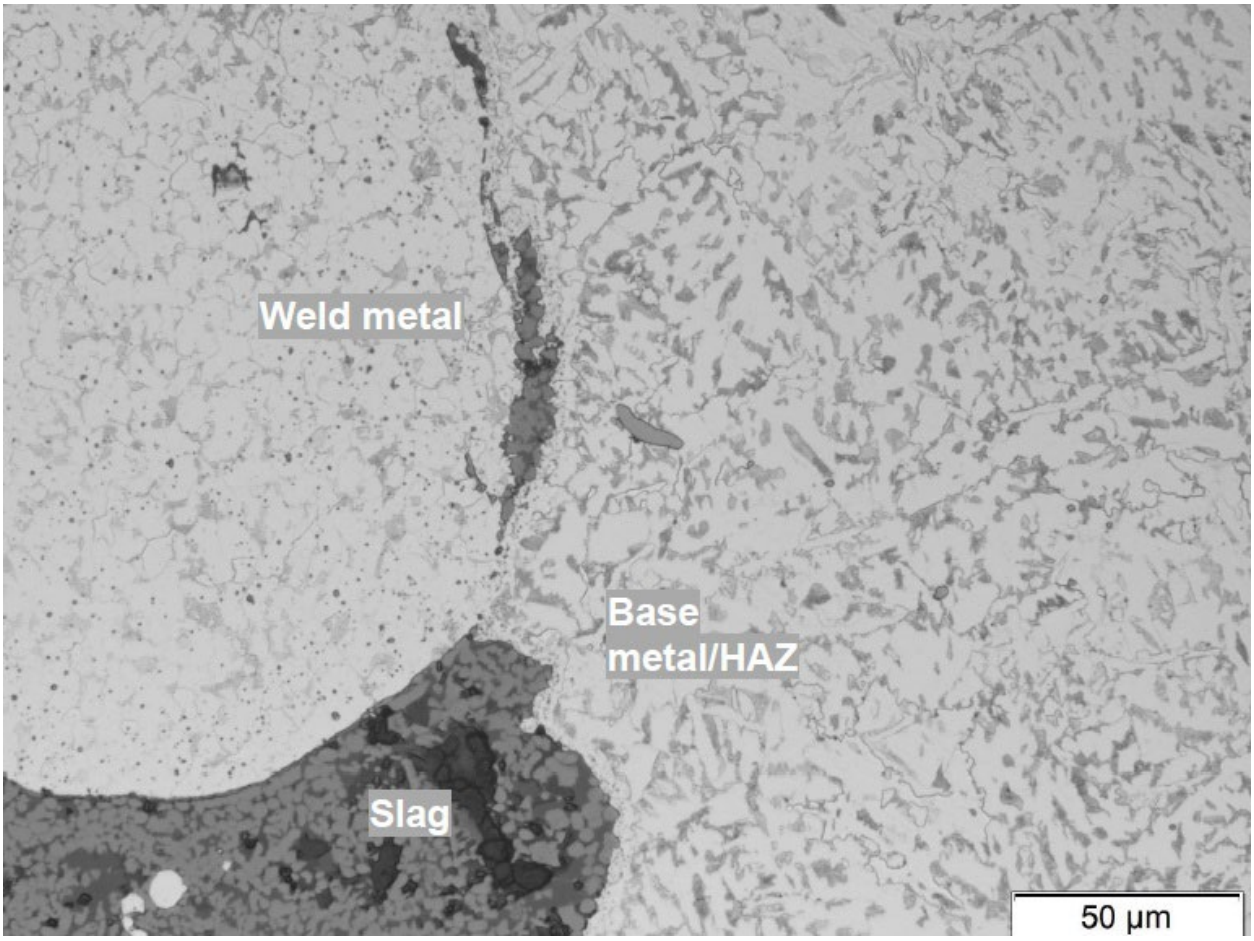

Figure 45. BF optical micrograph of the boxed area in Figure 44, showing the delineation between the weld and base metals, with intermediate slag (~500X, etched 2% Nital).

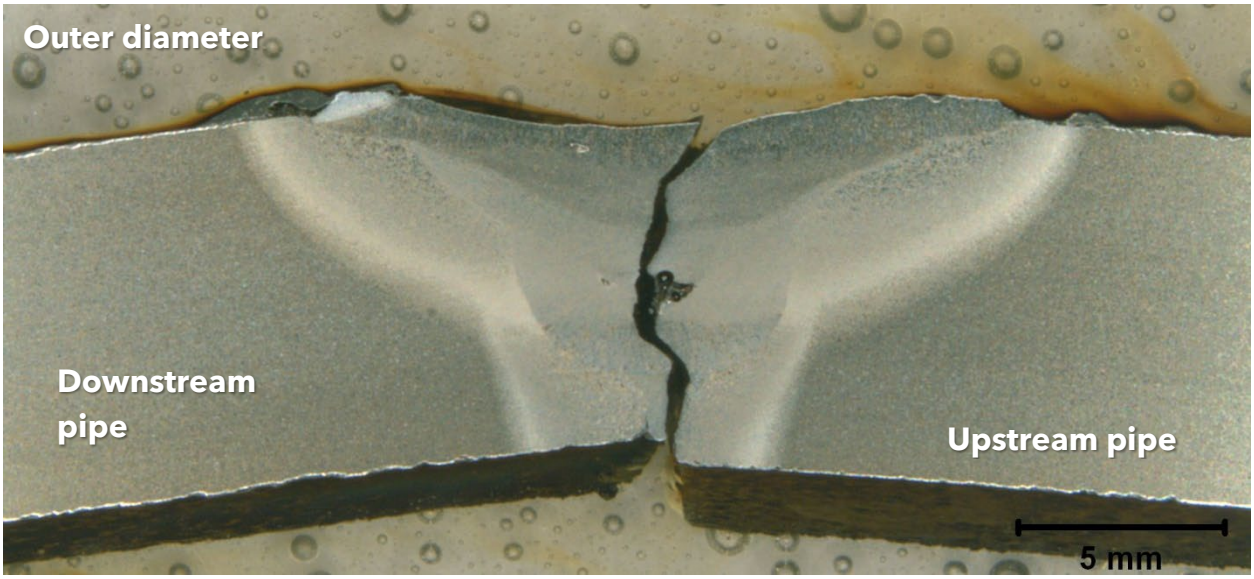

Figure 46. BF optical micrograph of the fracture at the girth weld at location M1_5a, 1.61 feet clockwise from 12 o'clock (~5X, etched 2% Nital).

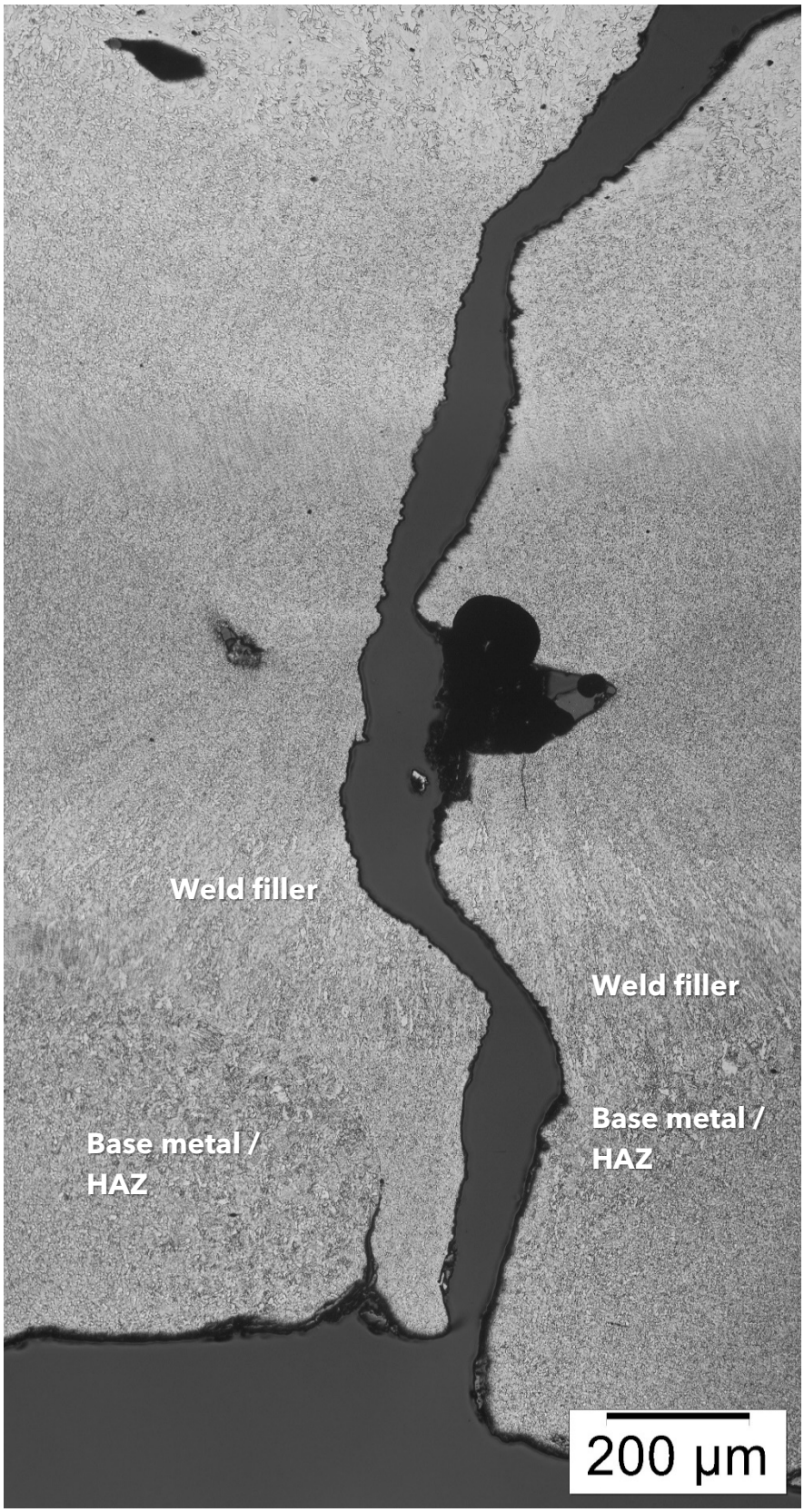

Figure 47. BF optical micrograph montage of the fracture through weld M1_5A (~25X, etched 2% Nital).

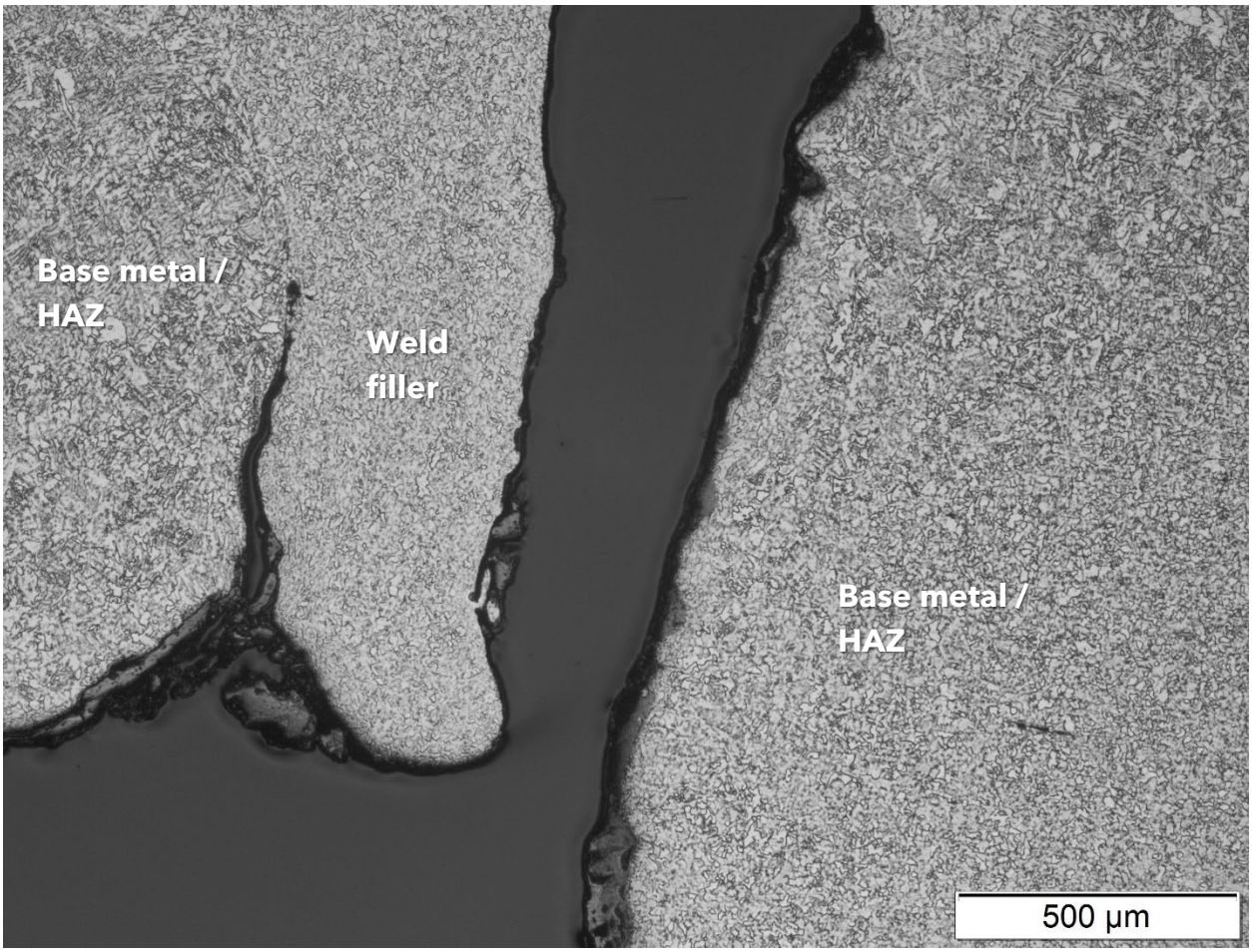

Figure 48. BF optical micrograph of weld laps and oxides on the inner diameter surface of weld M1_5a (50X, etched 2% Nital).

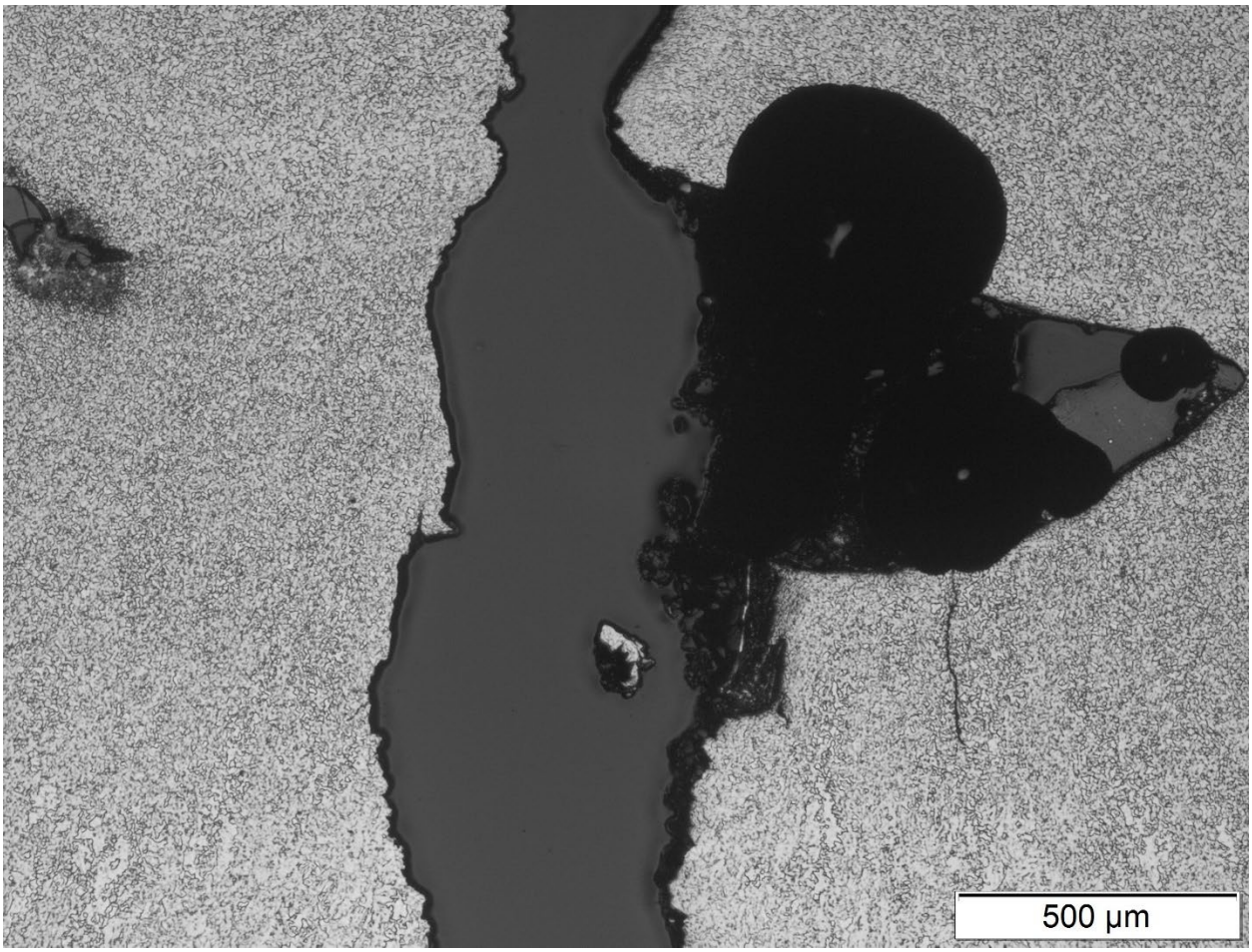

Figure 49. BF optical micrograph of the void and oxide in the center of the cross section inside the weld filler from Figure 47 (50X, etched 2% Nital).

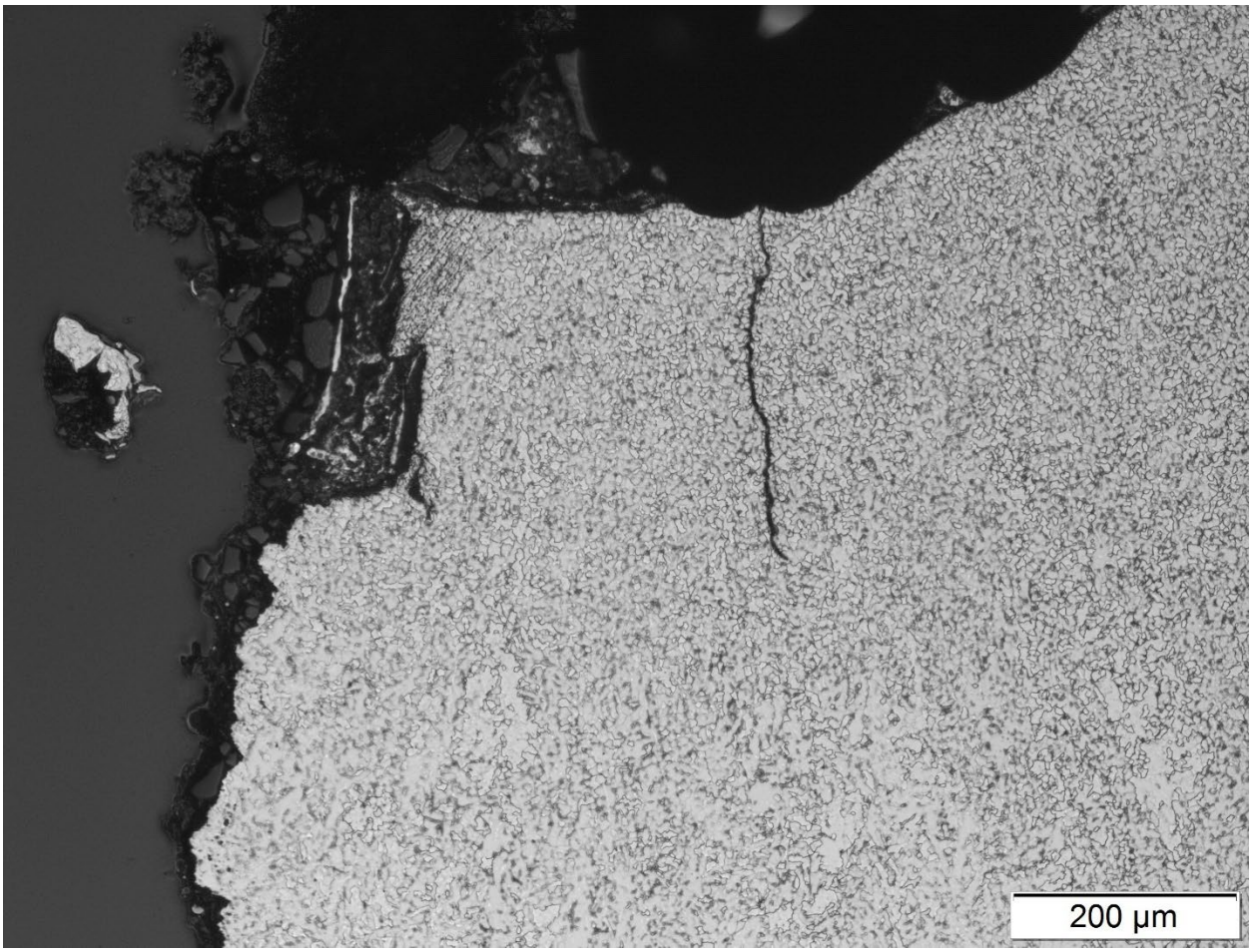

Figure 50. BF optical micrograph of the crack propagating from a void in Figure 49 (100X, etched 2% Nital).

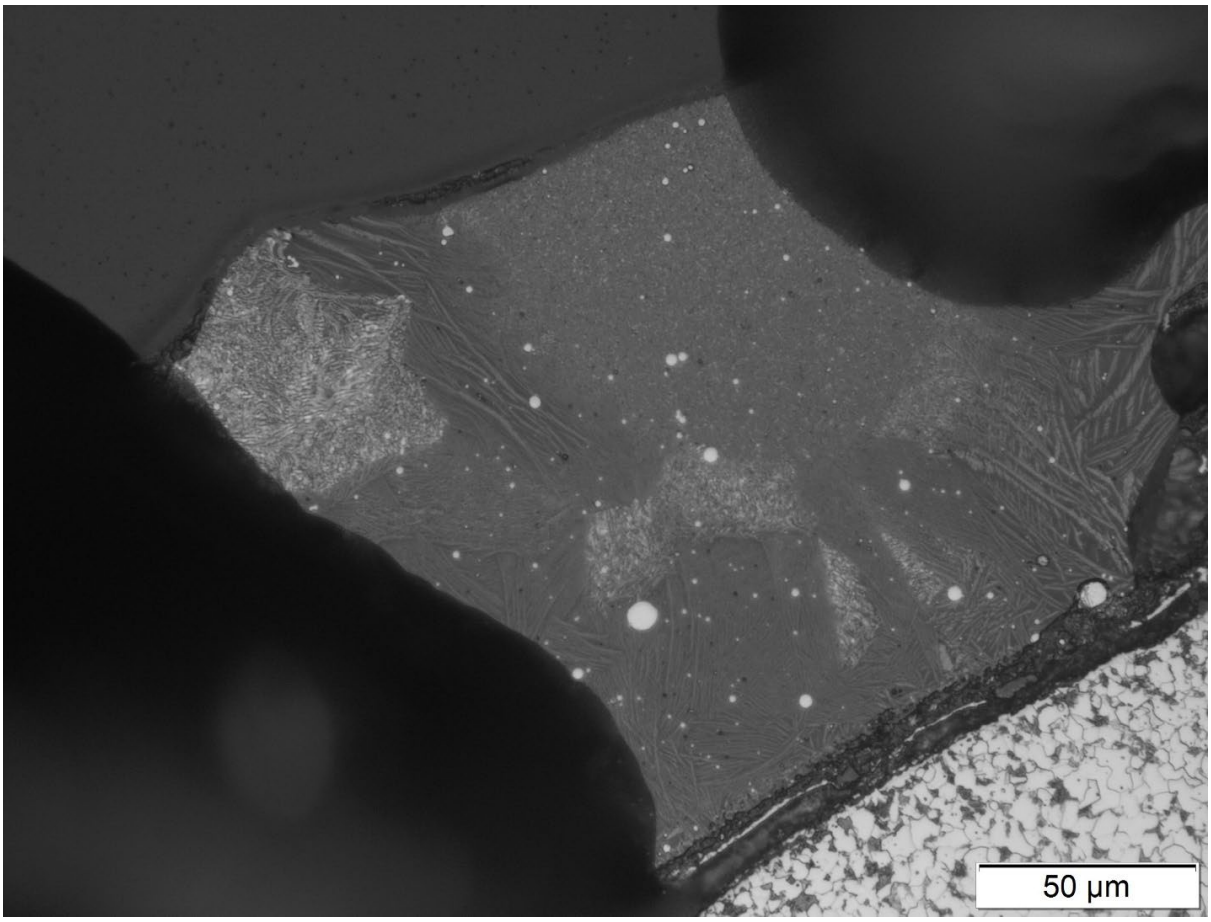

Figure 51. BF optical micrograph of dendritic compounds in the void of Figure 49 (400X, etched 2% Nital).

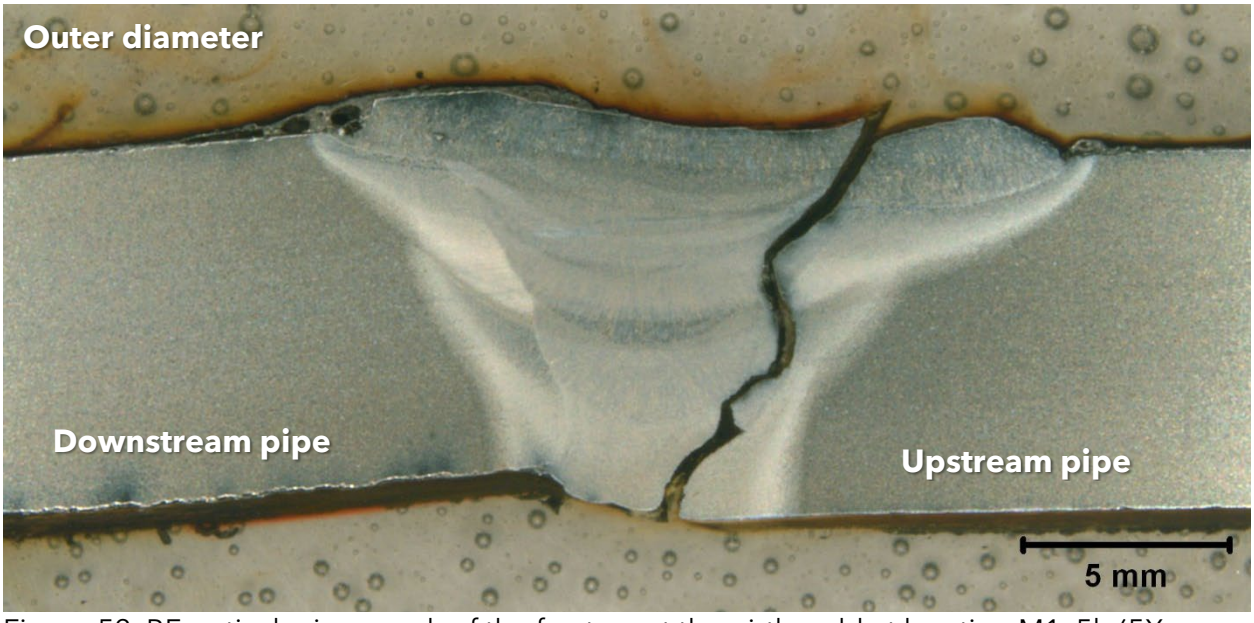

Figure 52. BF optical micrograph of the fracture at the girth weld at location M1_5b (5X, etched 2% Nital).

Figure 53. BF optical micrograph montage of the fracture through weld M1_5b (~25X, etched 2% Nital).

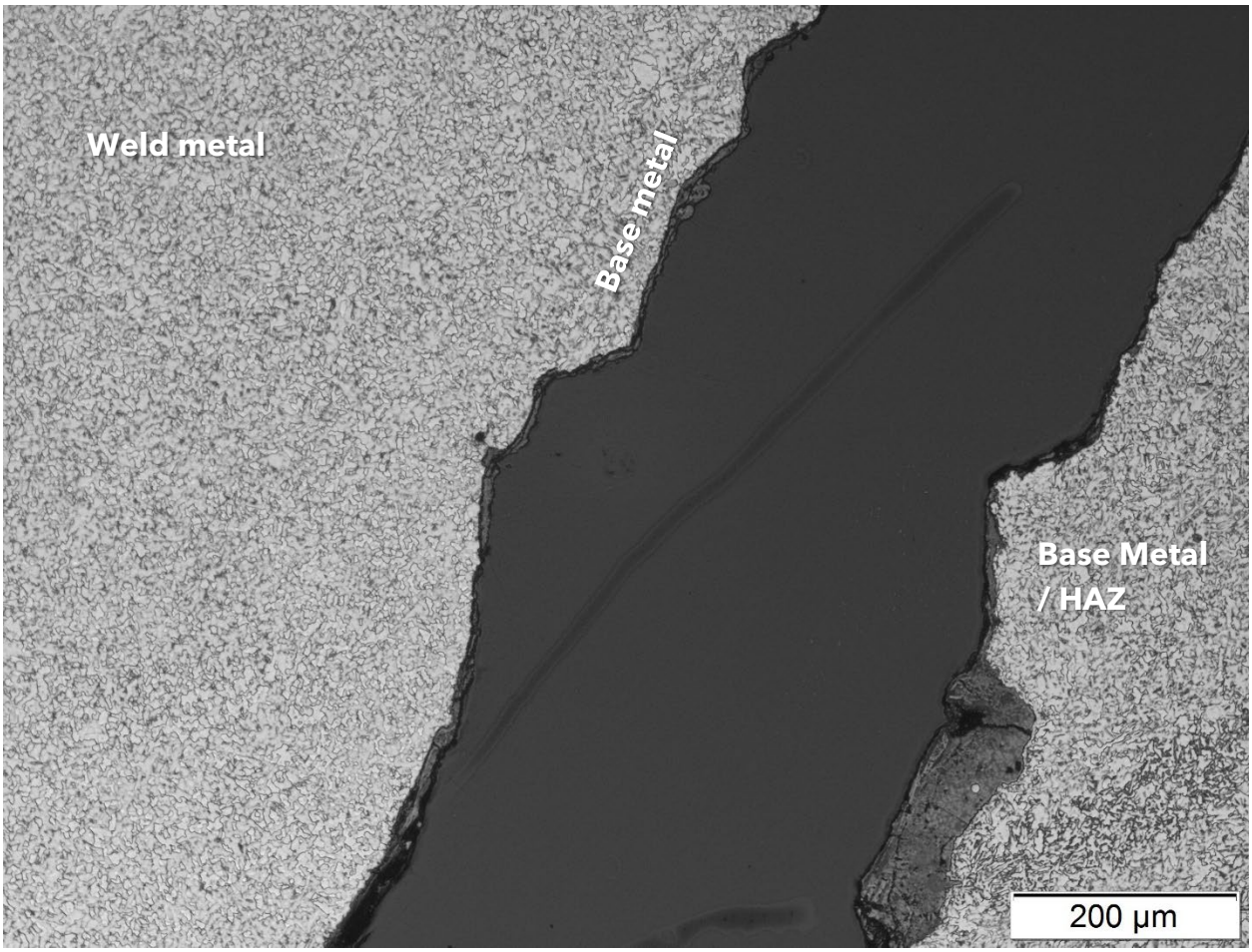

Figure 54. BF optical micrograph of oxide films along the fracture in Figure 53 (~100X, etched 2% Nital).

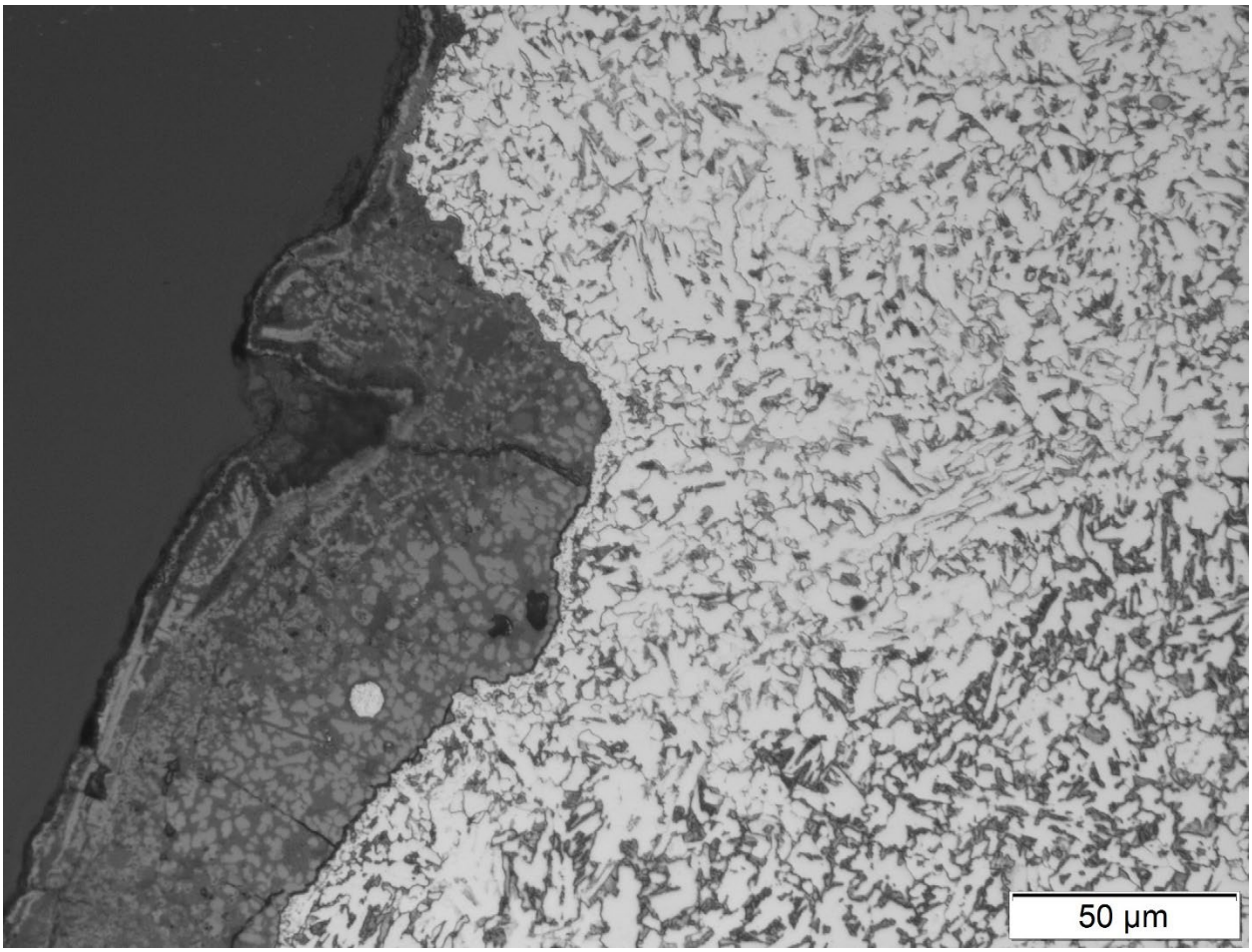

Figure 55. BF optical micrograph of the oxide globule to the right in Figure 54 (~400X, etched 2% Nital).

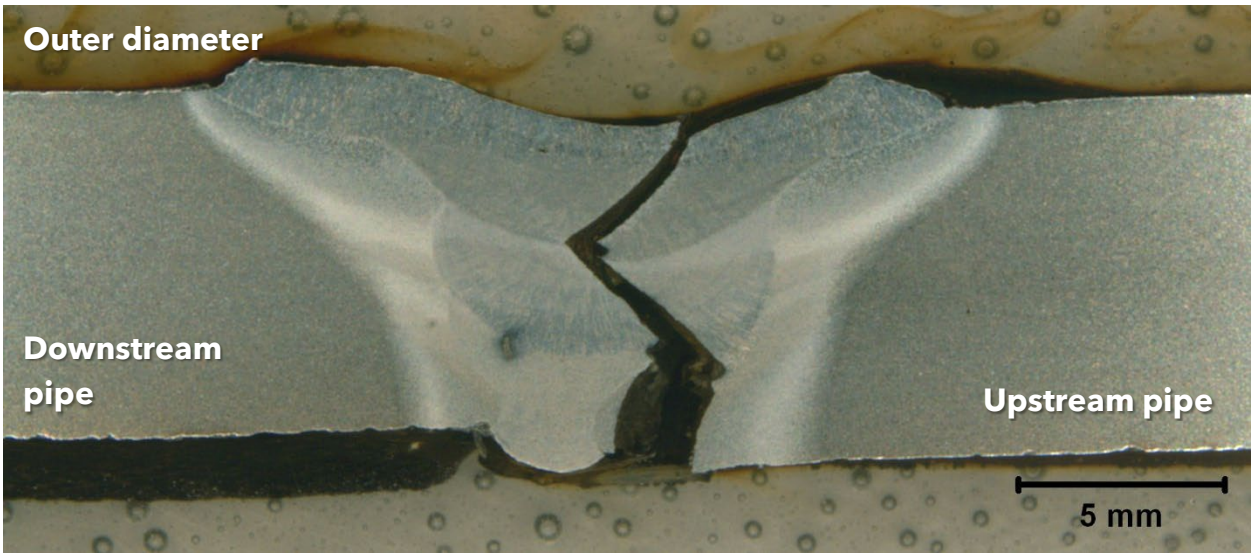

Figure 56. BF optical micrograph of the fracture at the girth weld at location M4_3, removed 4.31 feet clockwise of 12 o'clock top dead center (~5X, etched 2% Nital)

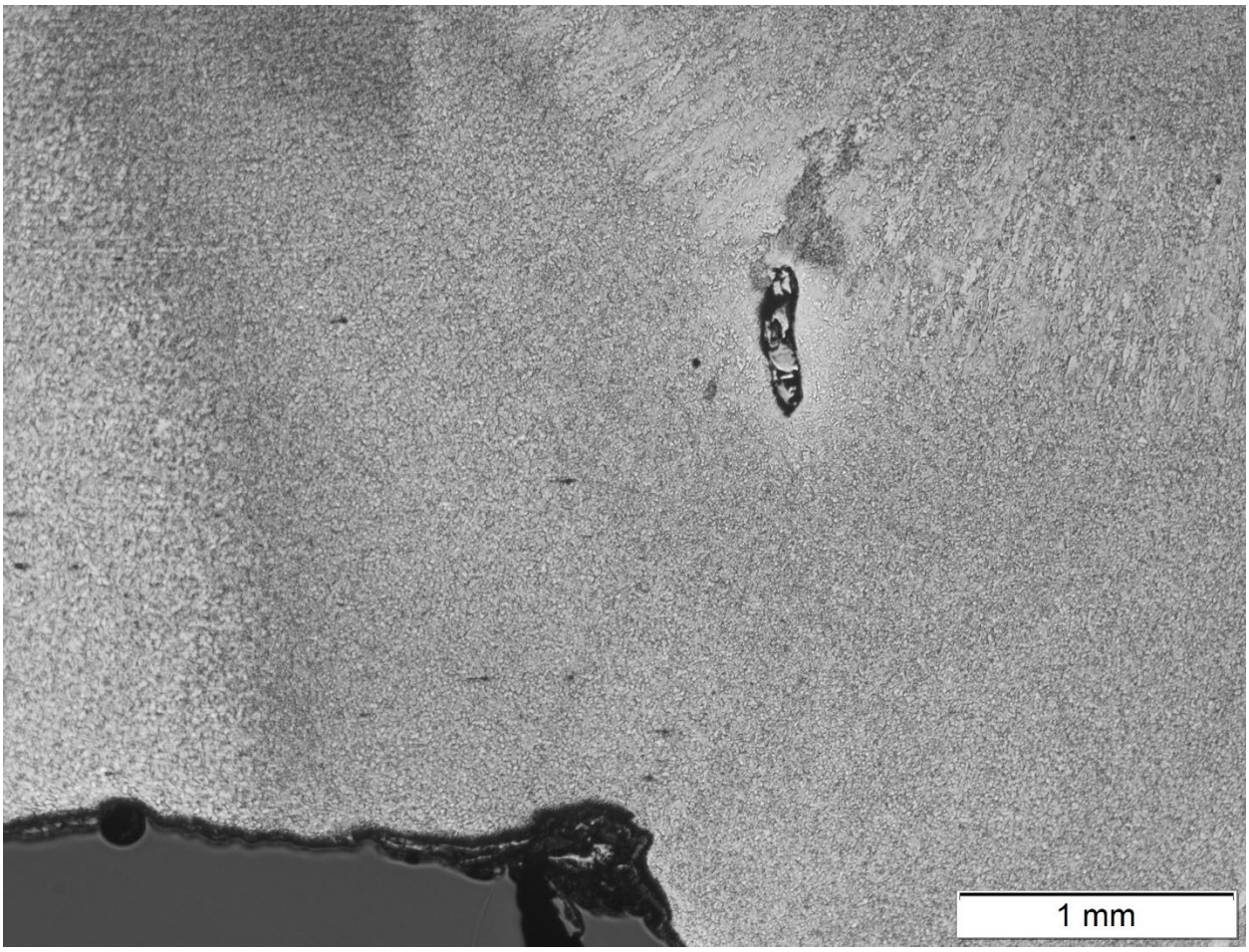

Figure 57. BF optical micrograph of an inclusion below a weld pass in Figure 56 (~25X, etched 2% Nital).

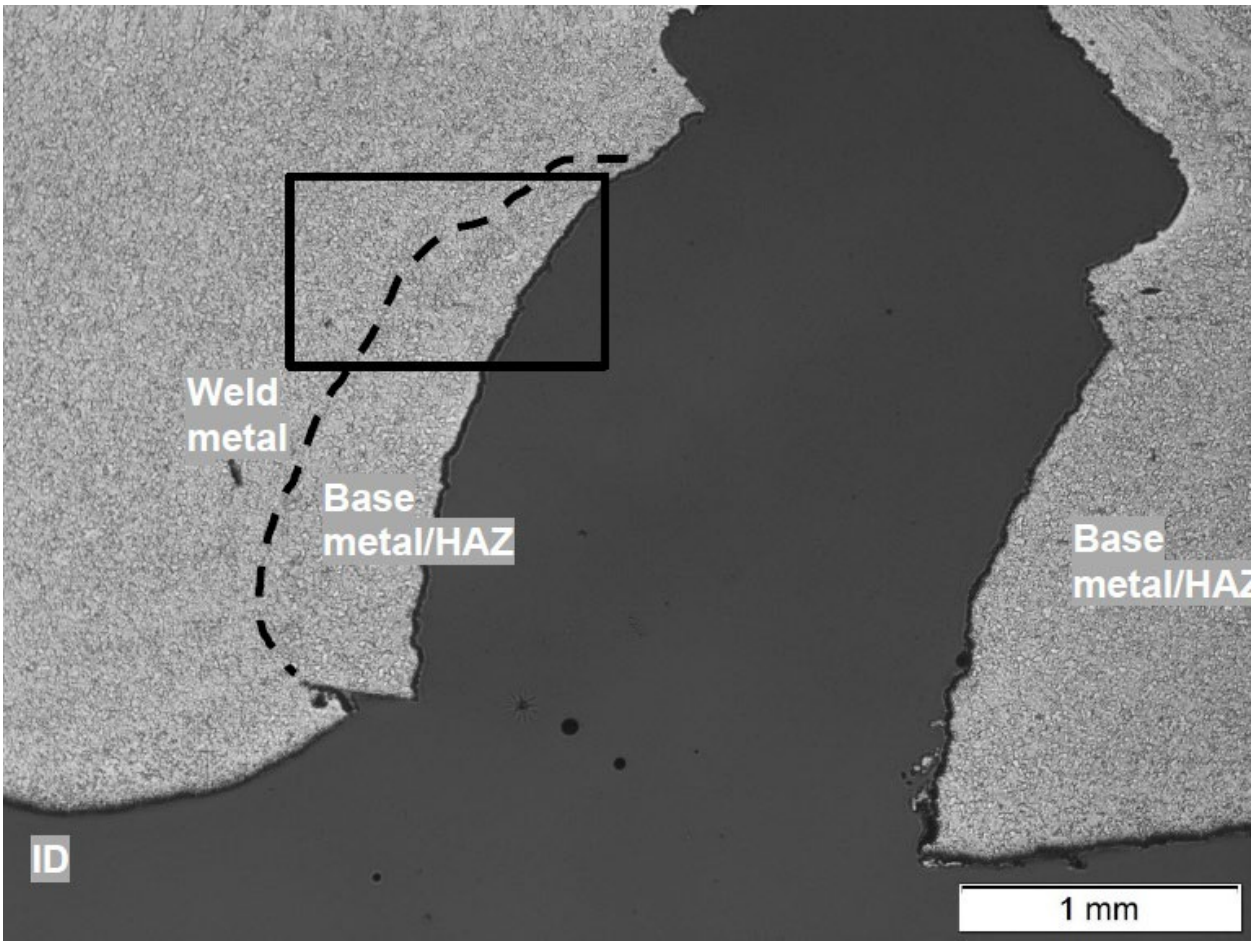

Figure 58. BF optical micrograph of the ID area of the fractured weld in Figure 57, showing the delineation of weld and base metal. The boxed area is shown in Figure 60 (~25X, etched 2% Nital).

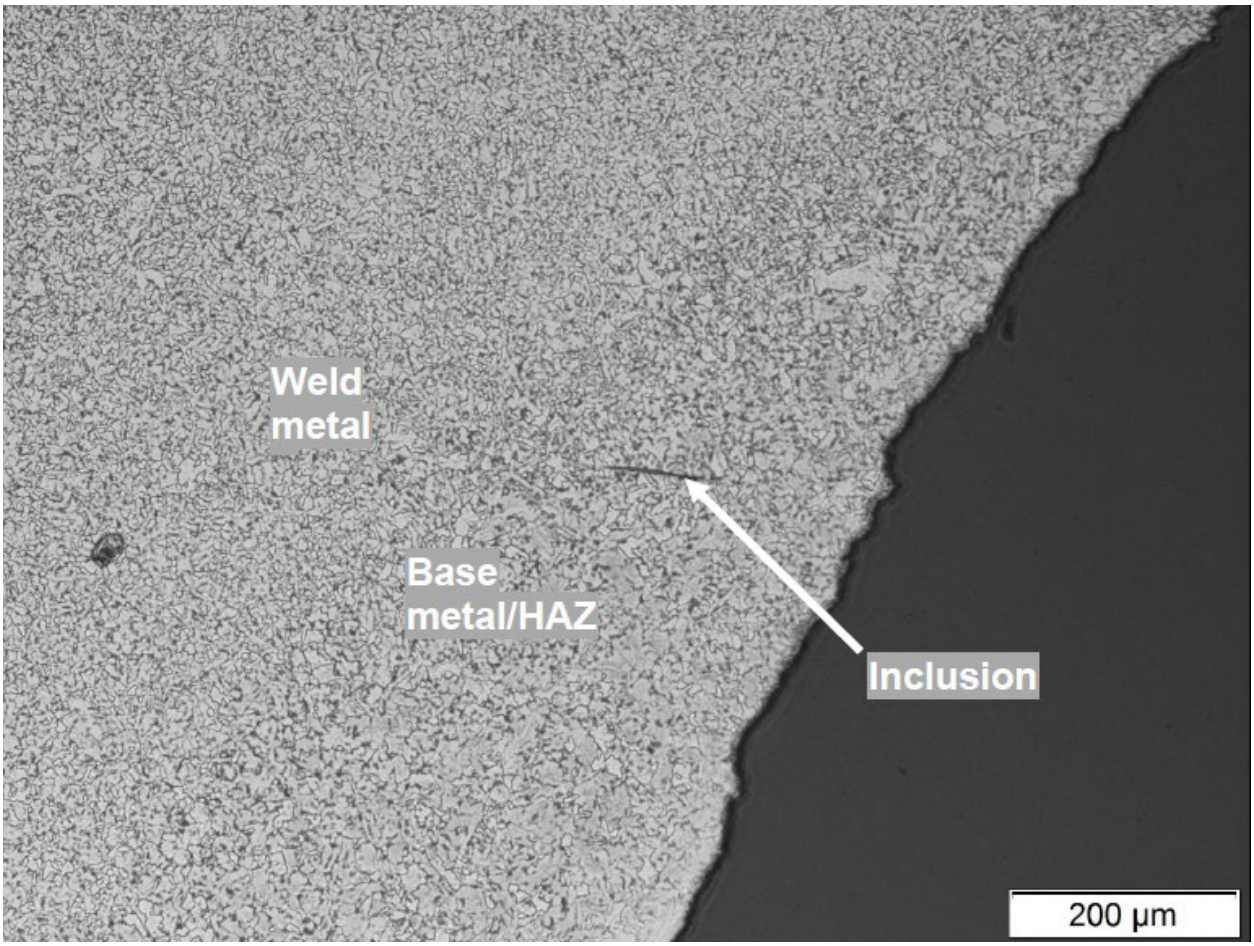

Figure 59. BF optical micrograph of the boxed area in Figure 58, showing a linear inclusion in the base metal (~100X, etched 2% Nital).

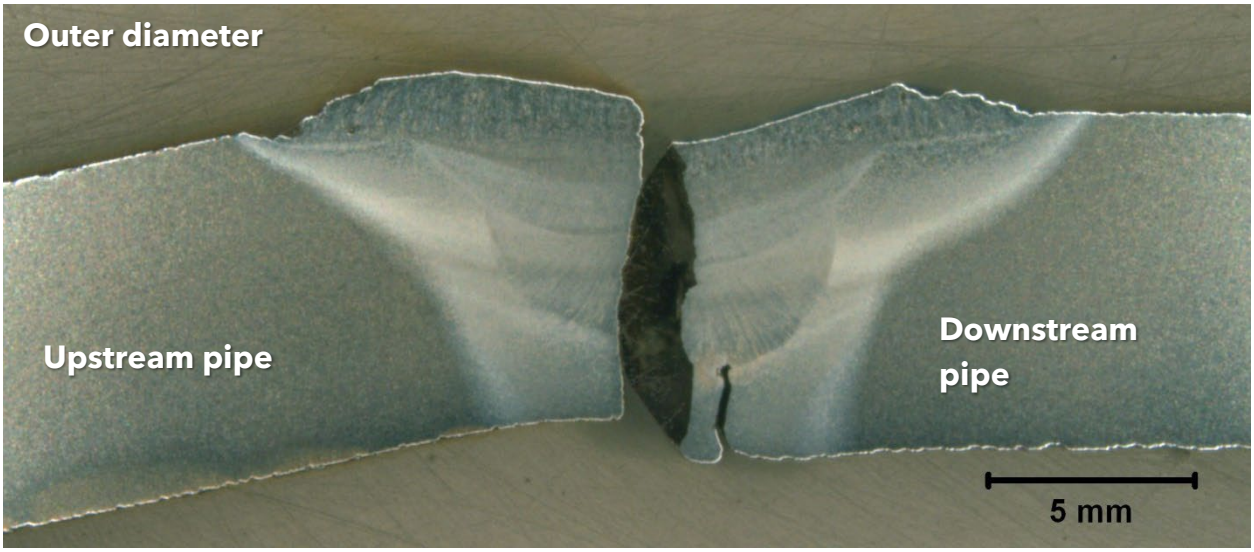

Figure 60. BF optical micrograph of the fracture at the weld at location M5_2, approximately 5.29 feet counterclockwise of top dead center (5X, etched 2% Nital).

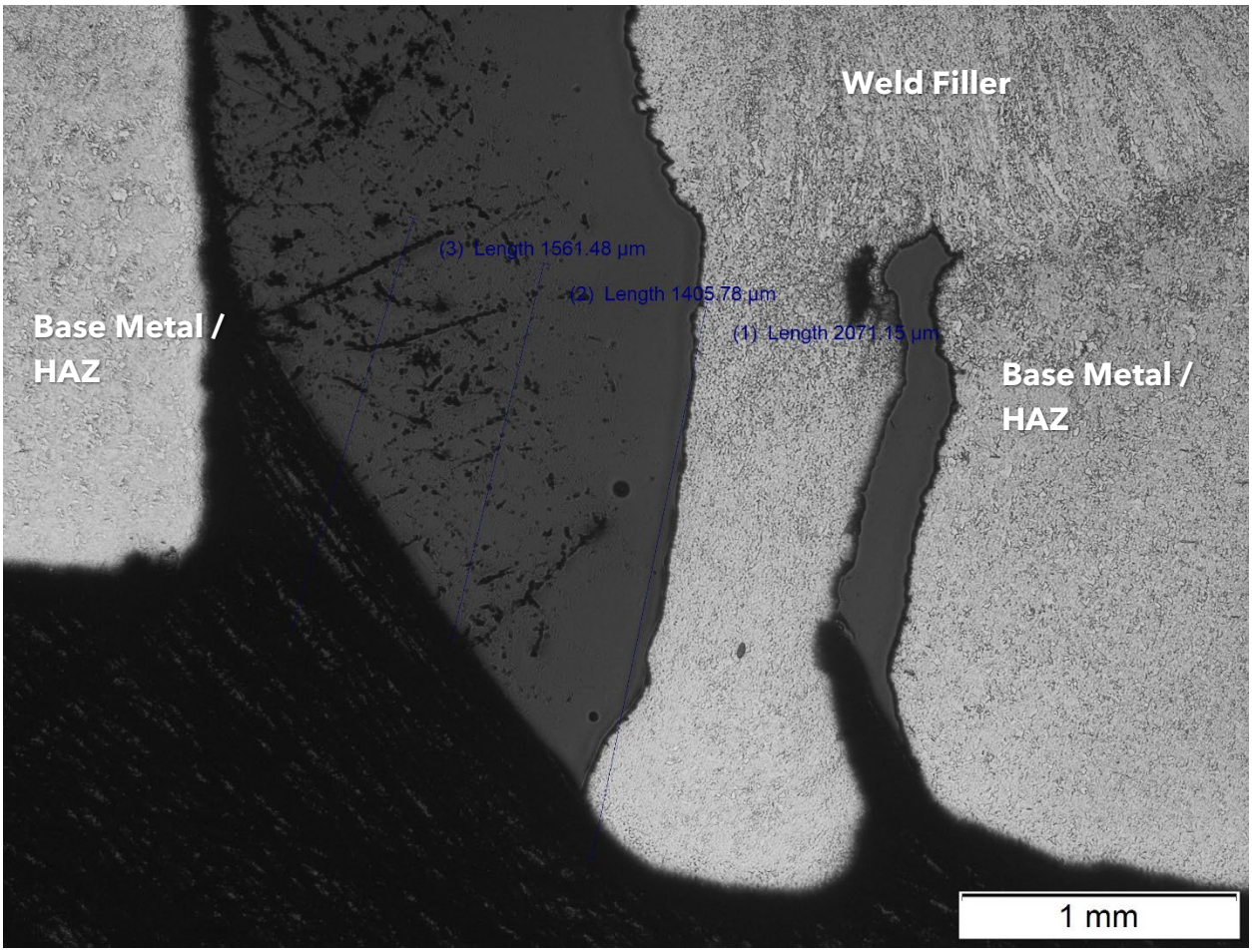

Figure 61. BF optical micrograph of weld laps on the inner diameter surface of weld M5_2 (25X, etched 2% Nital).

Figure 62. BF optical micrograph of M2C (location in Figure 6), parallel to the girth weld showing the multiple passes along the weld (~5X, etched 2% Nital).

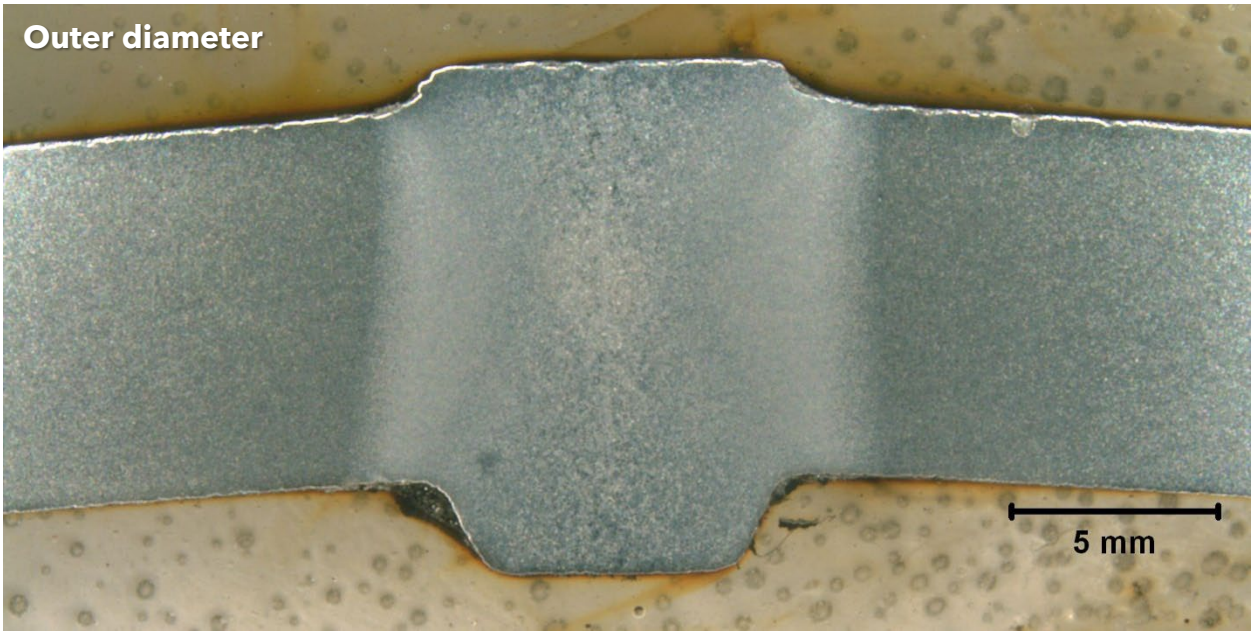

Figure 63. BF optical micrograph of the seam weld at location MS-1, sectioned across the seam weld on Pipe 1 approximately 1 inch from the upstream cut end (~5X, etched 2% Nital).

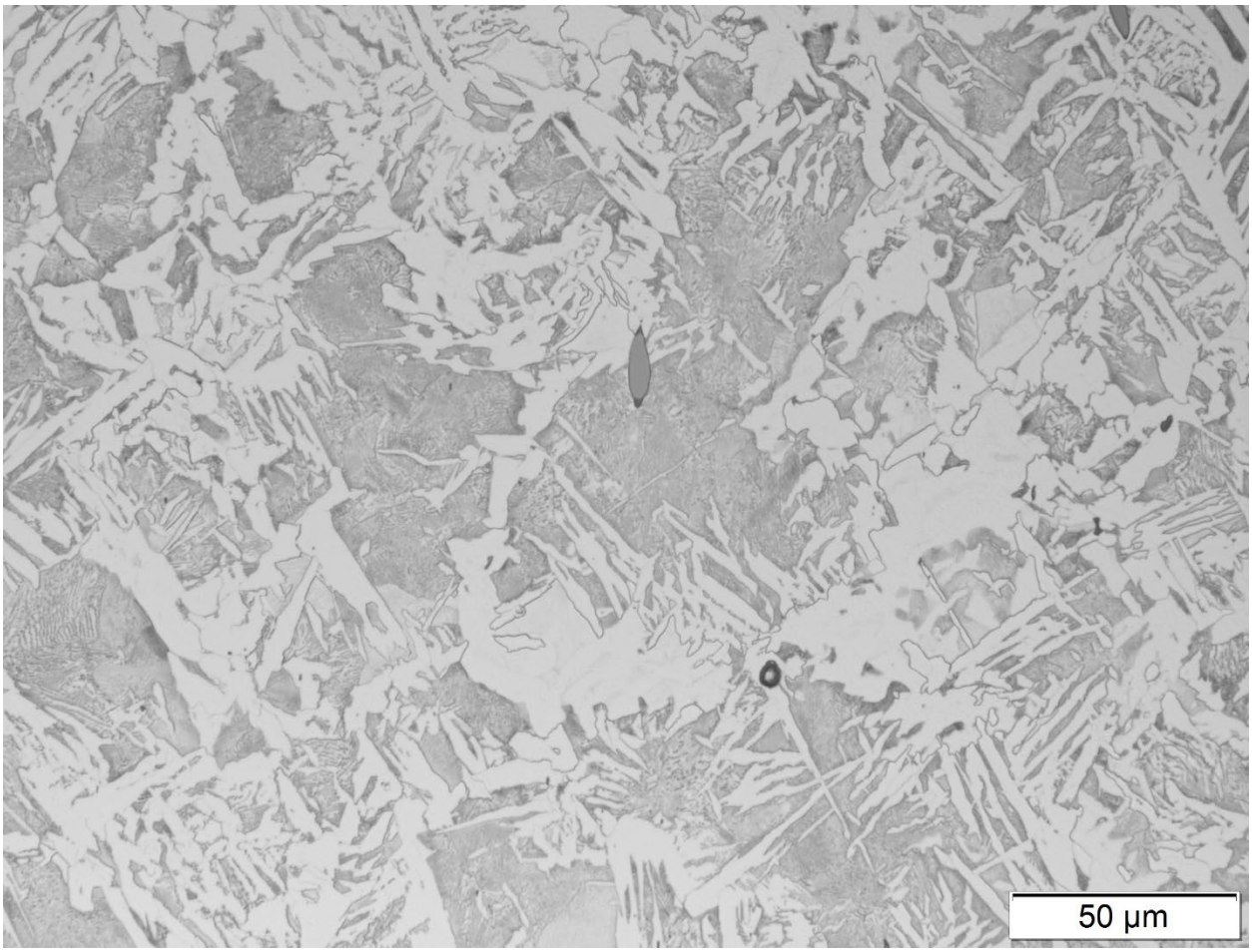

Figure 64. BF optical micrograph of a typical microstructure within the weld line of Figure 63 along the bond line (~400X, etched 2% Nital).

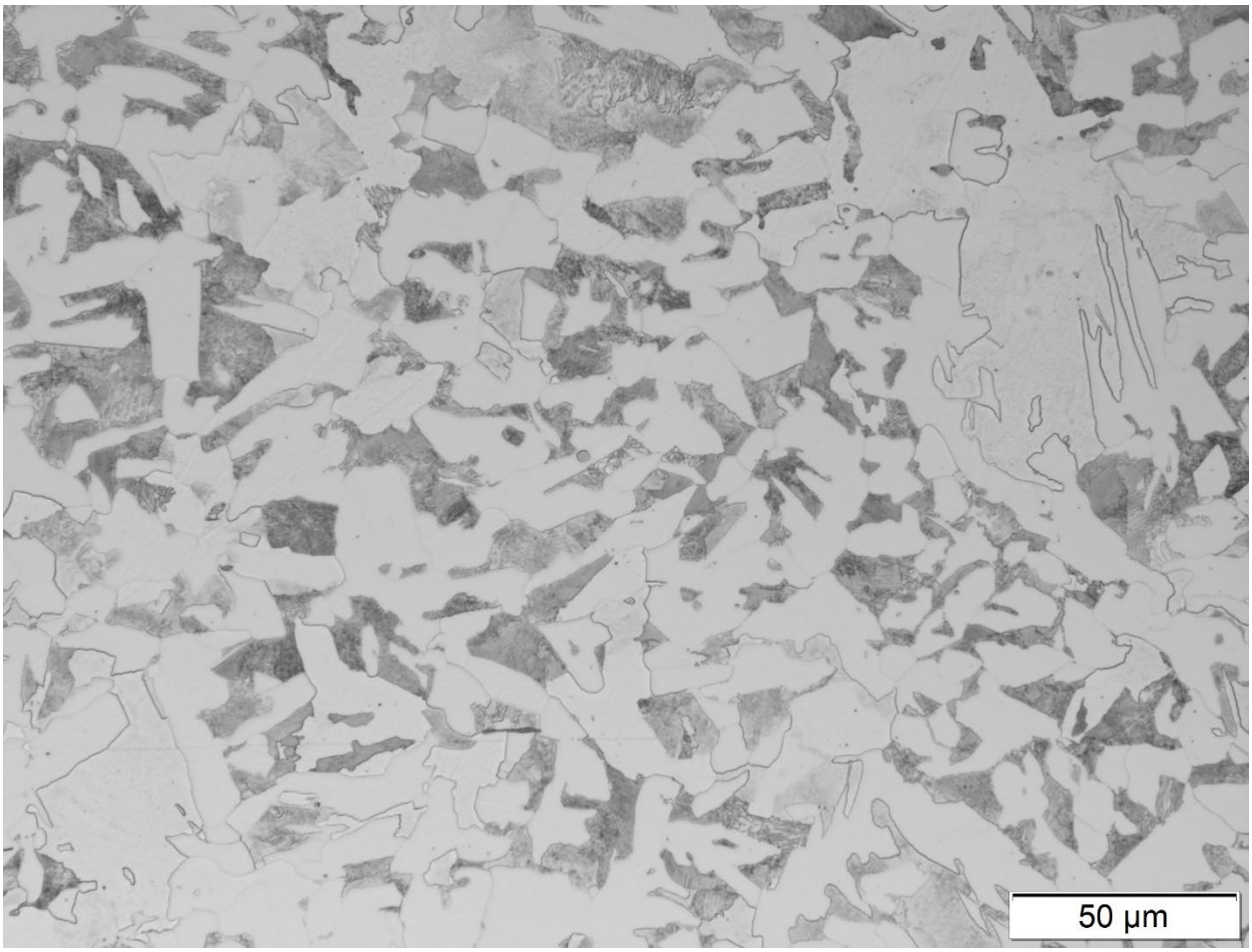

Figure 65. BF optical micrograph of a typical microstructure within the heat affected zone of Figure 63 (~400X, etched 2% Nital).

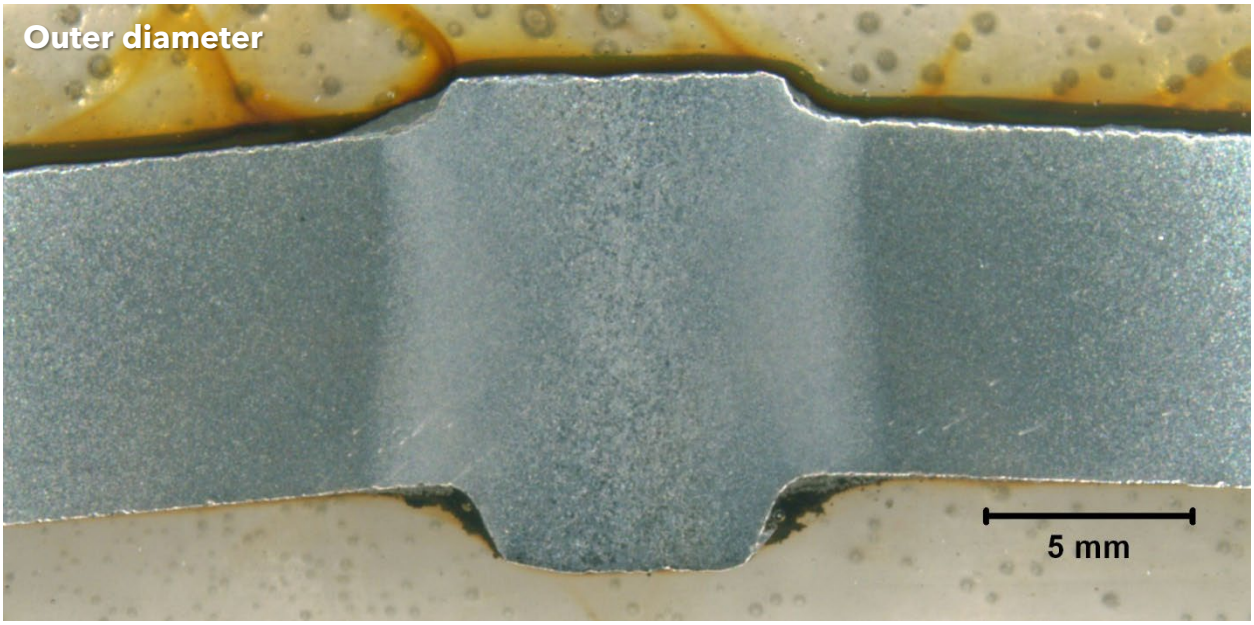

Figure 66. BF optical micrograph of the seam weld at location MS-2, sectioned from the seam weld 4.25 feet from the upstream girth weld end of Pipe 2 (~5X, etched 2% Nital).

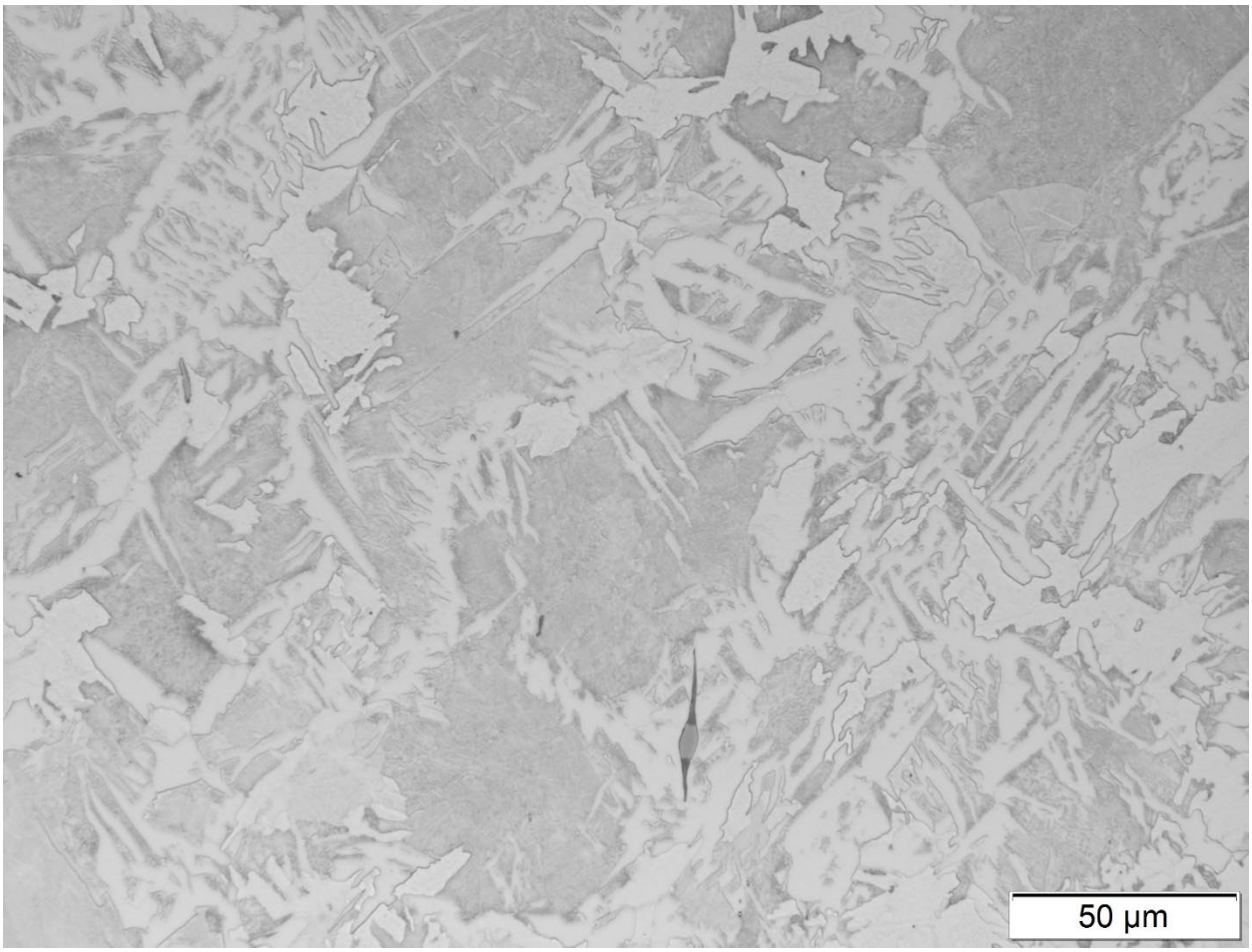

Figure 67. BF optical micrograph of a typical microstructure within the weld of Figure 66 (400X, etched 2% Nital).

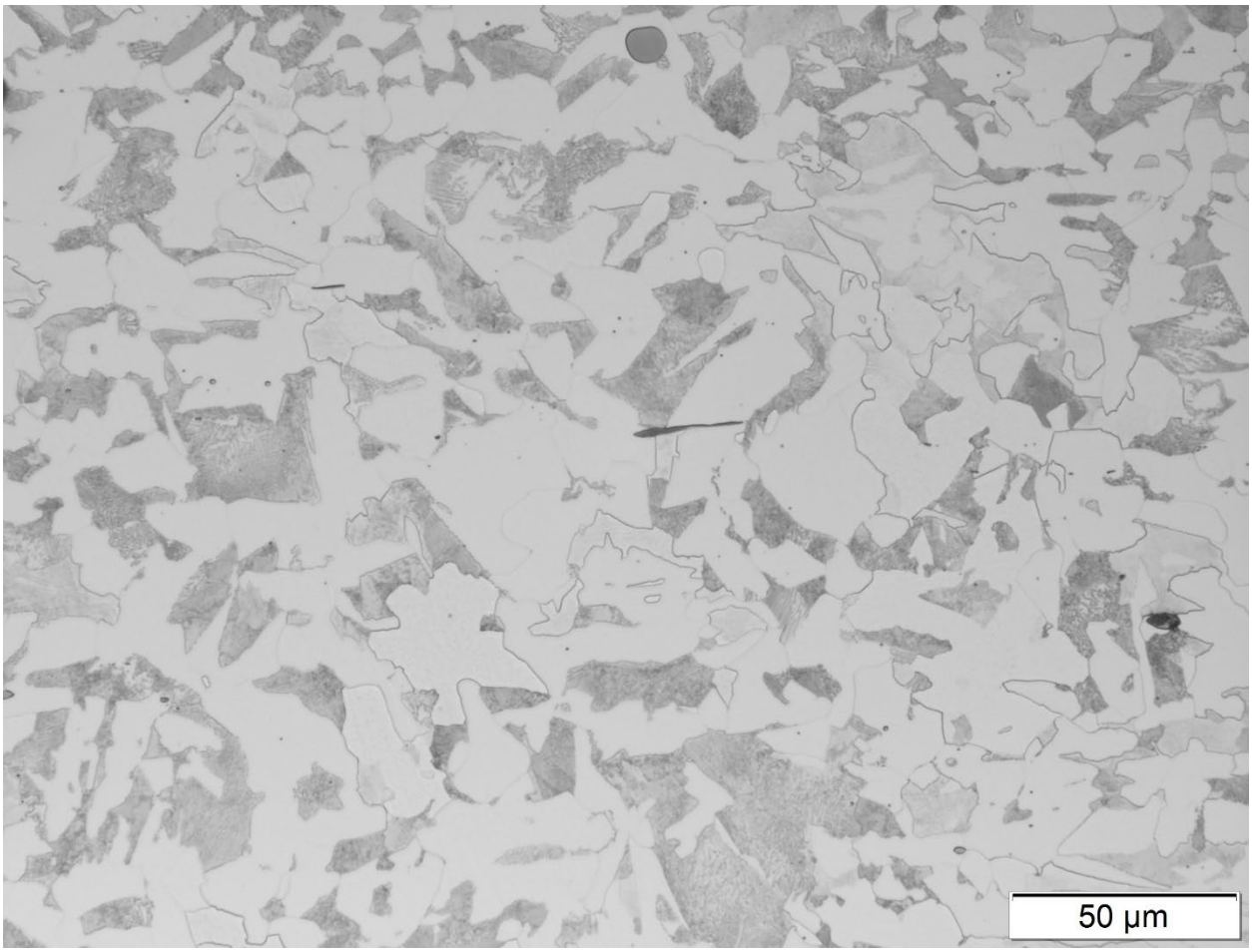

Figure 68. BF optical micrograph of a typical microstructure within the heat affected zone of Figure 66 (400X, etched 2% Nital).

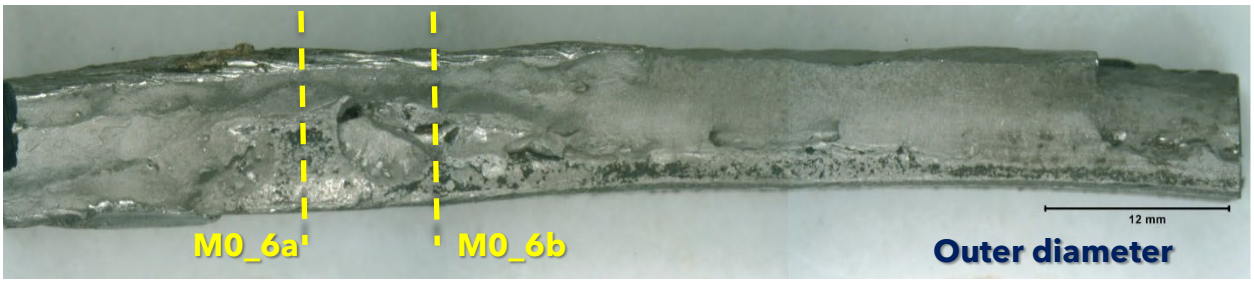

Figure 69. View of a sectioned and cleaned area of the Pipe 2 fracture (location 0_6), mating the side shown in Figure 10.

Inner diameter

Figure 70. Closer view of the left edge of the Pipe 2 fracture surface section at 1:15 o clock position, shown in Figure 69.

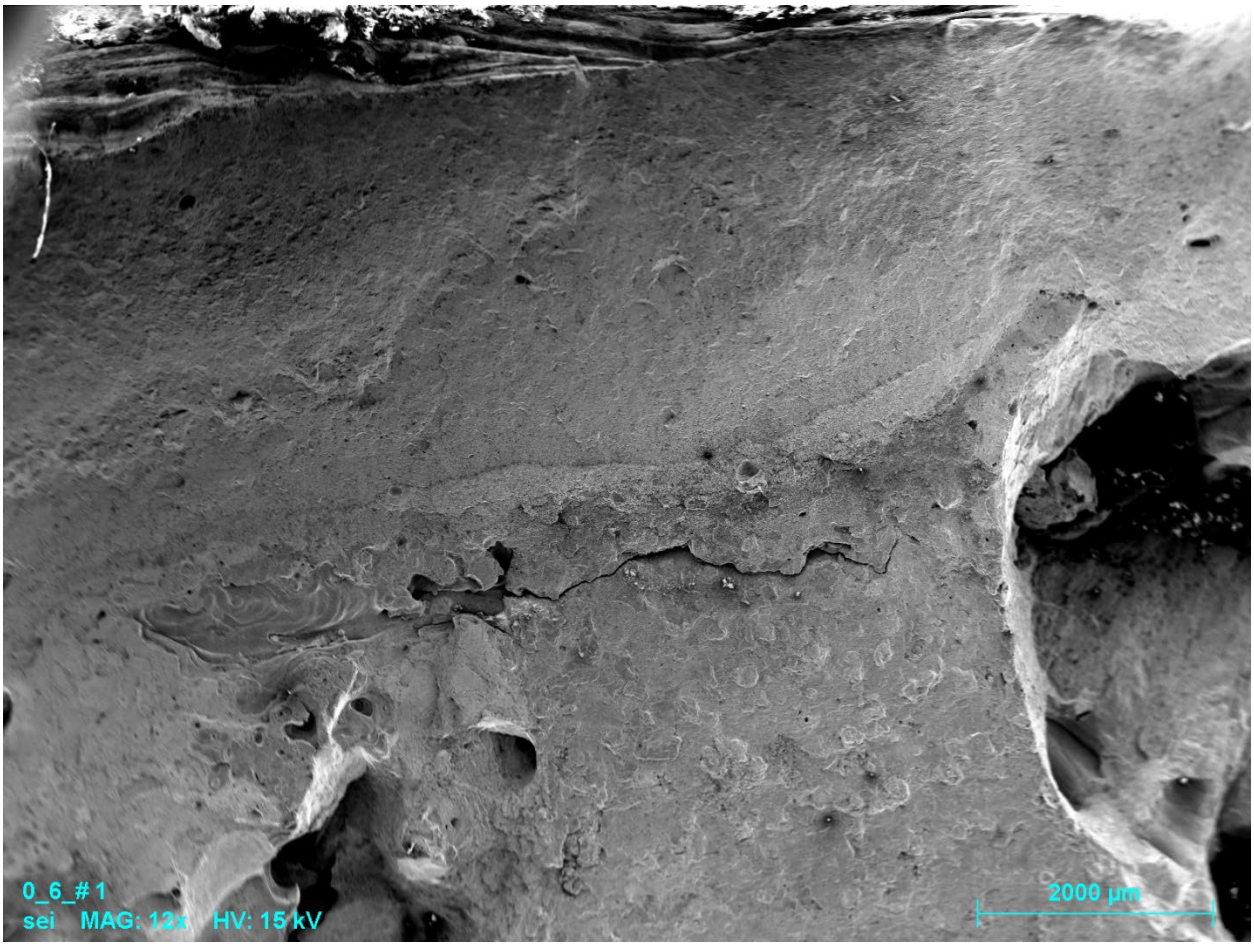

Figure 71. Secondary electron (SE) micrograph of the area towards the right in Figure 70.

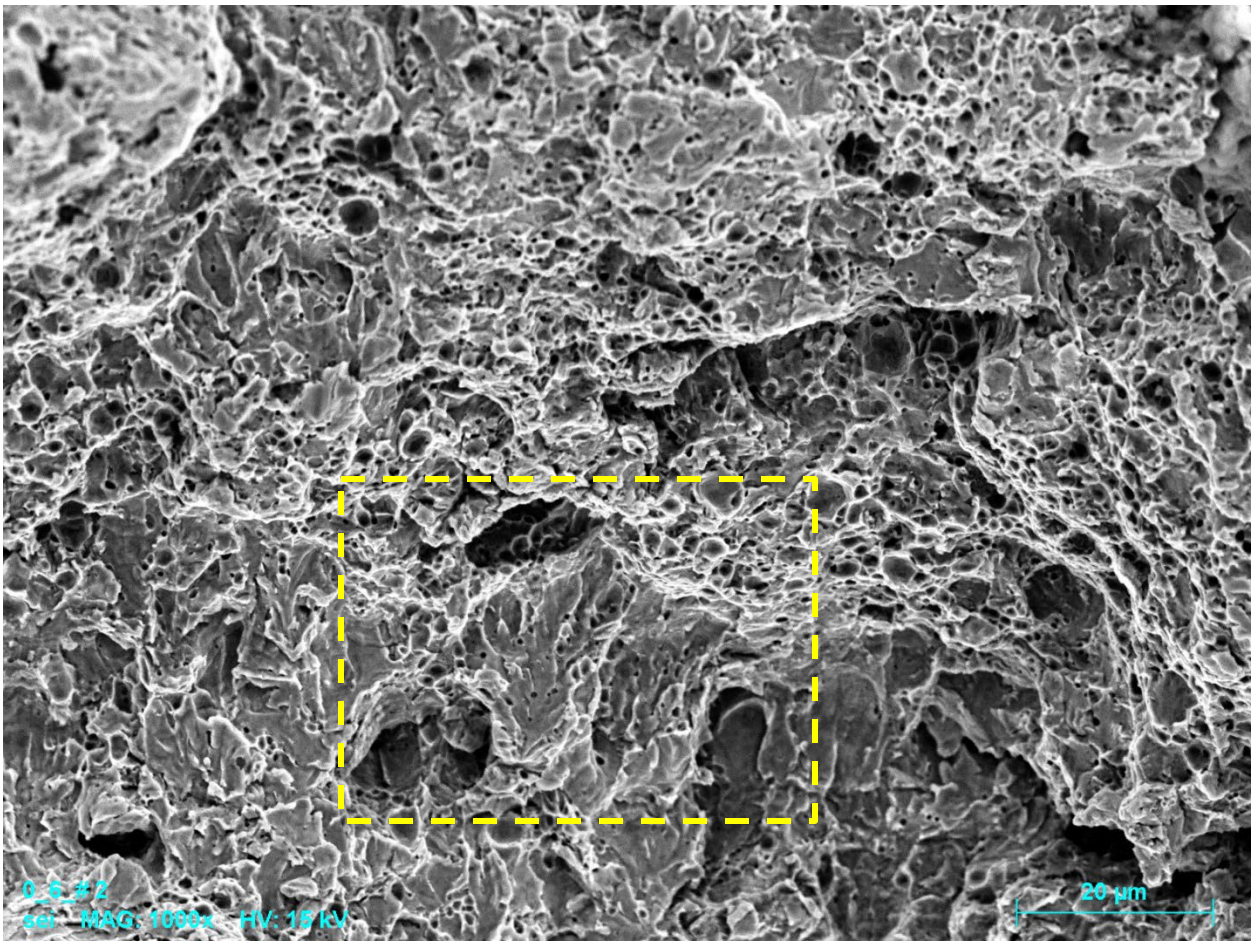

Figure 72. SE micrograph of a typical area in the upper half of the fracture in Figure 71, showing dimpled rupture and cleavage.

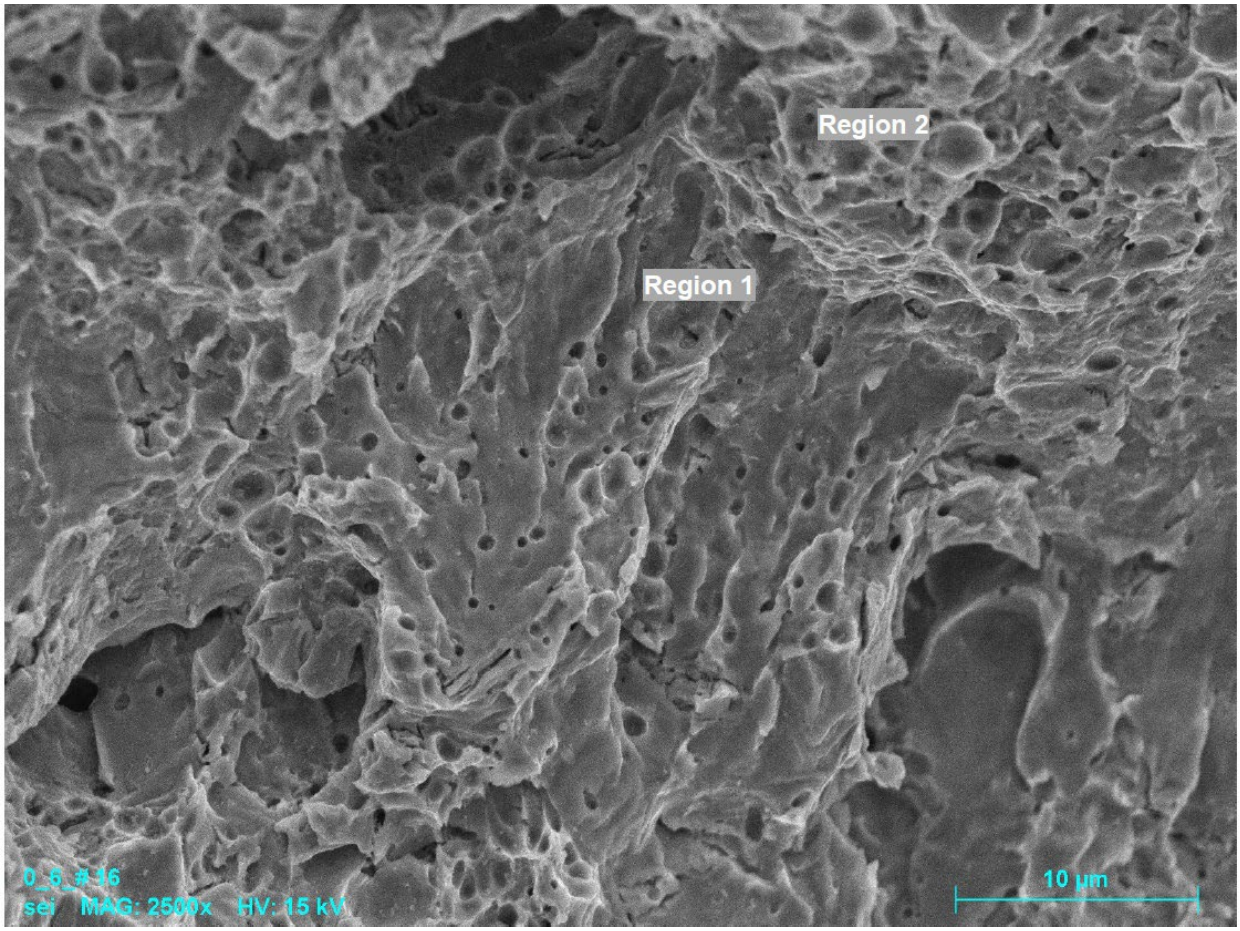

Figure 73. SE micrograph of the boxed area in Figure 72, showing the delineation between cleavage (Region 1) and dimpled rupture (Region 2).

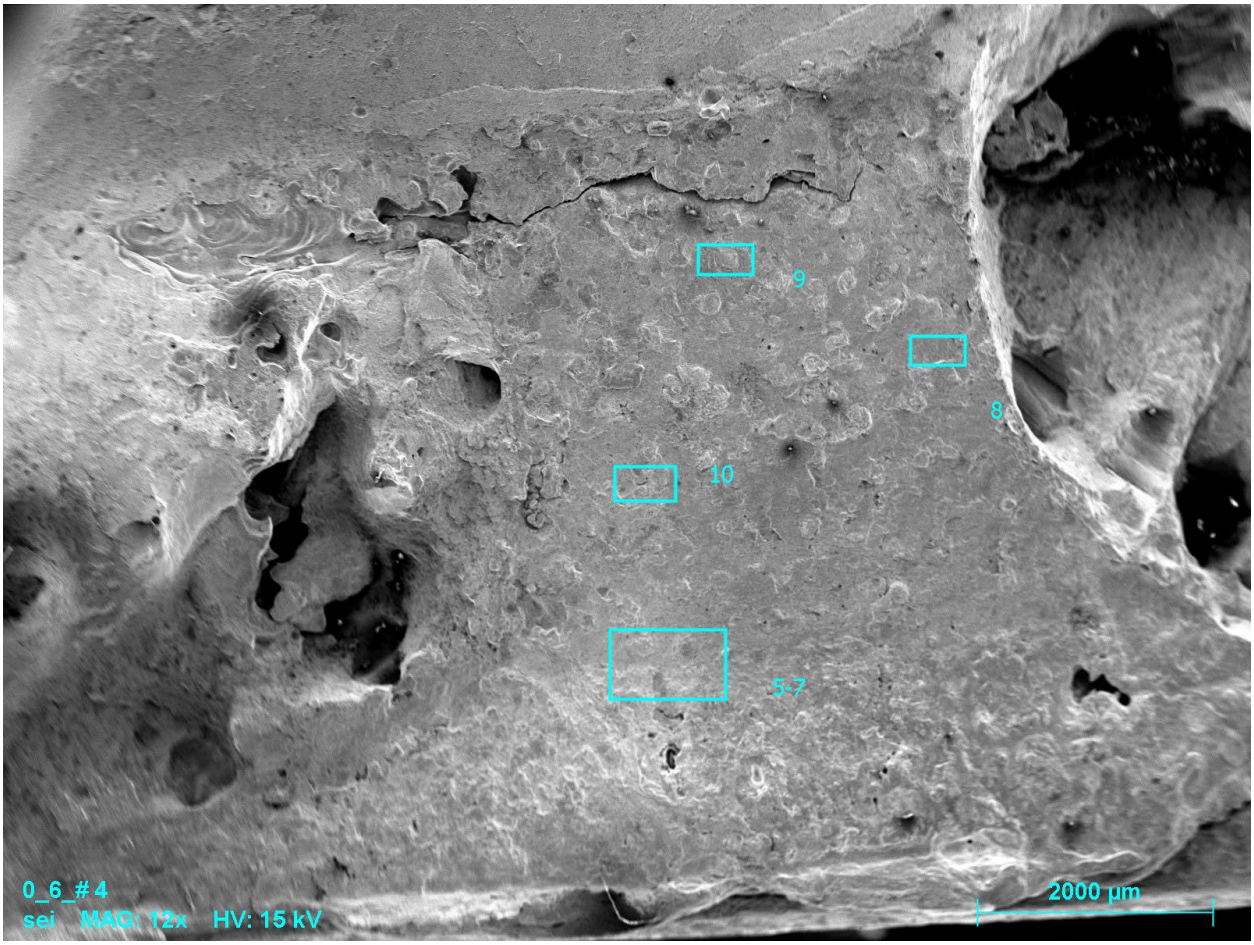

Figure 74. SE micrograph of the area in Figure 71, annotated to show areas examined closer.

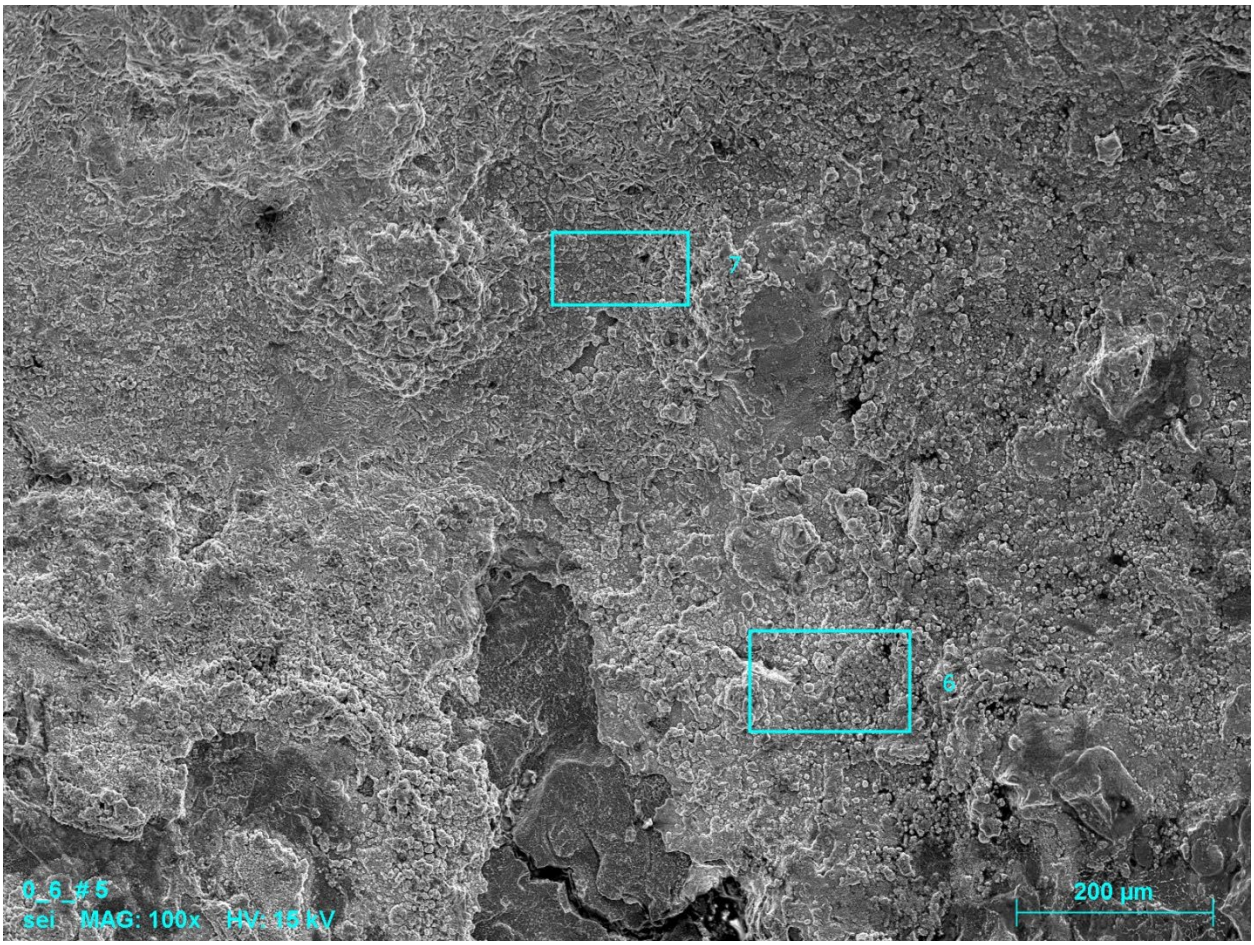

Figure 75. SE micrograph of boxed area "5-7' in Figure 74.

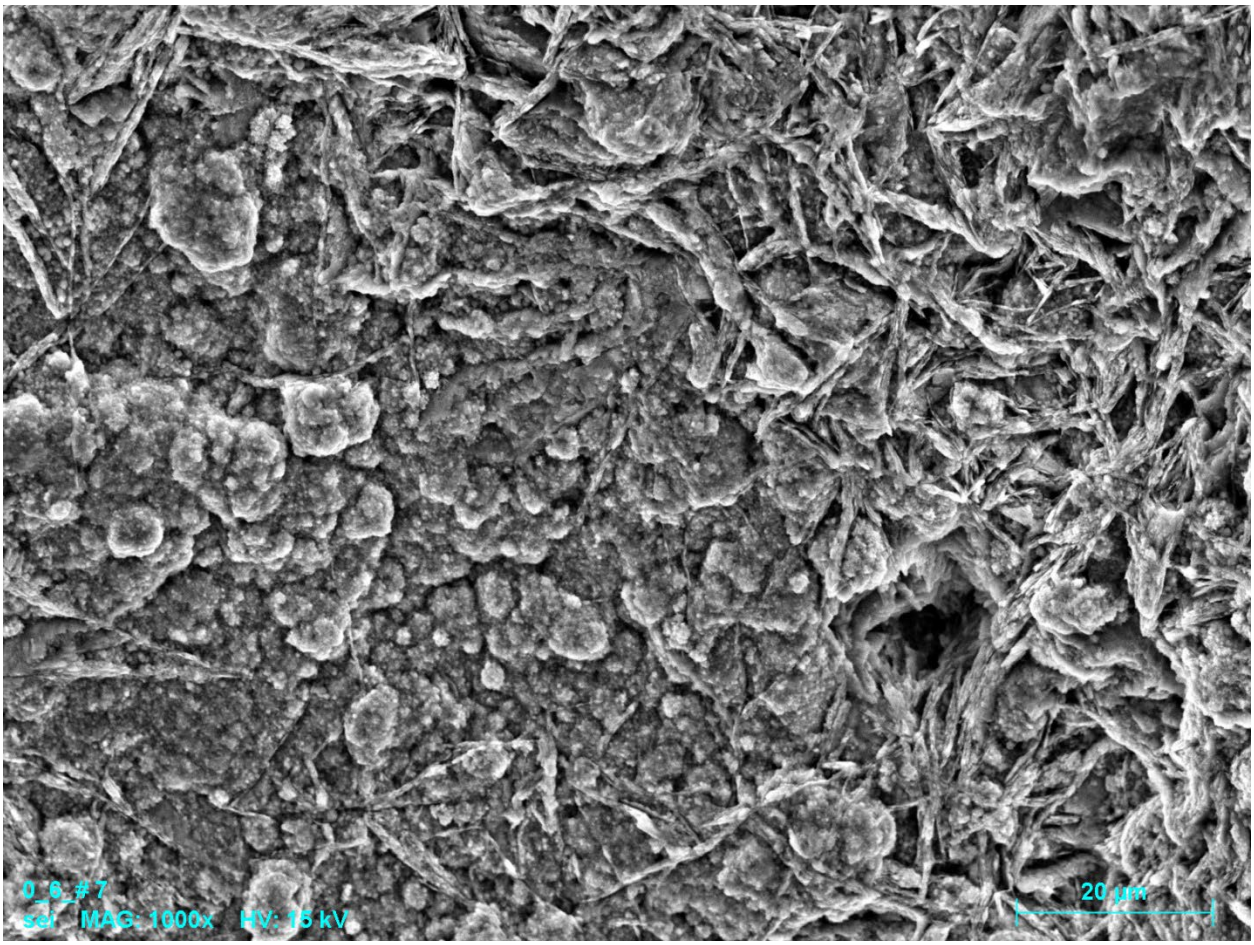

Figure 76. SE micrograph of boxed area “7” in Figure 75.

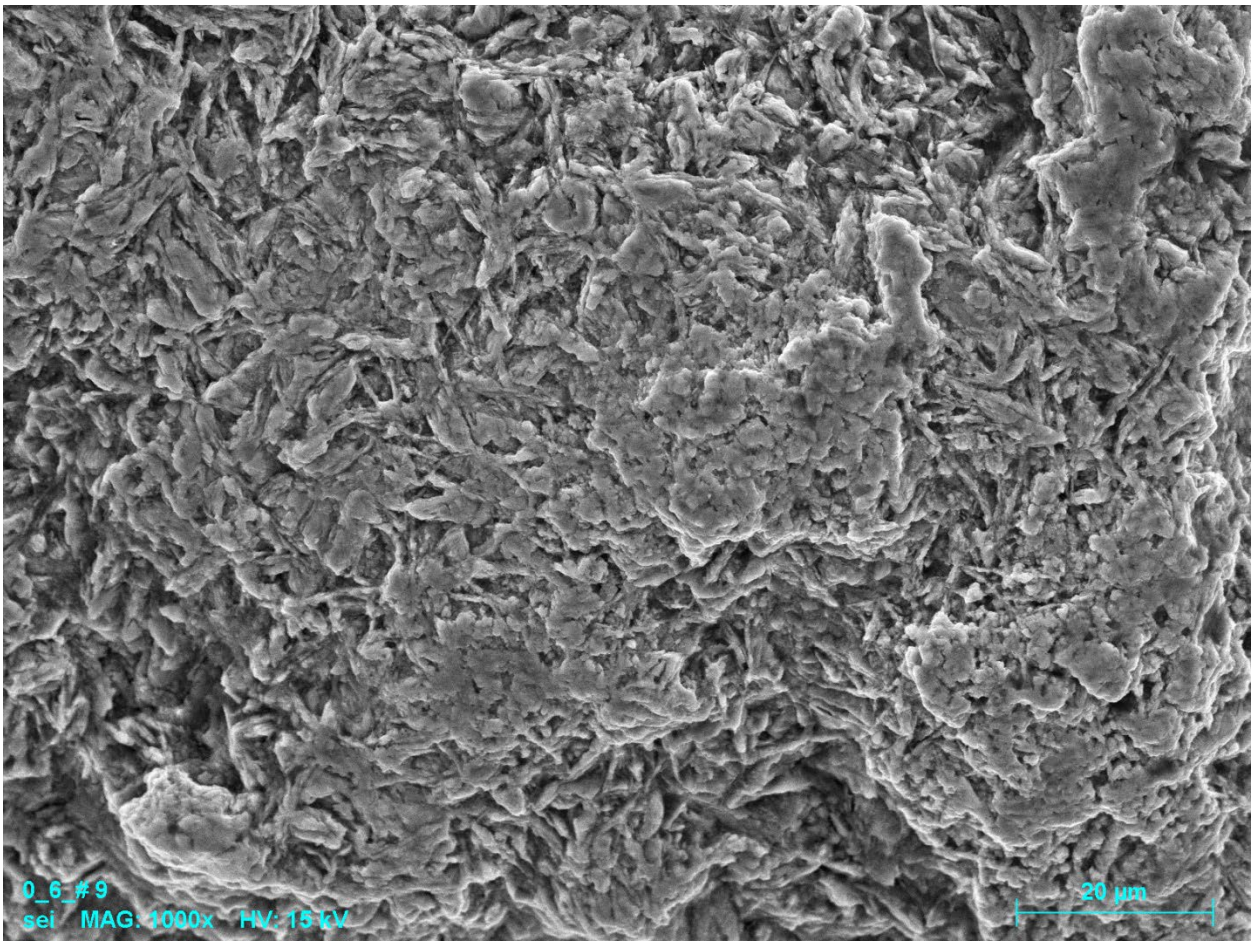

Figure 77. SE micrograph of the boxed area “9” in Figure 74.

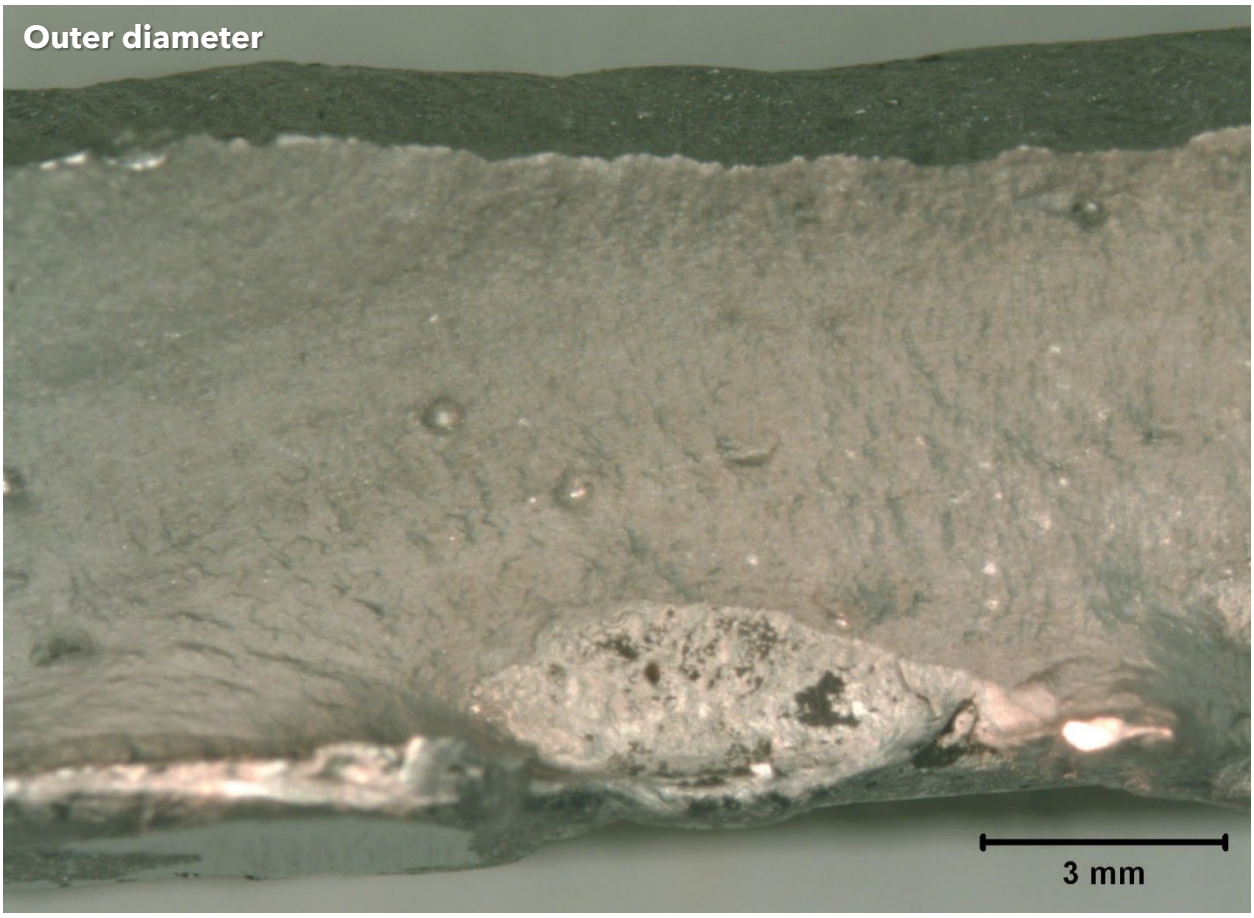

Figure 78. Area of the Pipe 2 fracture surface with a convex discontinuity near the ID edge.

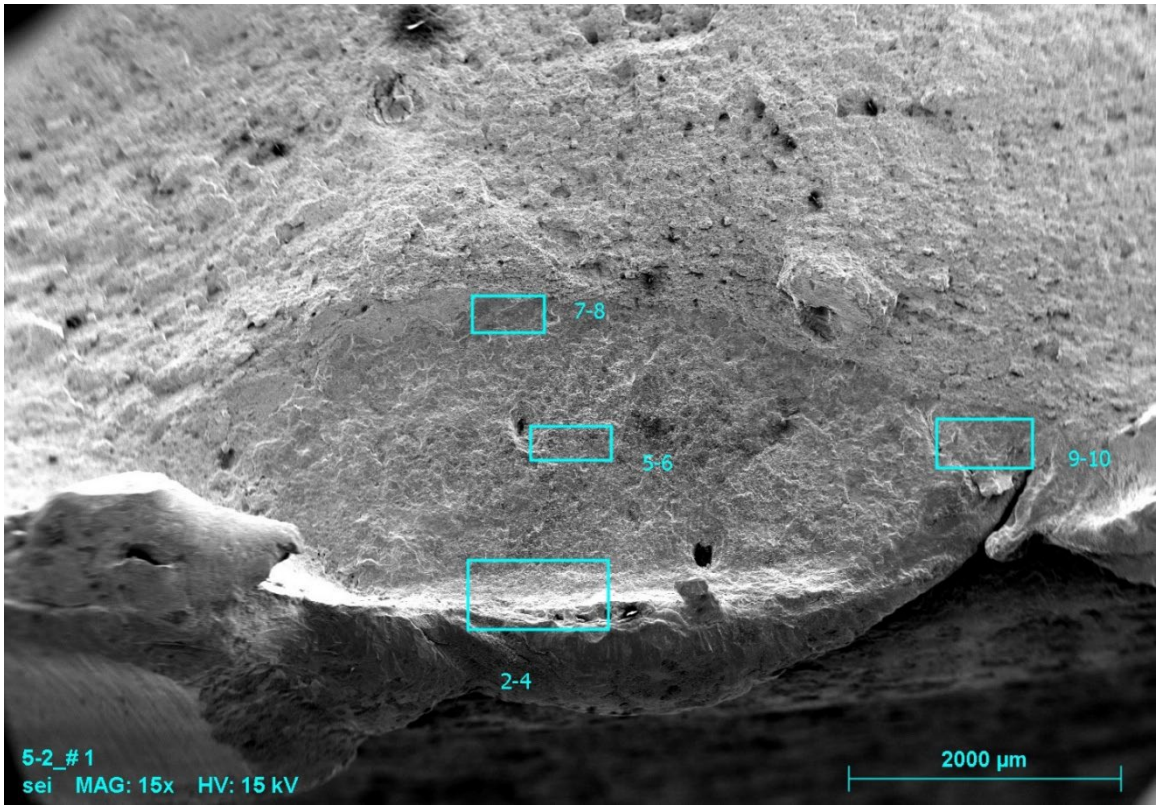

Figure 79. SE micrograph of the area in Figure 78 examined prior to surface oxide removal.

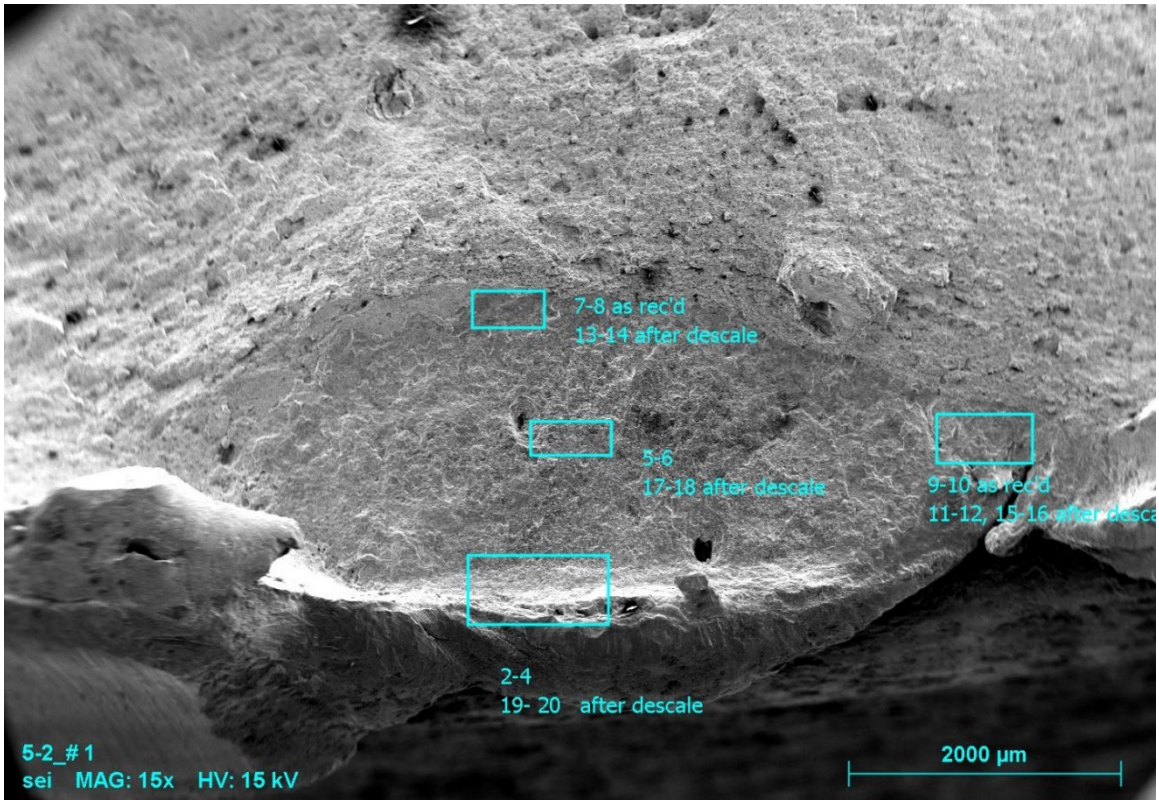

Figure 80. SE micrograph of the area in Figure 78 examined after surface oxide removal.

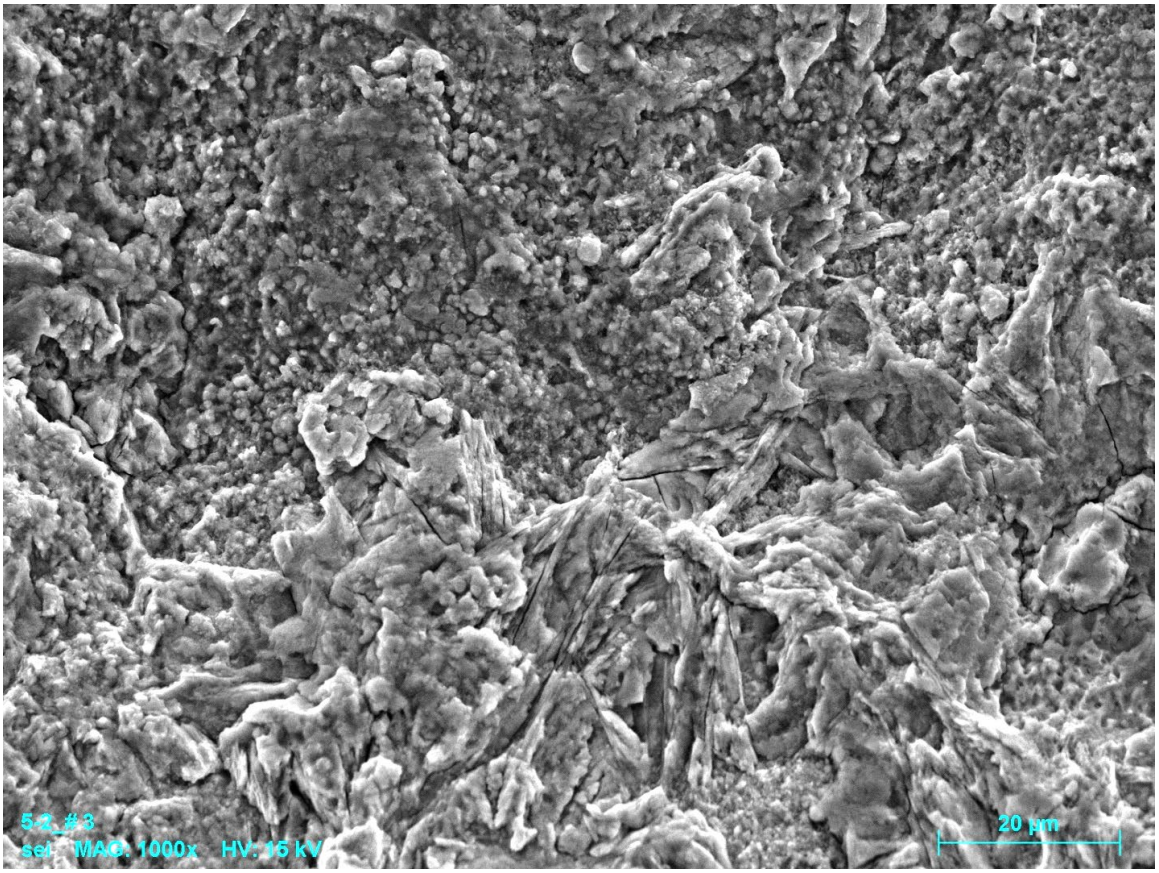

Figure 81. SE micrograph of location 3 in Figure 79, prior to oxide removal.

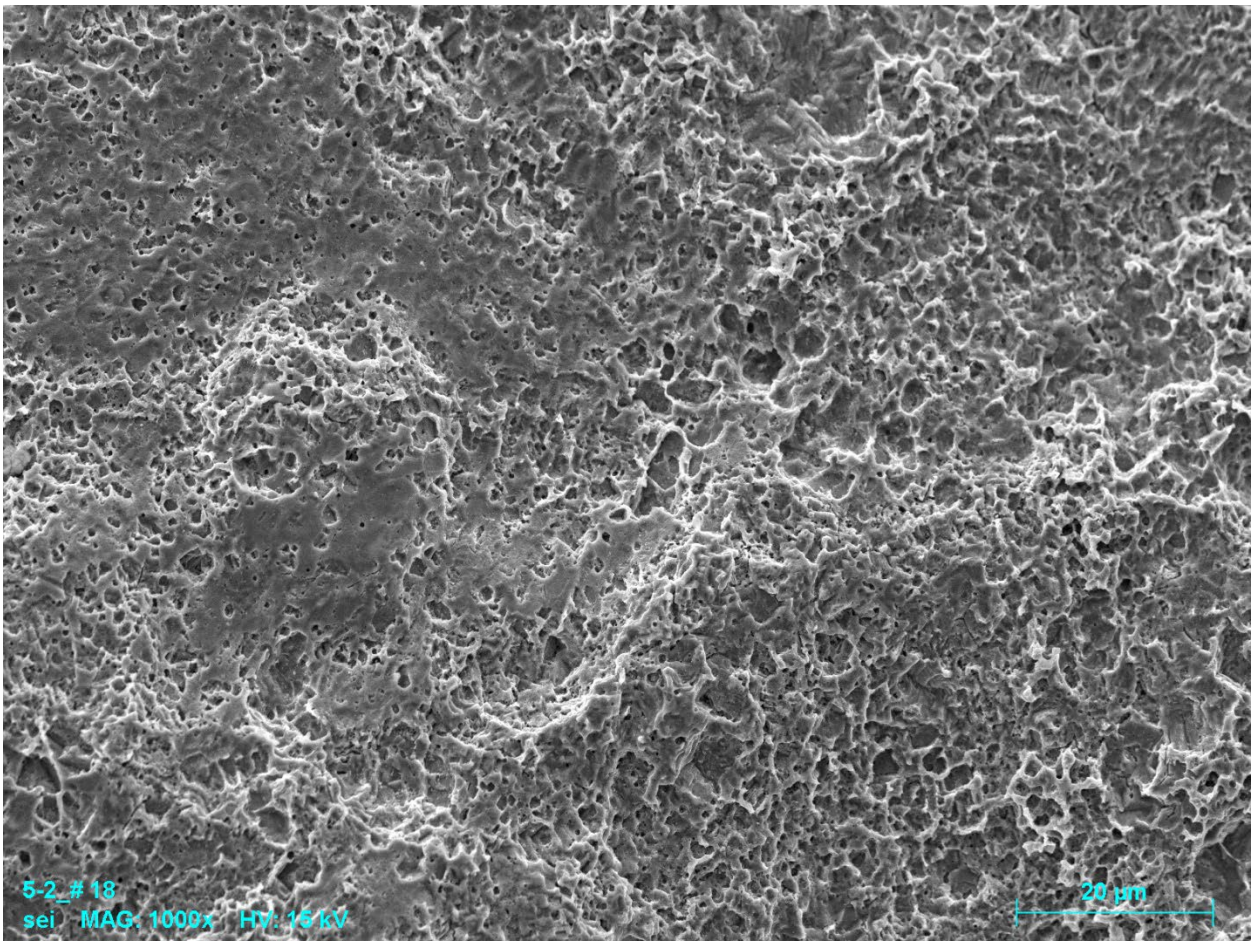

Figure 82. SE micrograph of location 18 in Figure 80, after oxide removal.

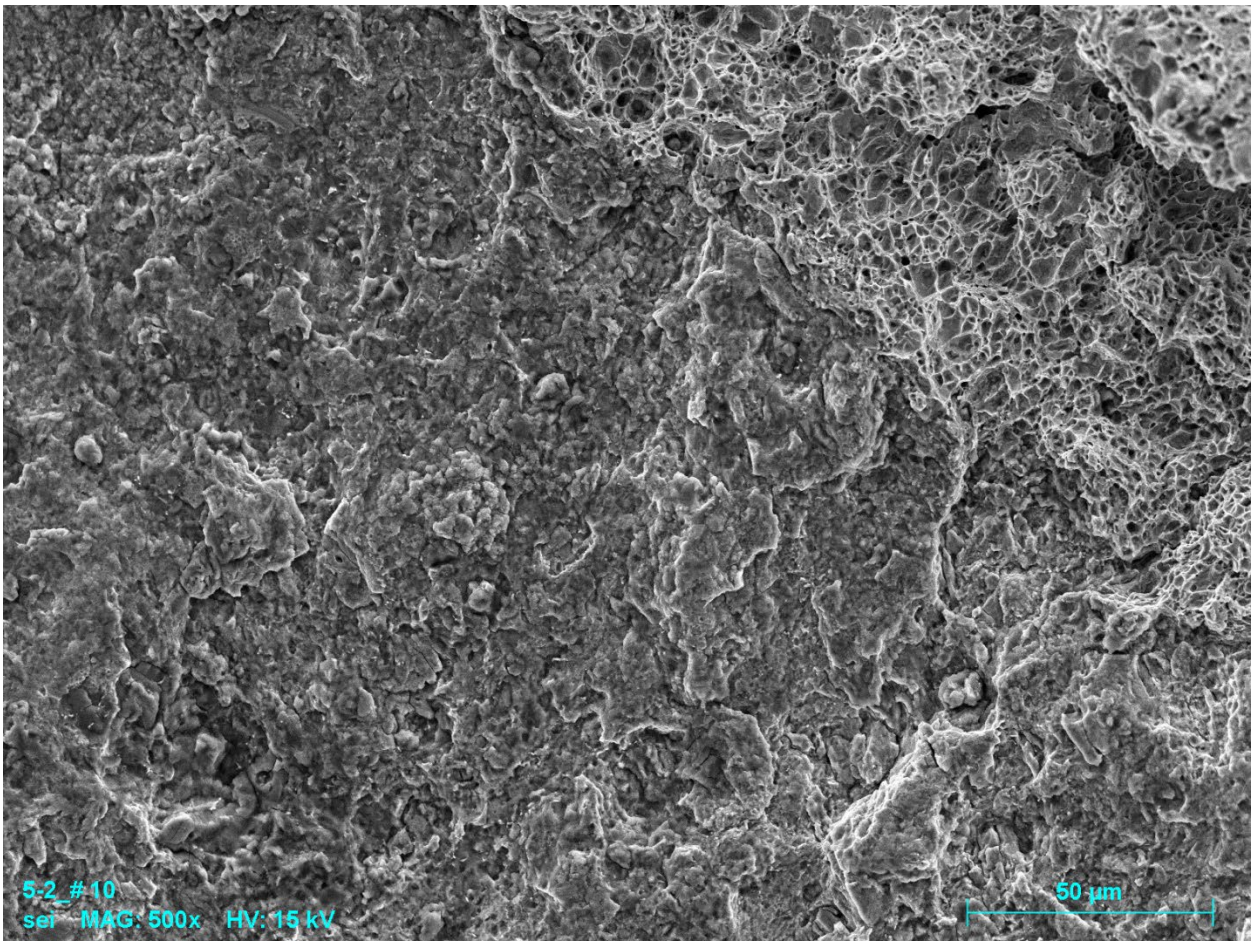

Figure 83. SE micrograph of location 10 in Figure 79, prior to oxide removal.

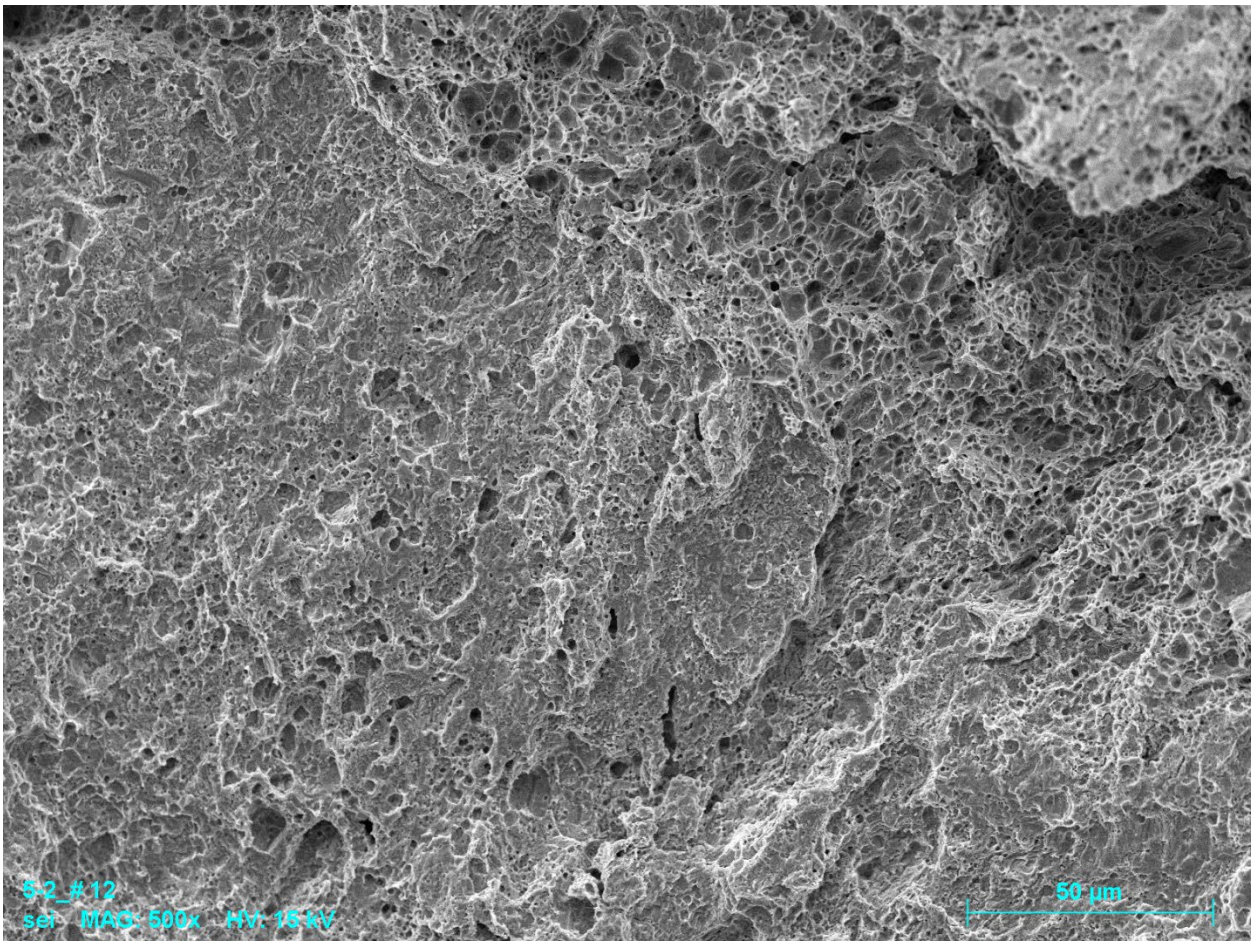

Figure 84. SE micrograph of location 12 in Figure 80, after oxide removal.

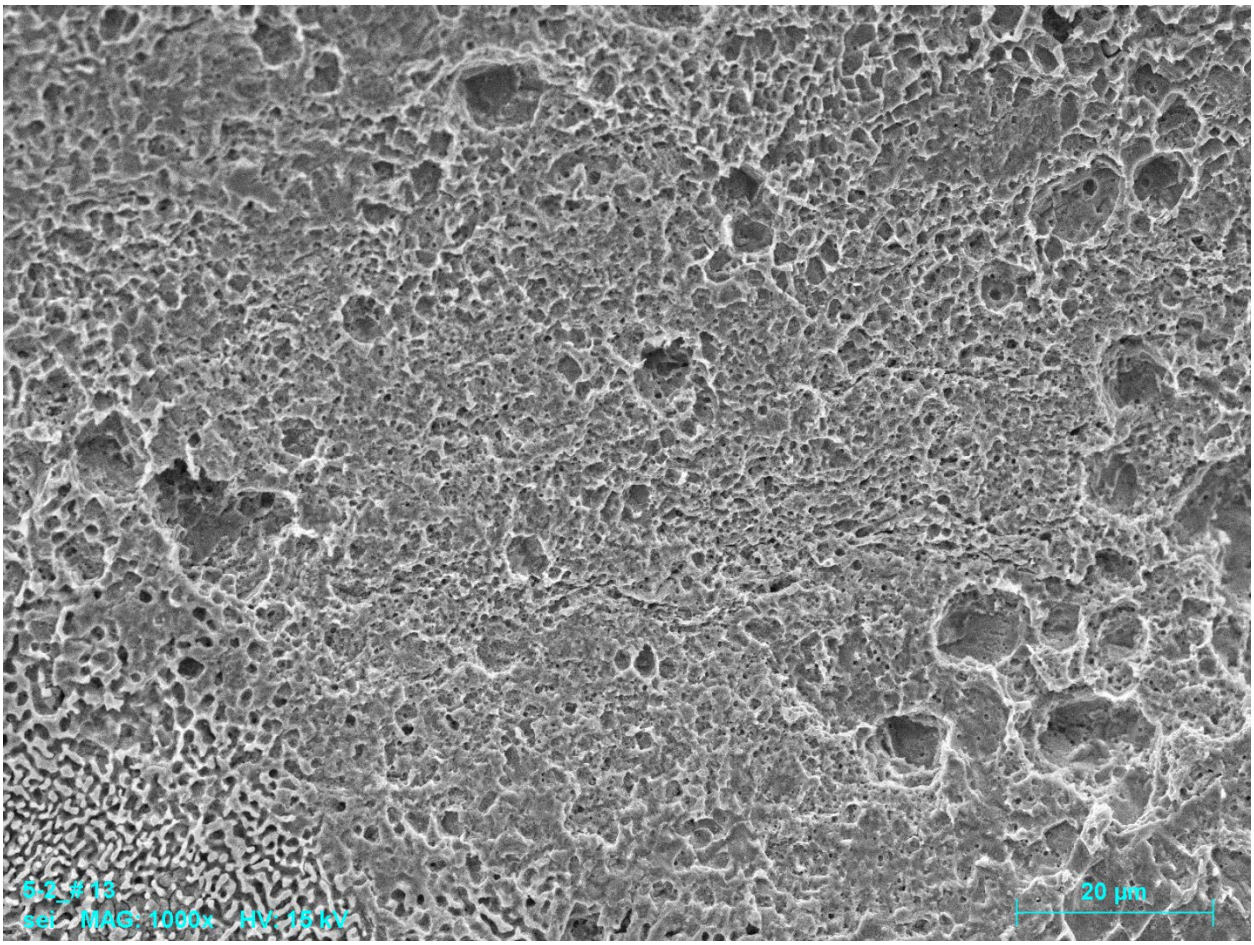

Figure 85. SE micrograph of location 13 in Figure 80, after oxide removal.

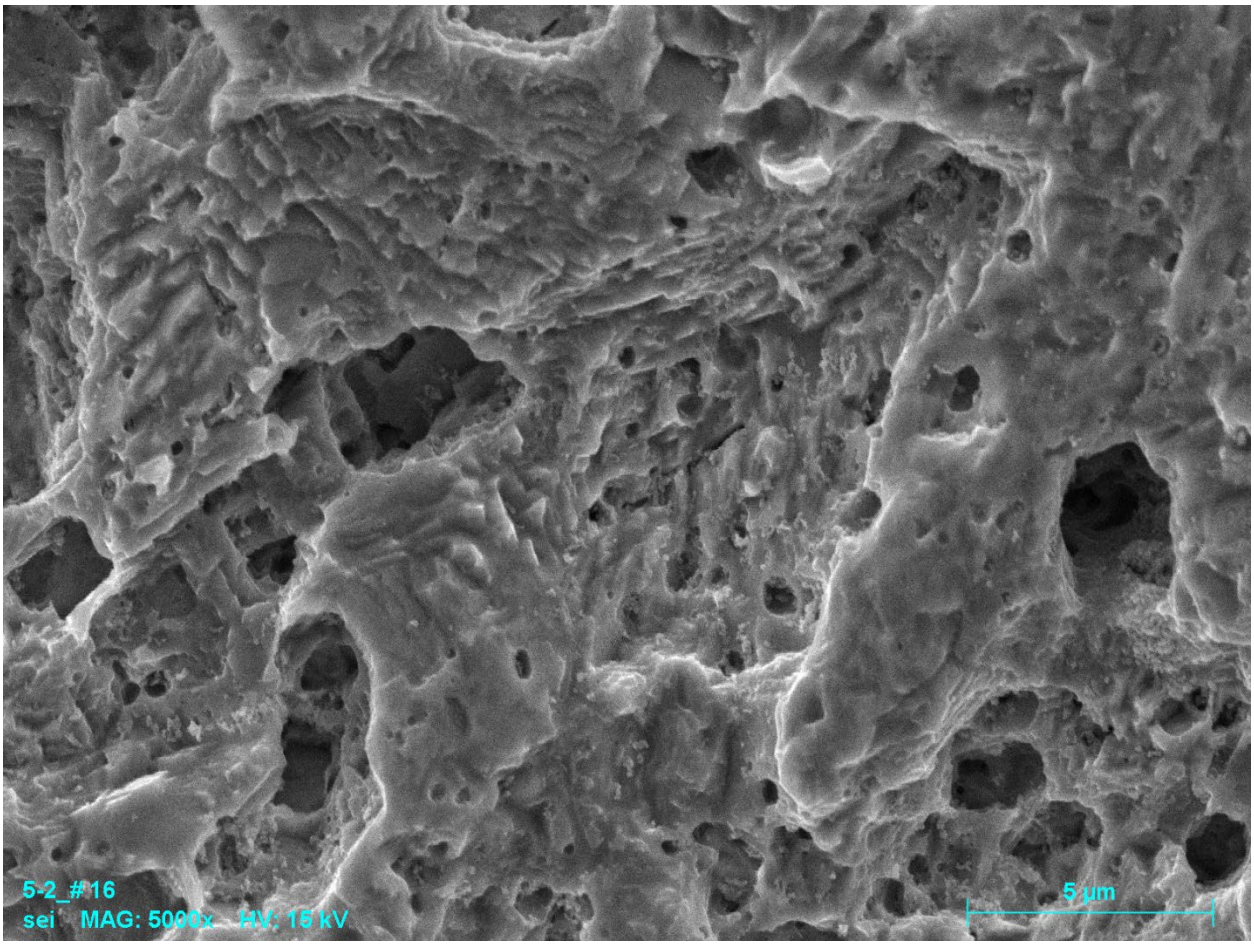

Figure 86. SE micrograph of location 16 in Figure 80, after oxide removal.

Figure 87. Montage of the radiographs from the girth weld of Pipe 3. The 0 represents 12 o'clock top dead center, with the remaining numbers indicating distances clockwise in inches. The seam welds are visible between the 5 and 10 locations.

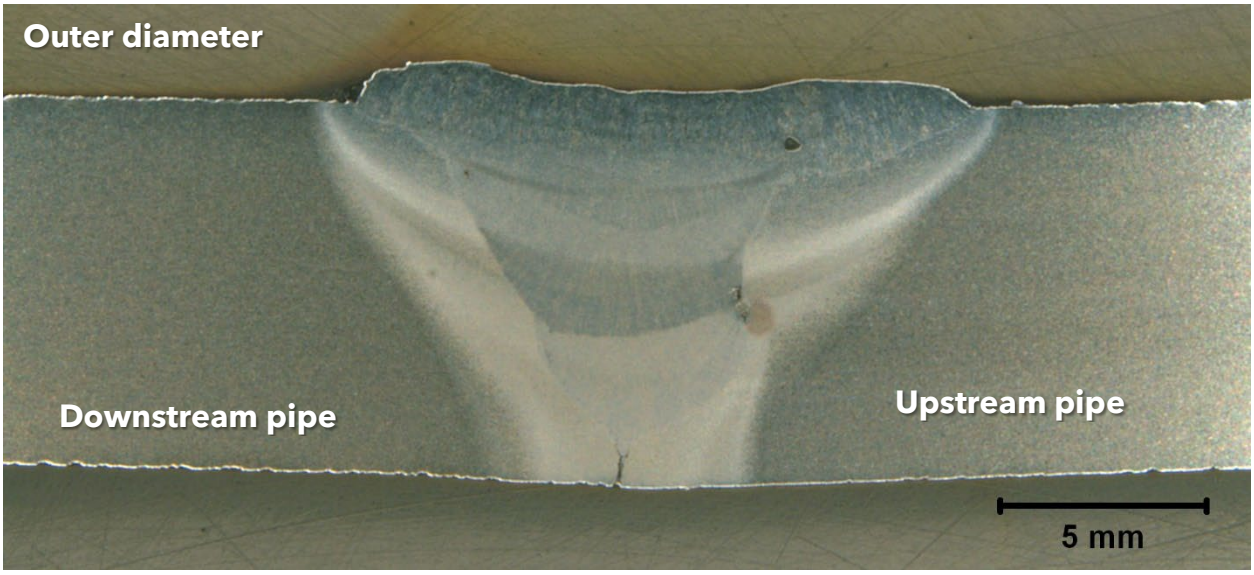

Figure 88. BF optical micrograph of the Pipe 3 girth weld at location M3-1, removed 1.06 clockwise of 12 o'clock top dead center (5X, etched 2% Nital).

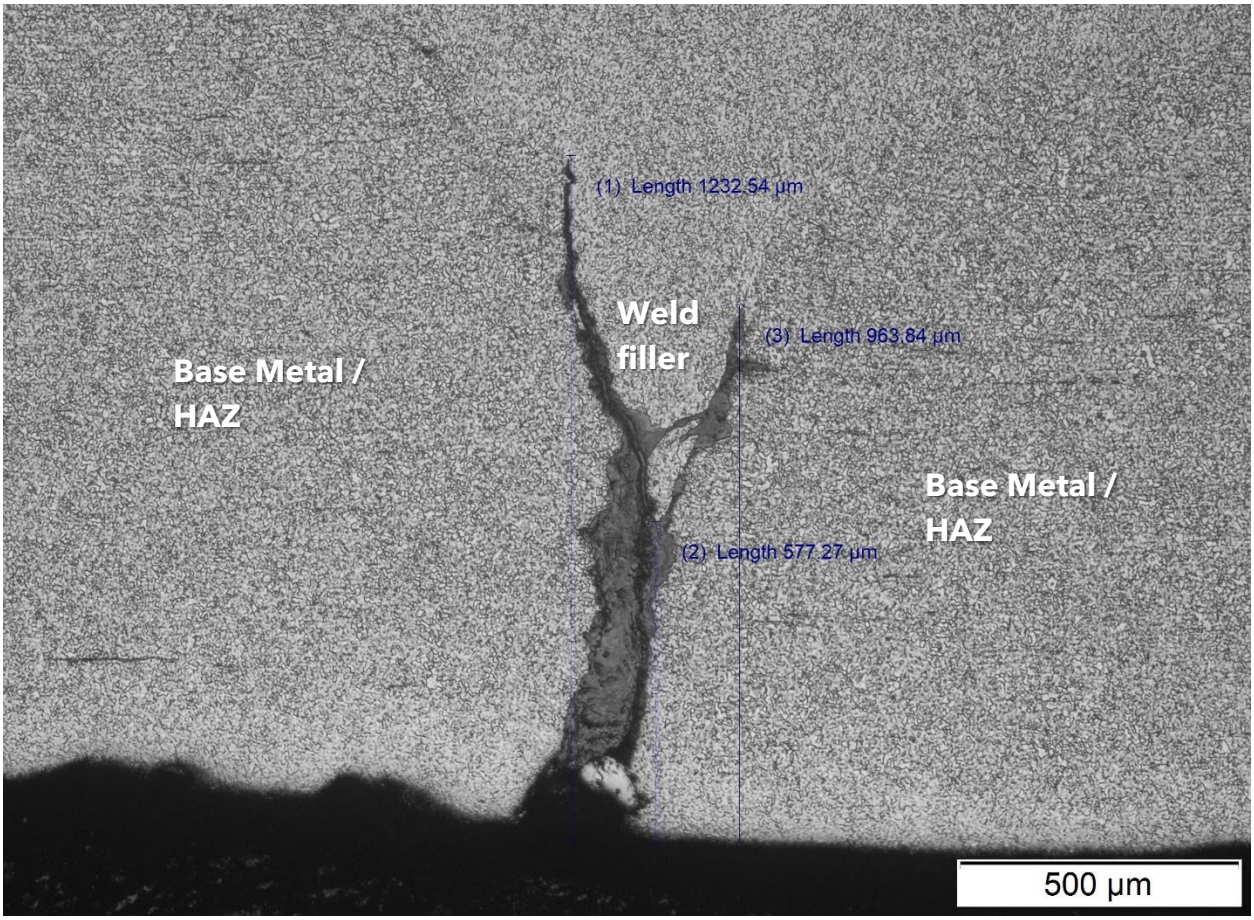

Figure 89. BF optical micrograph of the weld interior and cracking in M3-1, annotated showing distances from the inner diameter surface (~50X, etched 2% Nital).

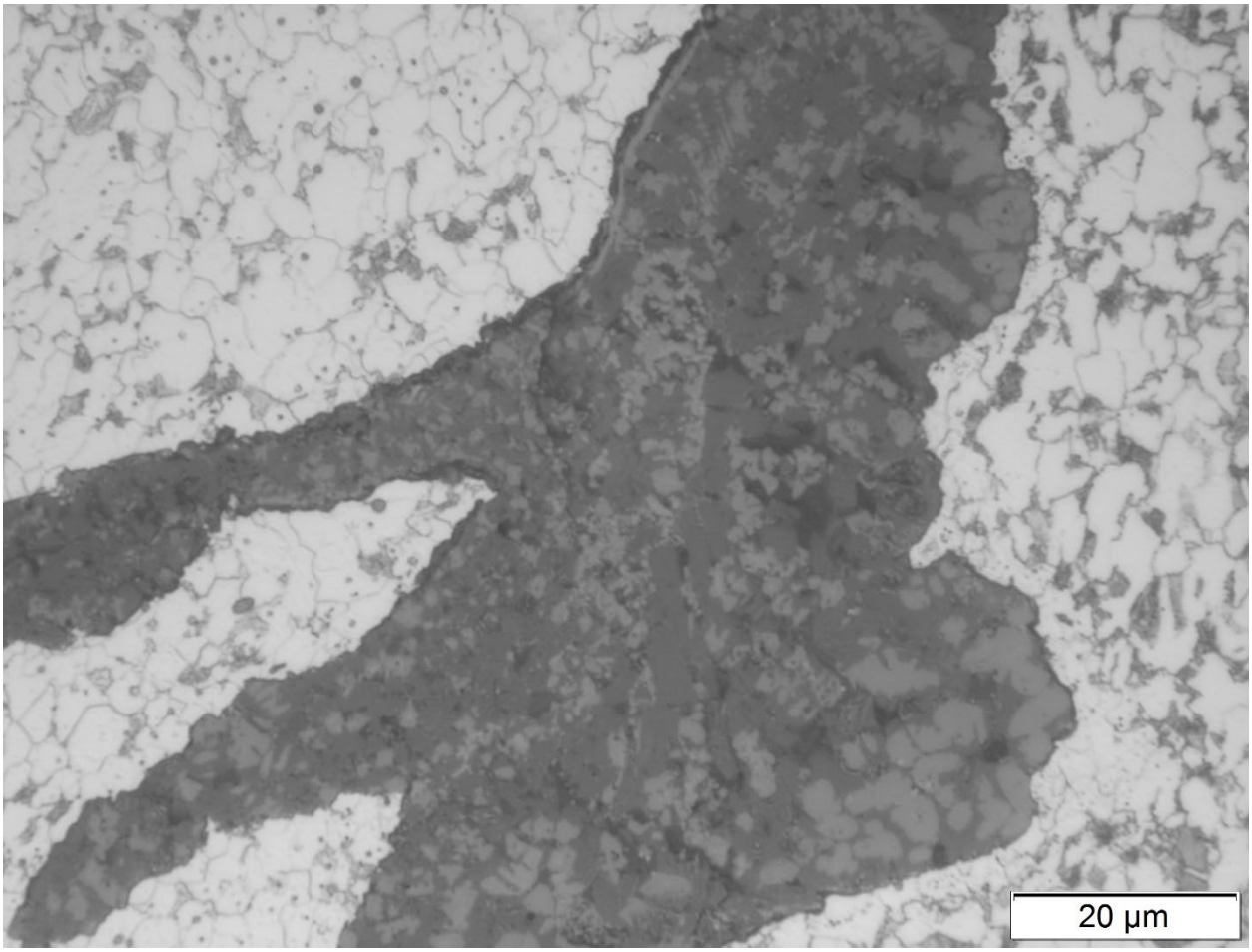

Figure 90. BF optical micrograph of the slag within the crack in Figure 89 (1000X, etched 2% Nital).

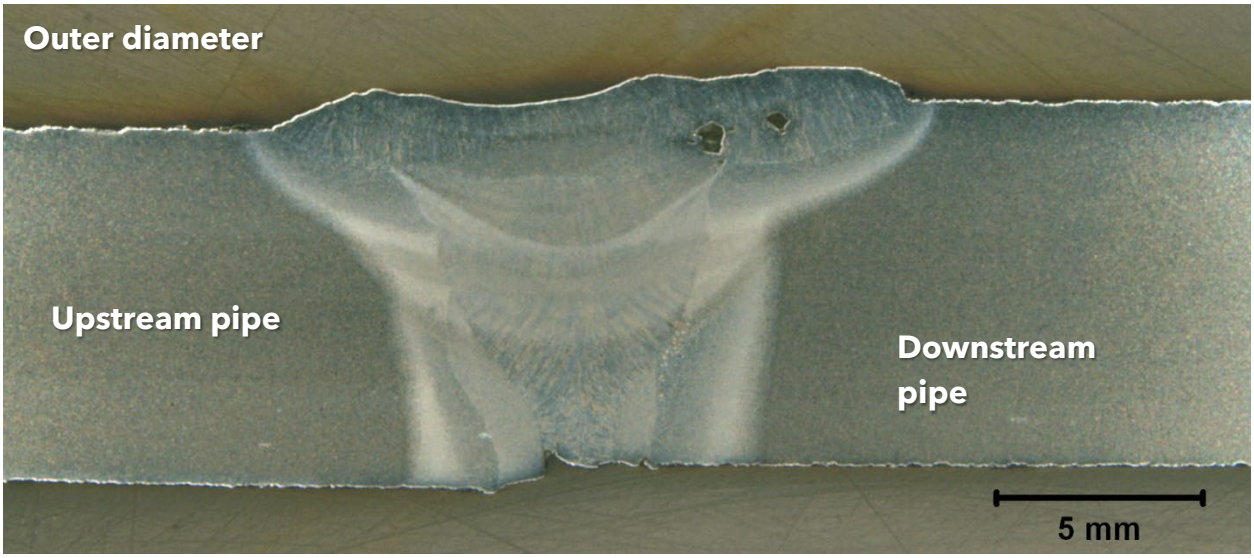

Figure 91. BF optical micrograph of the Pipe 3 girth weld at location M3-2, sectioned 2.08 feet clockwise of top dead center (~5X, etched 2% Nital).

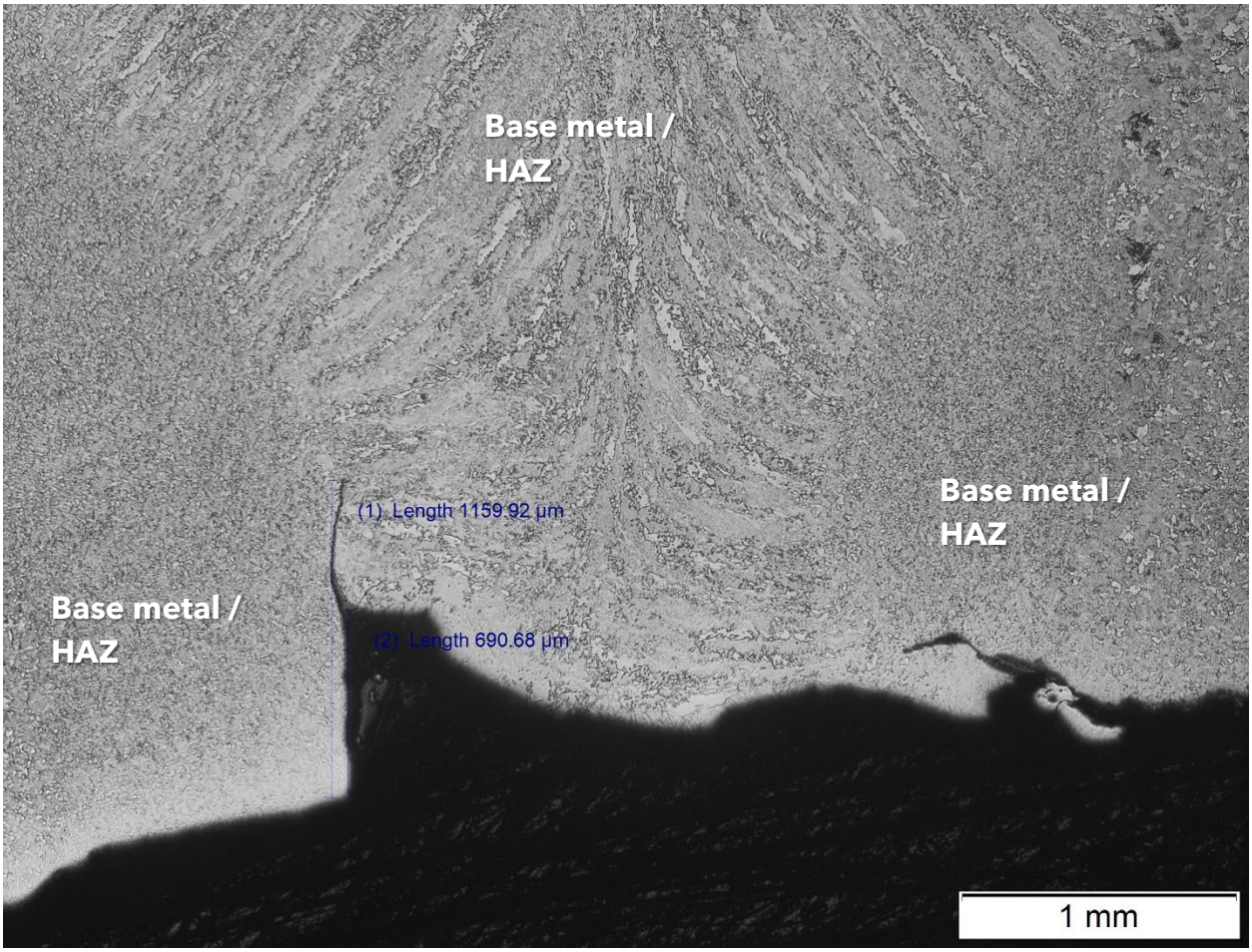

Figure 92. BF optical micrograph of the discontinuity and cracking in M3-2, annotated showing distances from the inner diameter surface (~25X, etched 2% Nital).

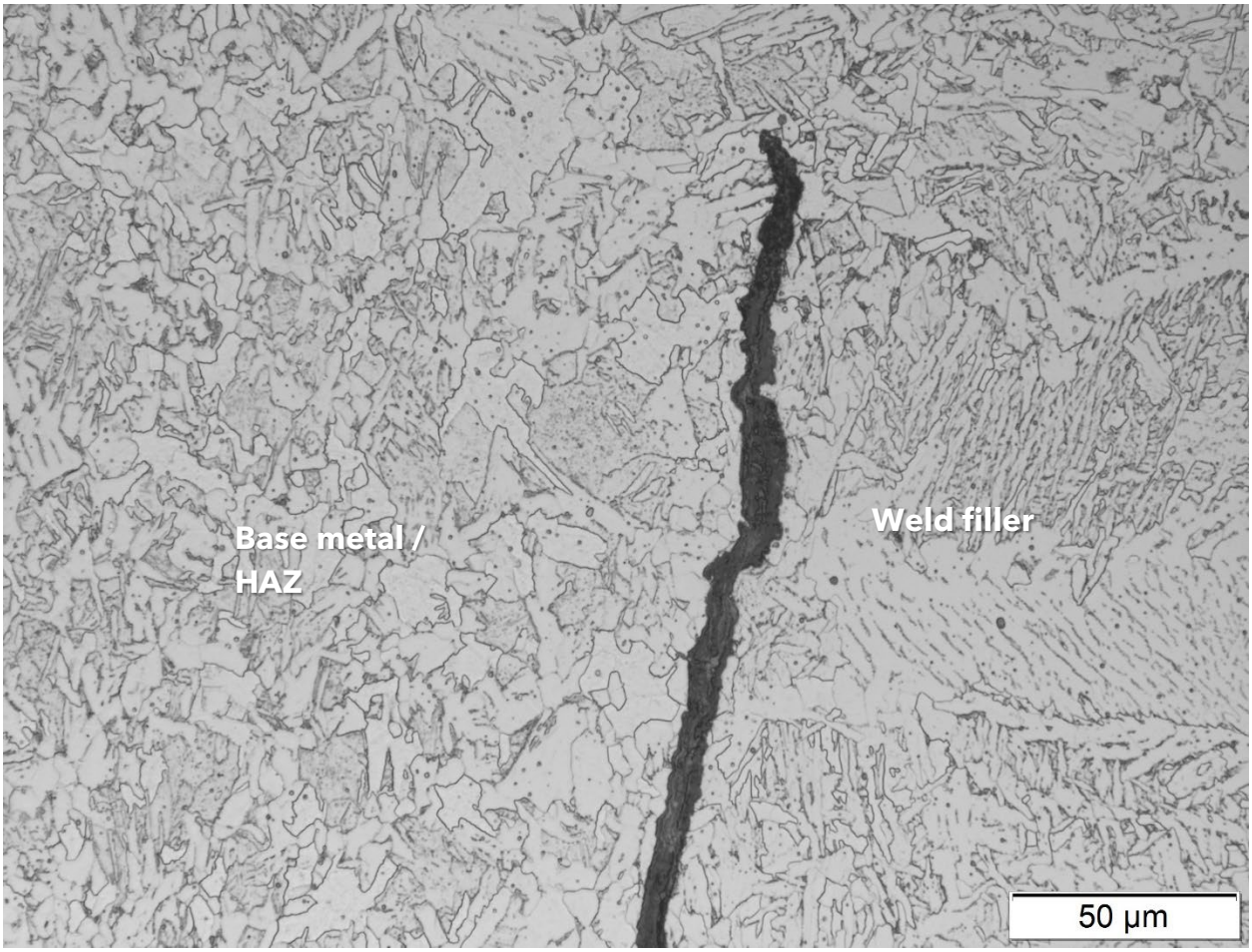

Figure 93. BF optical micrograph of the crack tip from Figure 92 (~400X, etched 2% Nital).

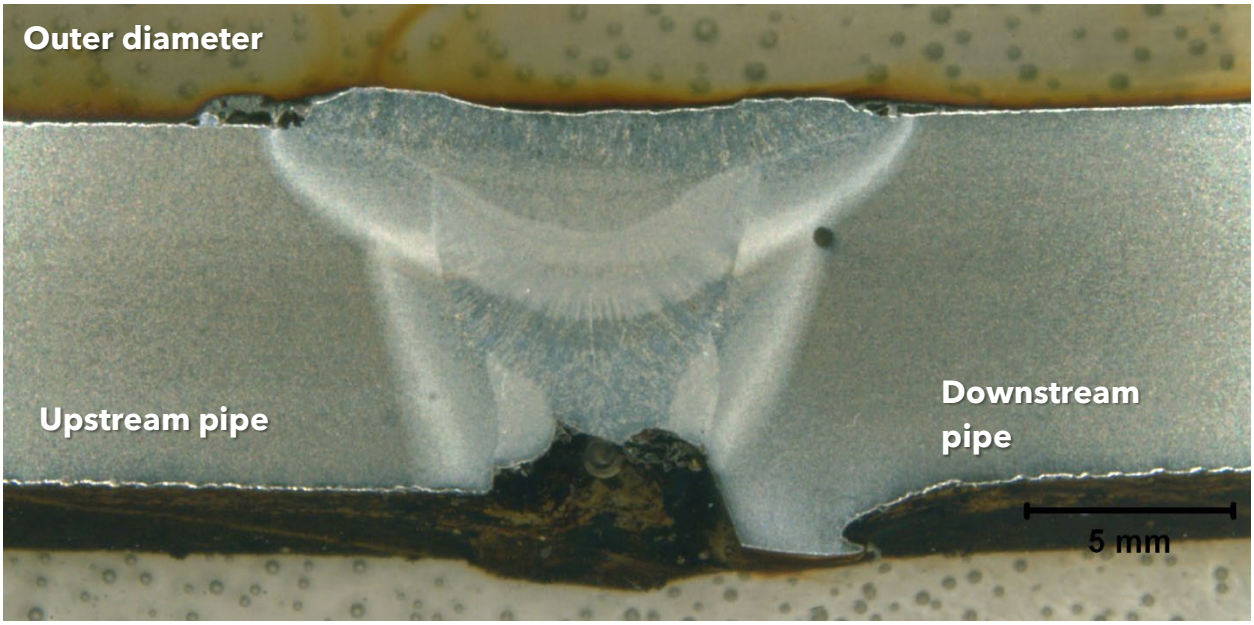

Figure 94. BF optical micrograph of the Pipe 3 girth weld at location M3-5, 4.4 feet clockwise of 12 o'clock (~5X, etched 2% Nital).

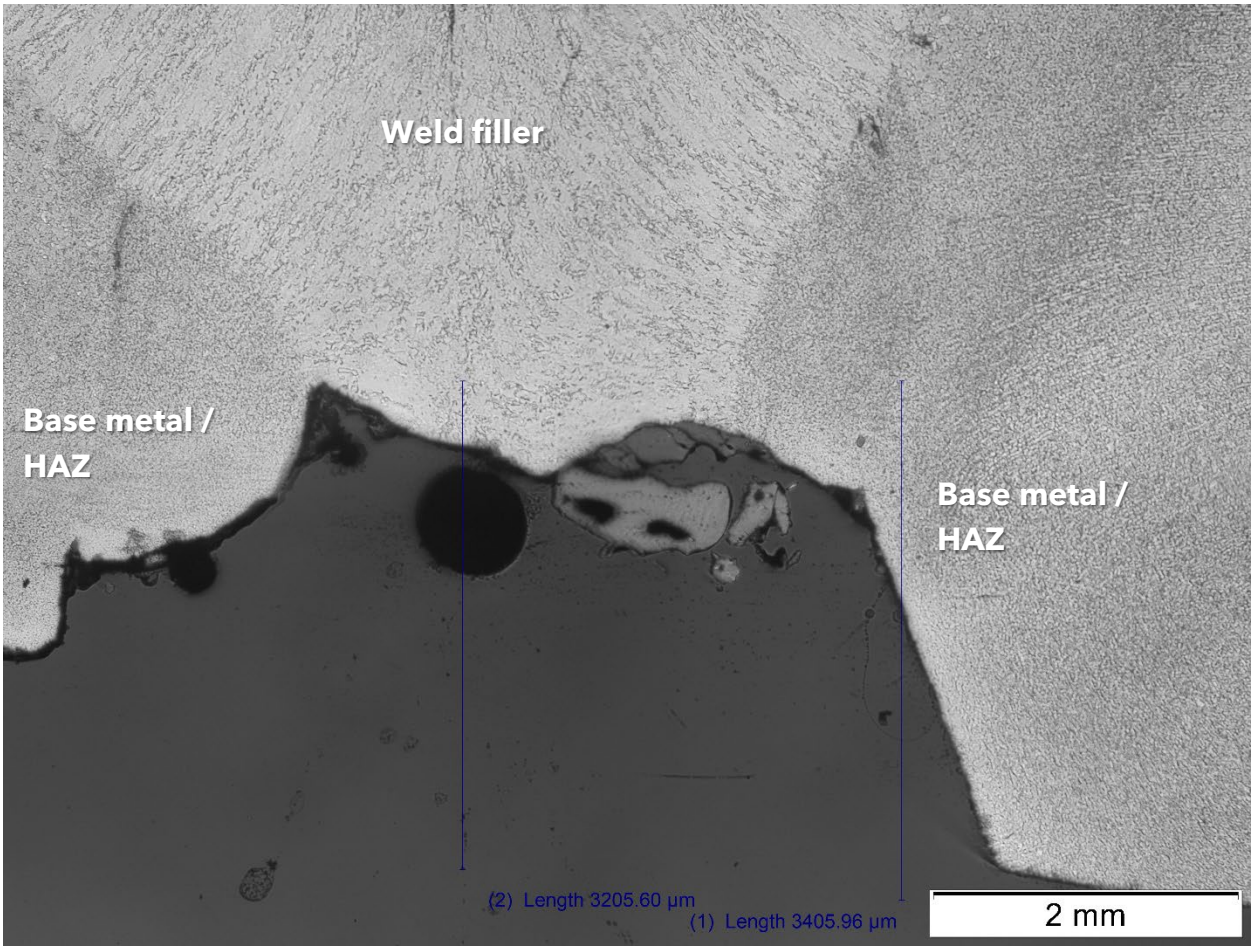

Figure 95. BF optical micrograph of the area of burn through in M3-5, annotated showing distances from the inner diameter surface (~25X, etched 2% Nital).

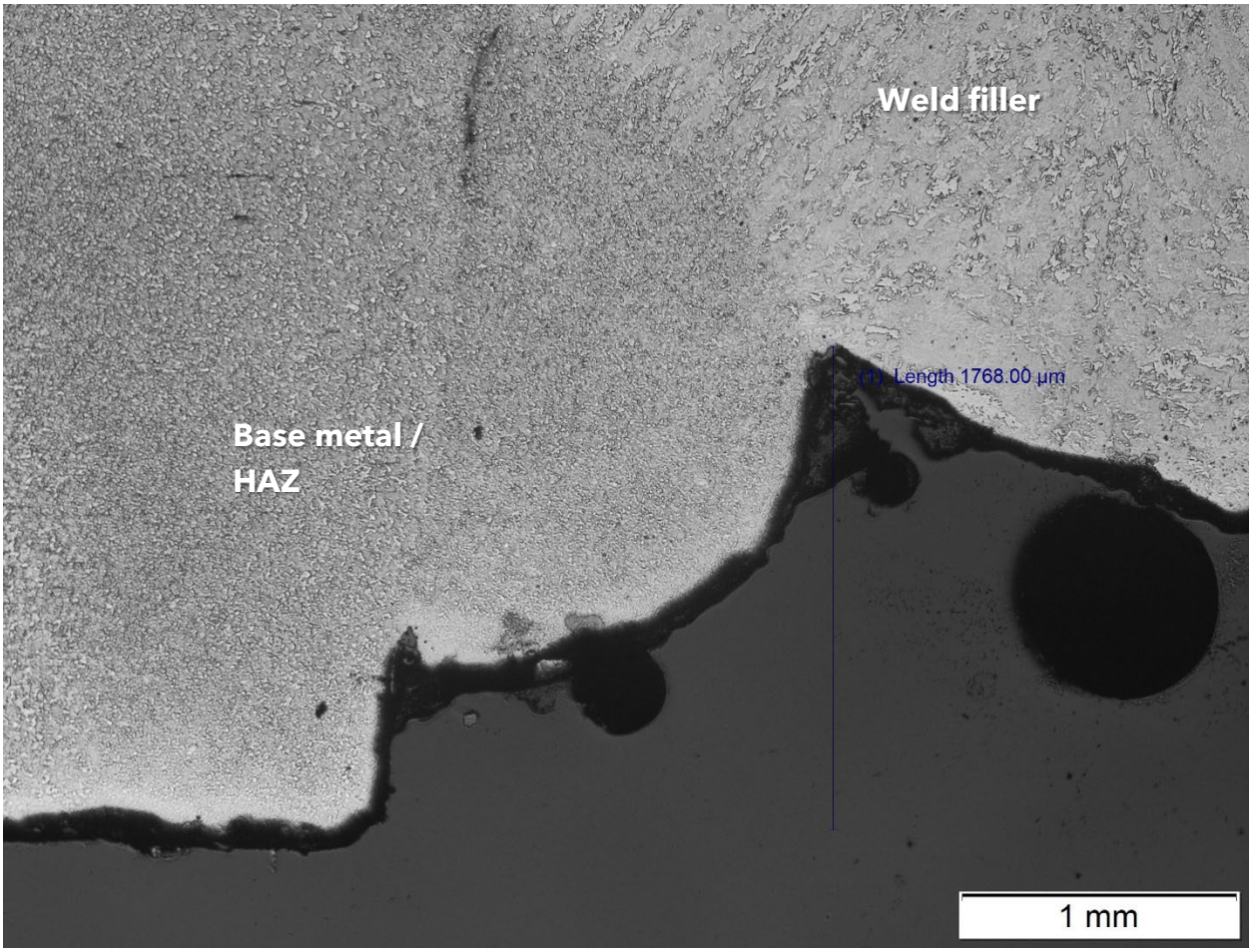

Figure 96. BF optical micrograph of the area of burn through in M3-5, annotated showing distances from the inner diameter surface (~25X, etched 2% Nital).

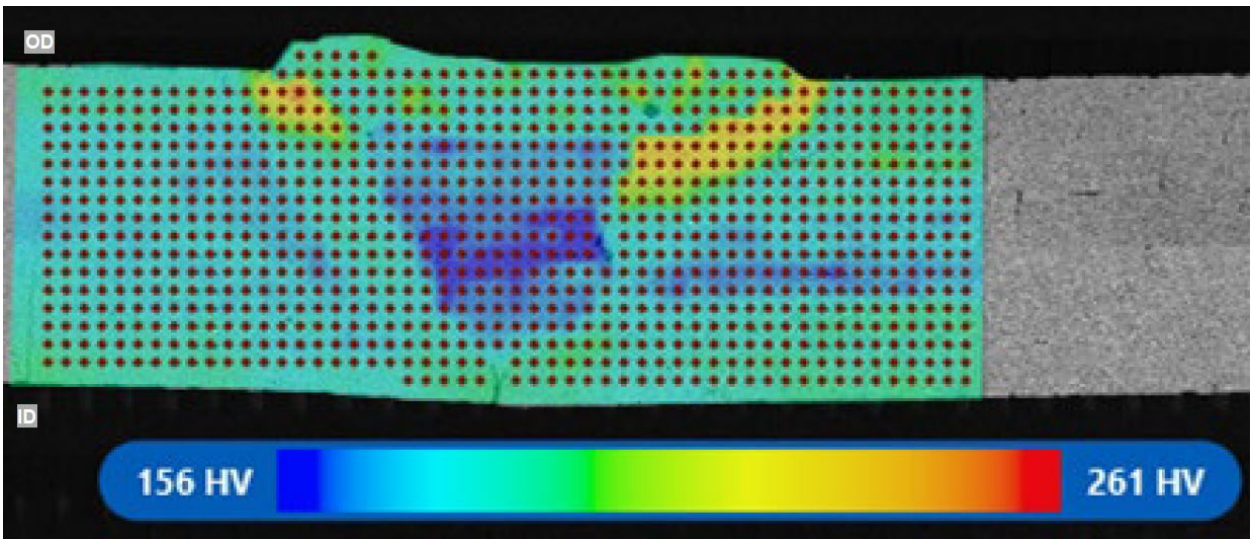

Figure 97. Microindentation hardness map of the girth weld cross section of M3_1, shown in Figure 88, showing values between 156 HV and 261 HV, represented by blue and red colors, respectively.

E. Appendix A – Charpy Impact Testing Results

Table A-1. Results of Charpy V-notch impact tests performed on circumferential base metal specimens removed from PS 1 (JT 29782).

Sample ID	Temperature, °F	Sub Size Impact Energy, ft-lbs	Full Size Impact Energy, ft-lbs	Shear, %	Lateral Expansion, mils
1	-30	3	4.1	0	3
2	-30	3	4.1	0	3
3	-30	4	5.5	0	4
4	32	8	11	10	12
5	32	5	6.9	10	11
6	32	9	12.4	10	15
7	75	14	19.2	50	24
8	75	13	17.8	50	24
9	75	14	19.2	50	24
10	115	22	30.2	70	39
11	115	25	34.3	80	38
12	115	25	34.3	90	42
13	160	29	39.8	100	43
14	160	28	38.4	100	43
15	160	28	38.4	100	44
16	200	28	38.4	100	48
17	200	30	41.2	100	50
18	200	28	38.4	100	40

Table A-2. Results of Charpy V-notch impact tests performed on longitudinal base metal specimens removed from PS 1 (JT 29782).

Sample ID	Temperature, °F	Sub Size Impact Energy, ft-lbs	Full Size Impact Energy, ft-lbs	Shear, %	Lateral Expansion, mils
1	-50	3	4.1	0	2
2	-50	2	2.7	0	1
3	-50	2	2.7	0	1
4	32	18	24.5	15	25
5	32	17	23.1	15	24
6	32	15	20.4	10	22
7	75	25	34	40	36
8	75	25	34	40	33
9	75	32	43.5	50	43
10	115	44	59.8	65	61
11	115	43	58.4	60	54
12	115	42	57.1	65	58
13	160	56	76.1	100	77
14	160	56	76.1	100	78
15	160	58	78.8	100	77
16	200	58	78.8	100	76
17	200	57	77.4	100	77
18	200	56	76.1	100	76

Table A-3. Results of Charpy V-notch impact tests performed on circumferential seam weld (bond line [BL] notch) specimens removed from PS 1 (JT 29782).

Sample ID	Temperature, °F	Sub Size Impact Energy, ft-lbs	Full Size Impact Energy, ft-lbs	Shear, %	Lateral Expansion, mils
1	32	3	4.1	0	3
2	32	3	4.1	0	4
3	32	7	9.6	0	12
4	115	13	17.8	30	23
5	115	10	13.7	30	19
6	115	14	19.2	35	25
7	140	14	19.2	60	23
8	140	12	16.5	30	20
9	140	10	13.7	30	15
10	170	15	20.6	70	25
11	170	13	17.8	70	25
12	170	11	15.1	50	17
13	200	22	30.2	80	37
14	200	23	31.6	85	40
15	200	23	31.6	90	37
16	230	19	26.1	100	33
17	230	21	28.8	100	32
18	230	20	27.5	100	28

Table A-4. Results of Charpy V-notch impact tests performed on circumferential seam weld (heat affected zone [HAZ] notch) specimens removed from PS 1 (JT 29782).

Sample ID	Temperature, °F	Sub Size Impact Energy, ft-lbs	Full Size Impact Energy, ft-lbs	Shear, %	Lateral Expansion, mils
1	-40	10	13.8	5	10
2	-40	9	12.4	5	9
3	-40	10	13.8	5	9
4	32	8	11.1	15	15
5	32	11	15.2	10	12
6	32	11	15.2	15	19
7	55	11	15.2	20	14
8	55	11	15.2	20	16
9	55	12	16.6	25	20
10	85	11.5	15.9	25	20
11	85	13	18	30	21
12	85	11	15.2	20	17
13	115	27	37.3	100	43
14	115	25	34.6	90	40
15	115	28	38.7	100	45
16	200	27	37.3	100	46
17	200	26	35.9	100	45
18	200	27	37.3	100	45

Table A-5. Results of analyses of the Charpy V-notch impact energy and percent shear plots for circumferential base metal, longitudinal base metal, seam weld (BL notch), and seam weld (HAZ notch) specimens removed from PS 1 (JT 29782).

	Circumferential Base Metal	Longitudinal Base Metal	Circumferential Seam Weld (BL notch)	Circumferential Seam Weld (HAZ notch)
Upper Shelf Impact Energy (Full Size), Ft-lbs	38.9	73.4	29.7	36.9
85% FATT, °F	118	140	202	108
85% FATT, °F (Full Scale Pipe) [1]	106	127	190	96.0

1 Full Scale Pipe FATT = 85% FATT + ((66*($t_w^{0.55}$/$t_c^{0.7}$)-100) where t_w = pipe wall thickness and t_c = width of the CVN specimen. W. A. Maxey, J. F. Kiefner, R. J. Eiber, Brittle Fracture Arrest in Gas Pipelines," NG-18 Report No. 135, A.G.A. Catalog No. L51436, April 1983, Battelle Columbus Laboratories. Rosenfeld, M.J., "A Simple Procedure for Synthesizing Charpy Impact Energy Transition Curves from Limited Test Data," International Pipeline Conference, Volume 1, ASME, 1996, Equation 1.

Table A-6. Results of Charpy V-notch impact tests performed on circumferential base metal specimens removed from PS 2 (JT 29783).

Sample ID	Temperature, °F	Sub Size Impact Energy, ft-lbs	Full Size Impact Energy, ft-lbs	Shear, %	Lateral Expansion, mils
1	-30	2.5	3.5	0	2
2	-30	3	4.2	0	2
3	-30	4	5.6	0	4
4	32	7	9.8	15	10
5	32	5	7	15	11
6	32	5	7	15	9
7	75	12.5	17.5	40	21
8	75	11	15.4	30	21
9	75	12	16.8	35	19
10	115	21	29.3	80	34
11	115	18	25.1	80	31
12	115	17	23.8	65	30
13	160	25	34.9	95	40
14	160	25	34.9	95	37
15	160	25	34.9	95	40
16	200	25	34.9	100	42
17	200	26	36.3	100	43
18	200	26	36.3	100	44

Table A-7. Results of Charpy V-notch impact tests performed on longitudinal base metal specimens removed from PS 2 (JT 29783).

Sample ID	Temperature, °F	Sub Size Impact Energy, ft-lbs	Full Size Impact Energy, ft-lbs	Shear, %	Lateral Expansion, mils
1	-30	4	5.8	5	4
2	-30	4.5	6.6	5	7
3	-30	3	4.4	5	3
4	32	7	10.2	10	13
5	32	4	5.8	10	10
6	32	4	5.8	10	8
7	75	18	26.3	30	26
8	75	13	19	25	20
9	75	20	29.2	30	30
10	115	35	51.1	80	50
11	115	33	48.2	75	51
12	115	39	56.9	90	54
13	160	44	64.2	95	63
14	160	43	62.7	95	61
15	160	41	59.8	90	60
16	200	44	64.2	100	64
17	200	42	61.3	100	62
18	200	43	62.7	100	65

Table A-8. Results of Charpy V-notch impact tests performed on circumferential seam weld (bond line notch) specimens removed from PS 2 (JT 29783).

Sample ID	Temperature, °F	Sub Size Impact Energy, ft-lbs	Full Size Impact Energy, ft-lbs	Shear, %	Lateral Expansion, mils
1	32	3	4.3	5	5
2	32	2	2.8	5	5
3	32	2	2.8	5	3
4	115	11	15.6	20	20
5	115	10	14.2	20	19
6	115	7	10	20	17
7	140	12	17.1	30	20
8	140	14.5	20.6	30	25
9	140	13	18.5	30	20
10	170	16	22.8	70	29
11	170	15	21.3	60	21
12	170	16	22.8	80	27
13	200	19	27	80	31
14	200	19	27	90	34
15	200	18	25.6	70	32
16	240	16	22.8	100	30
17	240	18	25.6	100	32
18	240	16	22.8	100	30

Table A-9. Results of Charpy V-notch impact tests performed on circumferential seam weld (HAZ notch) specimens removed from PS 2 (JT 29783).

Sample ID	Temperature, °F	Sub Size Impact Energy, ft-lbs	Full Size Impact Energy, ft-lbs	Shear, %	Lateral Expansion, mils
1	-40	7	9.7	0	7
2	-40	9	12.4	0	9
3	-40	3.5	4.8	0	2
4	32	10	13.8	10	16
5	32	12	16.6	10	17
6	32	10	13.8	10	15
7	115	17	23.5	50	33
8	115	15	20.7	40	27
9	115	15	20.7	40	25
10	140	31	42.9	100	44
11	140	30	41.5	100	47
12	140	30	41.5	100	46
13	170	28	38.7	100	44
14	170	29	40.1	100	46
15	170	29	40.1	100	47
16	200	24	33.2	100	44
17	200	27	37.3	100	44
18	200	26	35.9	100	43

Table A-10. Results of analyses of the Charpy V-notch impact energy and percent shear plots for circumferential base metal, longitudinal base metal, seam weld (BL notch), and seam weld (HAZ notch) specimens removed from PS 2 (JT 29783).

	Circumferential Base Metal	Longitudinal Base Metal	Circumferential Seam Weld (BL notch)	Circumferential Seam Weld (HAZ notch)
Upper Shelf Impact Energy (Full Size), Ft-lbs	34.0	63.0	24.4	39.0
85% FATT, °F	133	123	200	122
85% FATT, °F (Full Scale Pipe) [1]	122	115	190	111

1 Full Scale Pipe FATT = 85% FATT + ((66*($t_w^{0.55}$/$t_c^{0.7}$)-100) where t_w = pipe wall thickness and t_c = width of the CVN specimen. W. A. Maxey, J. F. Kiefner, R. J. Eiber, Brittle Fracture Arrest in Gas Pipelines," NG-18 Report No. 135, A.G.A. Catalog No. L51436, April 1983, Battelle Columbus Laboratories. Rosenfeld, M.J., "A Simple Procedure for Synthesizing Charpy Impact Energy Transition Curves from Limited Test Data," International Pipeline Conference, Volume 1, ASME, 1996, Equation 1.

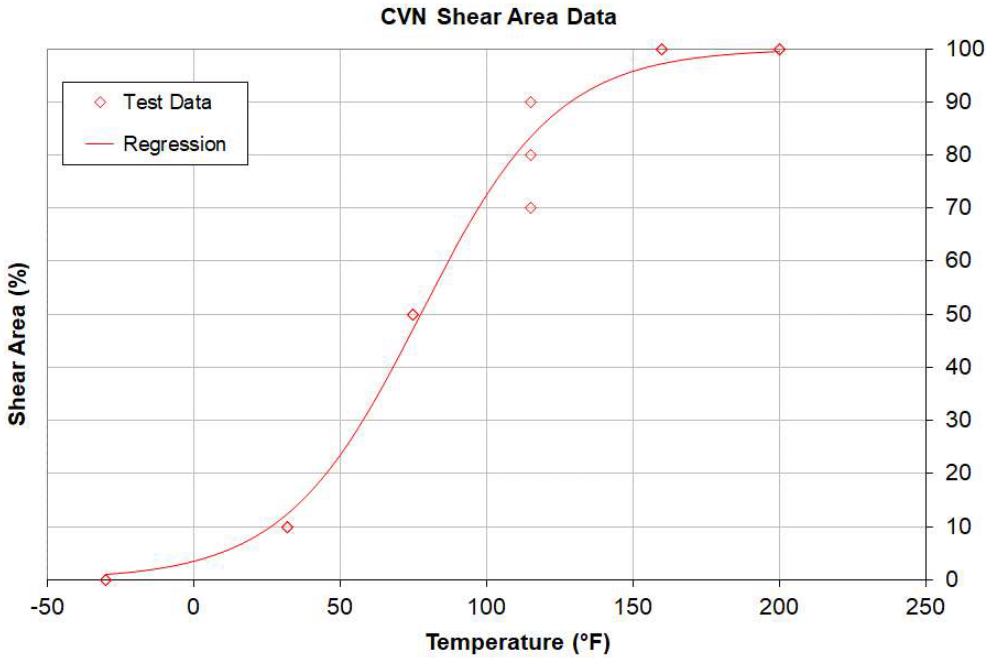

Figure A-1. Percent shear from Charpy V-notch tests as a function of temperature for circumferential base metal specimens removed from JT 29782 of PS 1.

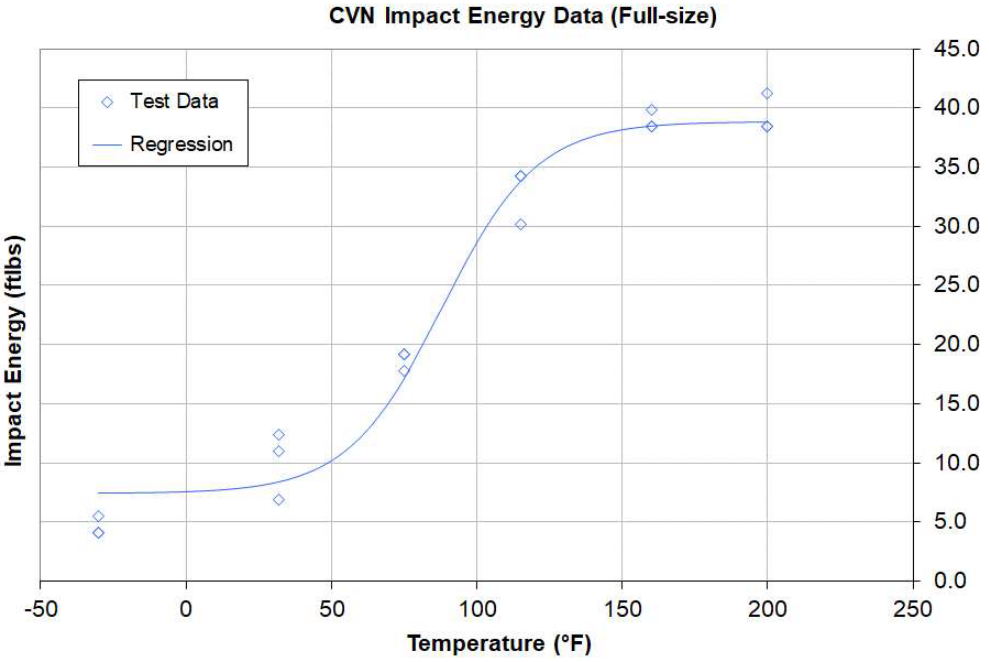

Figure A-2. Charpy V-notch impact energy as a function of temperature for circumferential base metal specimens removed from JT 29782 of PS 1.

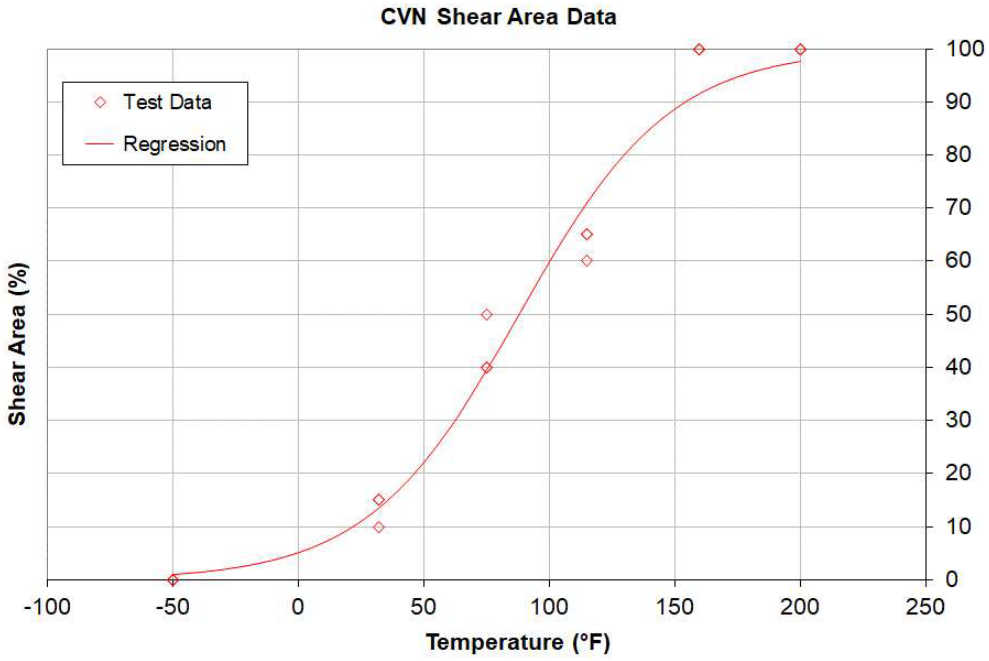

Figure A-3. Percent shear from Charpy V-notch tests as a function of temperature for longitudinal base metal specimens removed from JT 29782 of PS 1.

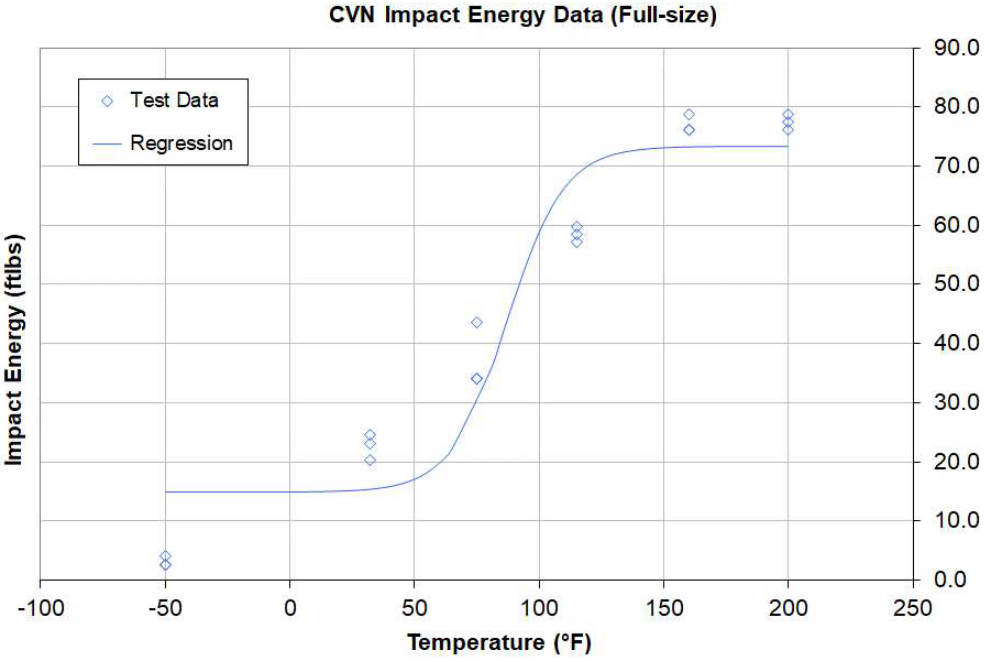

Figure A-4. Charpy V-notch impact energy as a function of temperature for longitudinal base metal specimens removed from JT 29782 of PS 1.

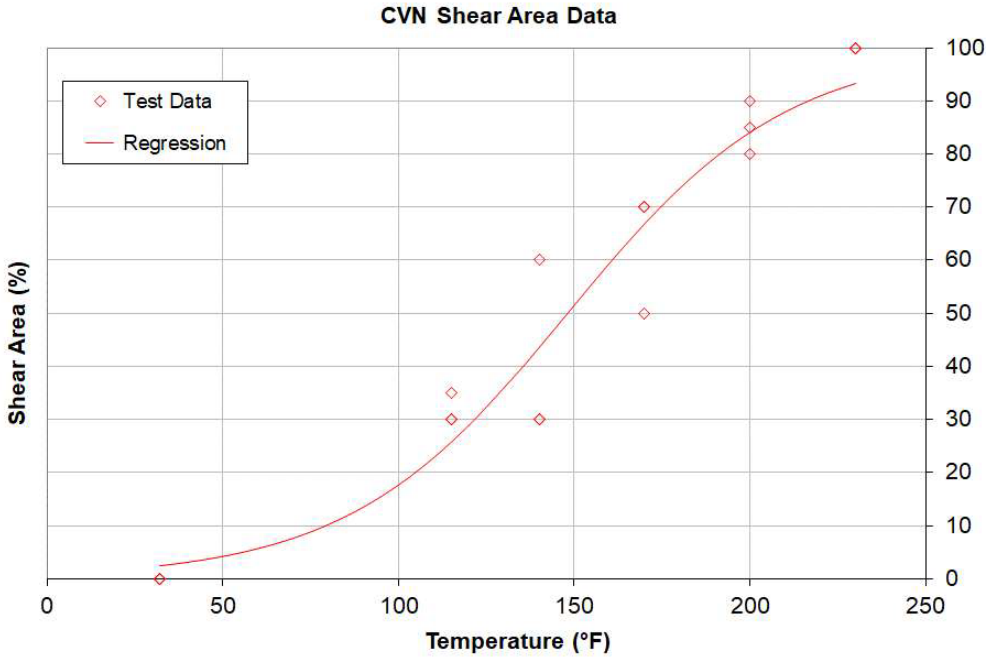

Figure A-5. Percent shear from Charpy V-notch tests as a function of temperature for circumferential seam weld (bond line notch) specimens removed from JT 29782 of PS 1.

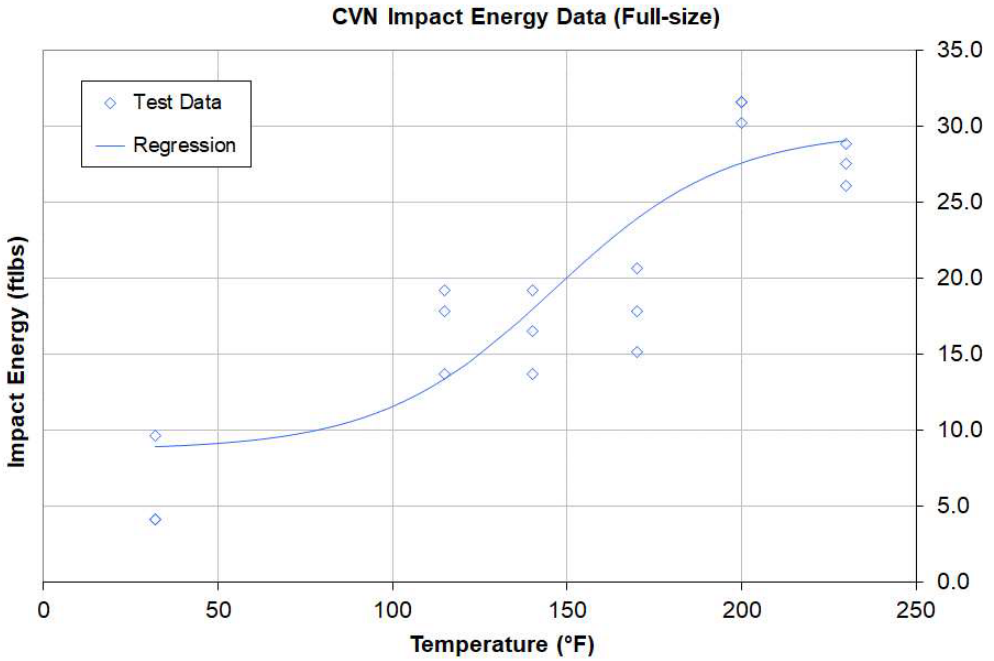

Figure A-6. Charpy V-notch impact energy as a function of temperature for circumferential seam weld (bond line notch) specimens removed from JT 29782 of PS 1.

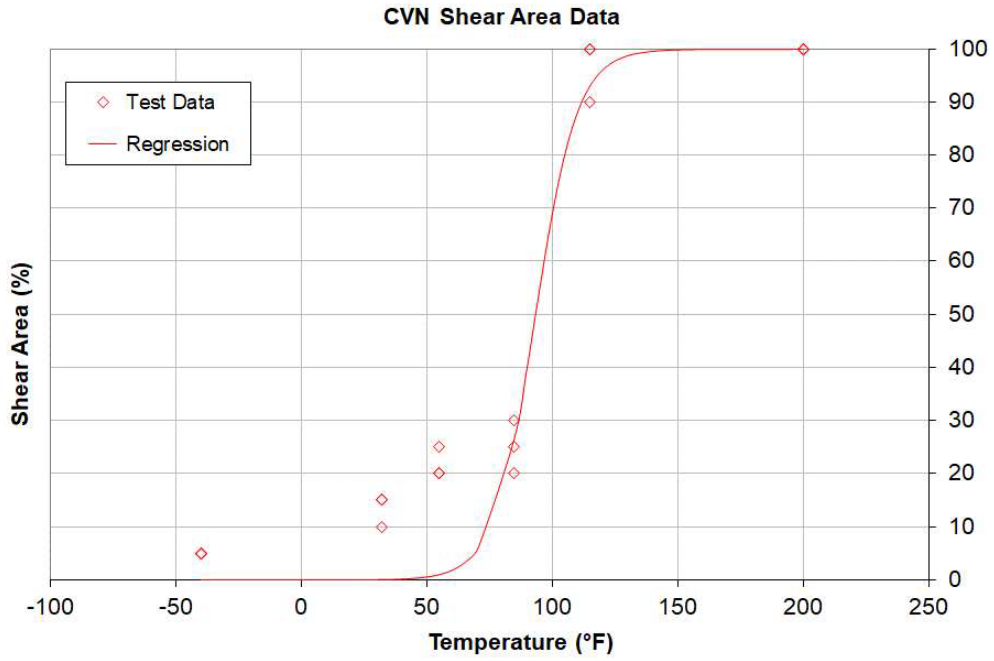

Figure A-7. Percent shear from Charpy V-notch tests as a function of temperature for circumferential seam weld (HAZ notch) specimens removed from JT 29782 of PS 1.

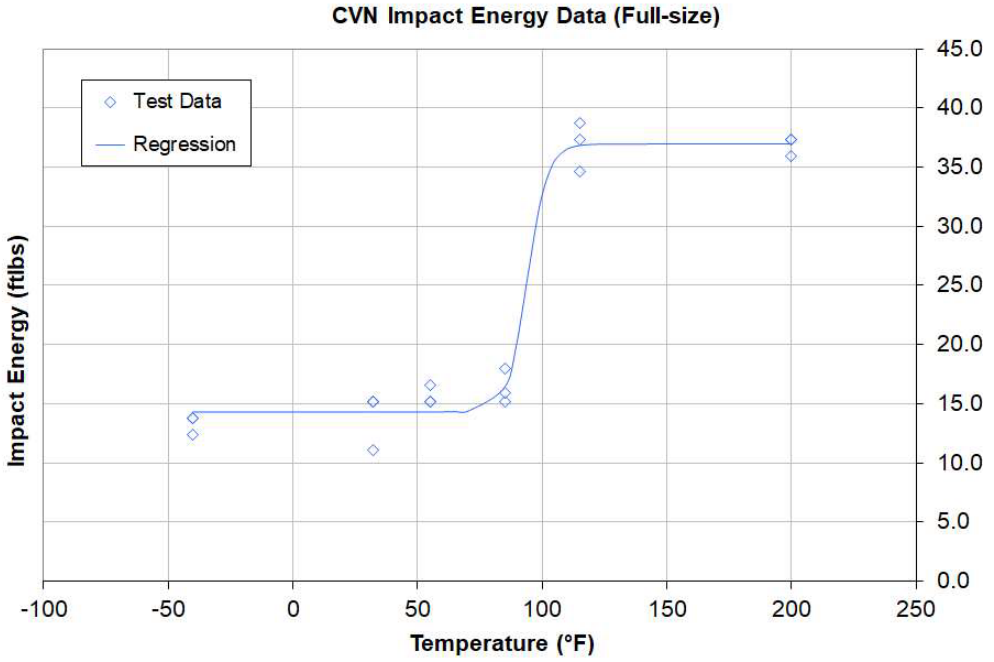

Figure A-8. Charpy V-notch impact energy as a function of temperature for circumferential seam weld (HAZ notch) specimens removed from JT 29782 of PS 1.

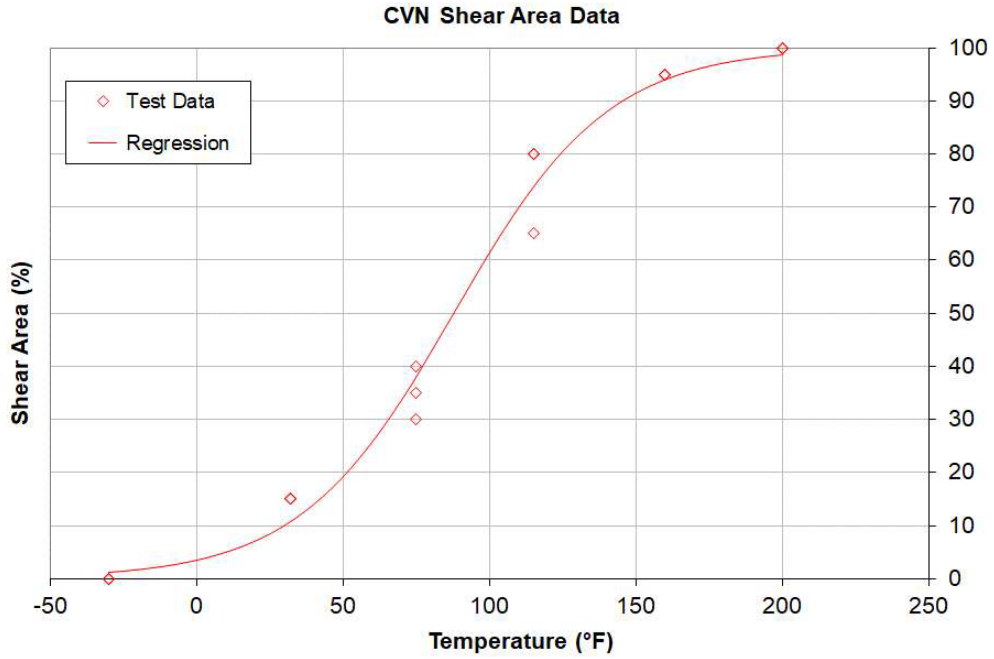

Figure A-9. Percent shear from Charpy V-notch tests as a function of temperature for circumferential base metal specimens removed from JT 29783 of PS 2.

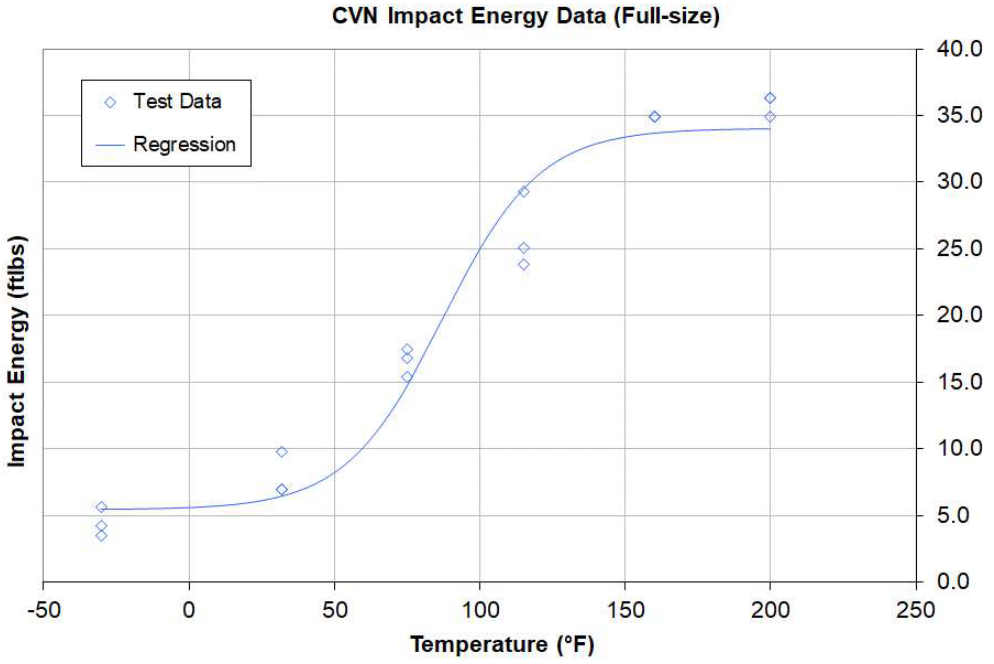

Figure A-10. Charpy V-notch impact energy as a function of temperature for circumferential base metal specimens removed from JT 29783 of PS 2.

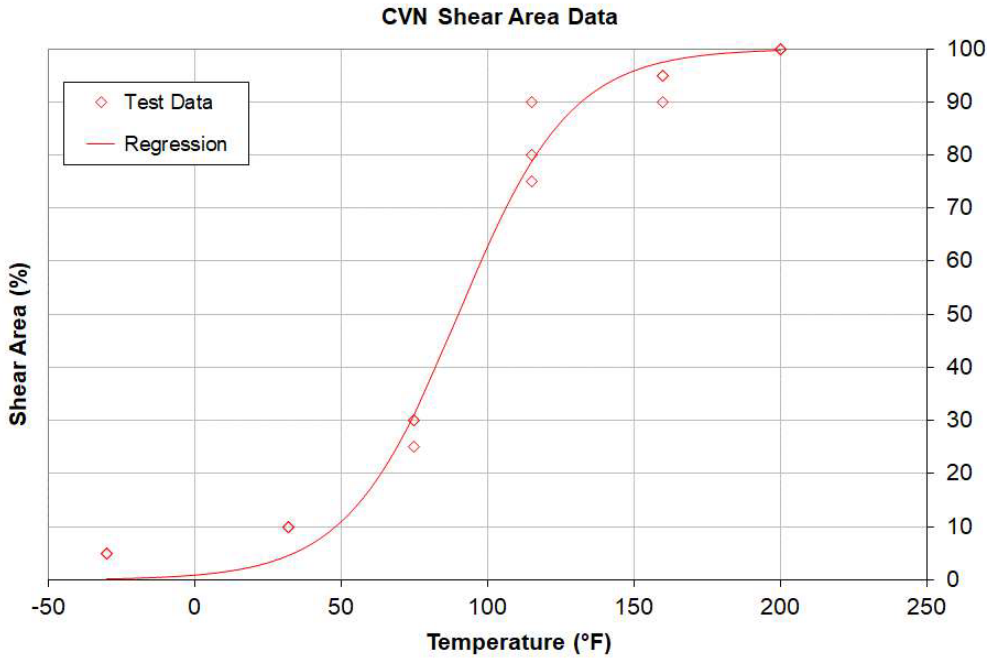

Figure A-11. Percent shear from Charpy V-notch tests as a function of temperature for longitudinal base metal specimens removed from JT 29783 of PS 2.

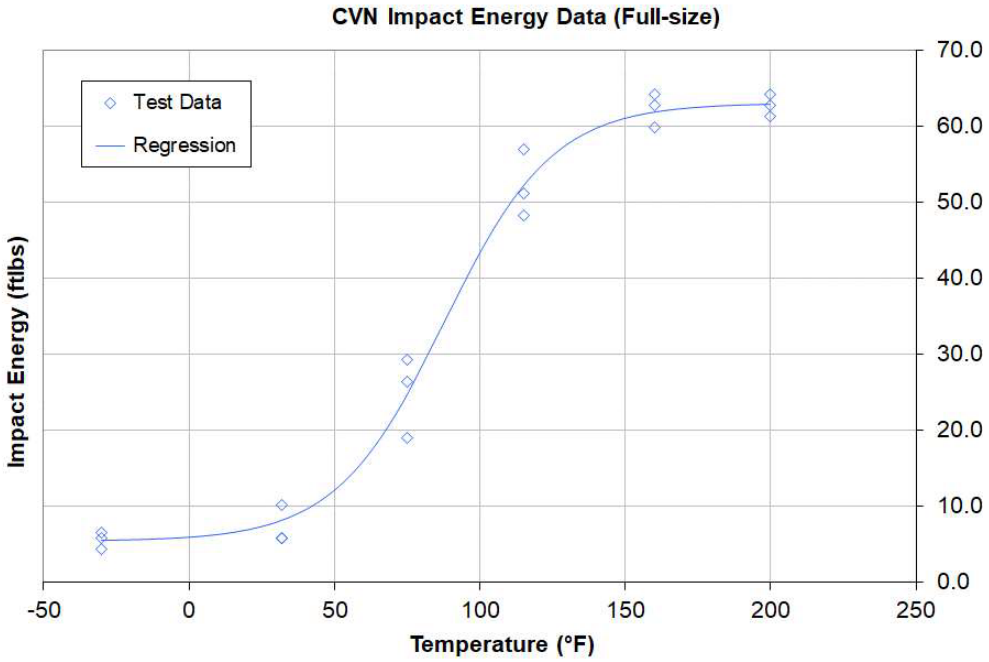

Figure A-12. Charpy V-notch impact energy as a function of temperature for longitudinal base metal specimens removed from JT 29783 of PS 2.

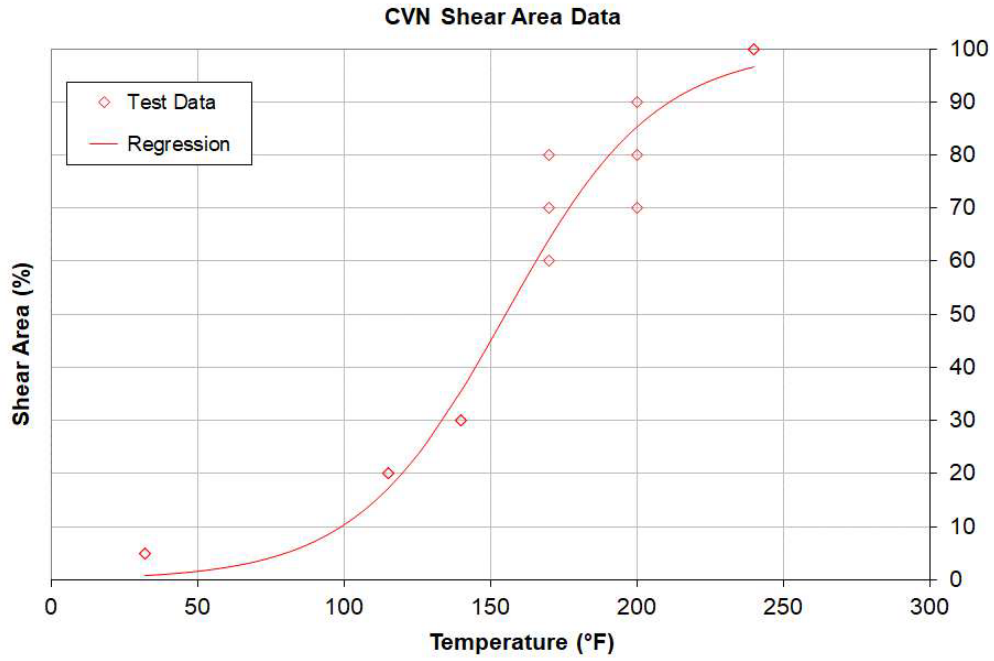

Figure A-13. Percent shear from Charpy V-notch tests as a function of temperature for circumferential seam weld (bond line notch) specimens removed from JT 29783 of PS 2.

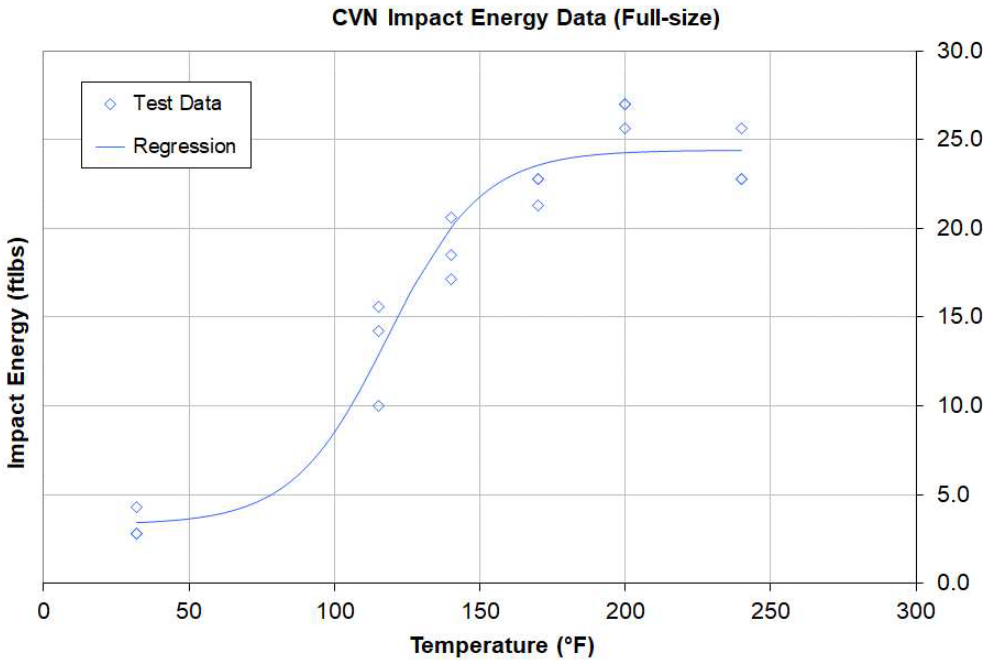

Figure A-14. Charpy V-notch impact energy as a function of temperature for circumferential seam weld (bond line notch) specimens removed from JT 29783 of PS 2.

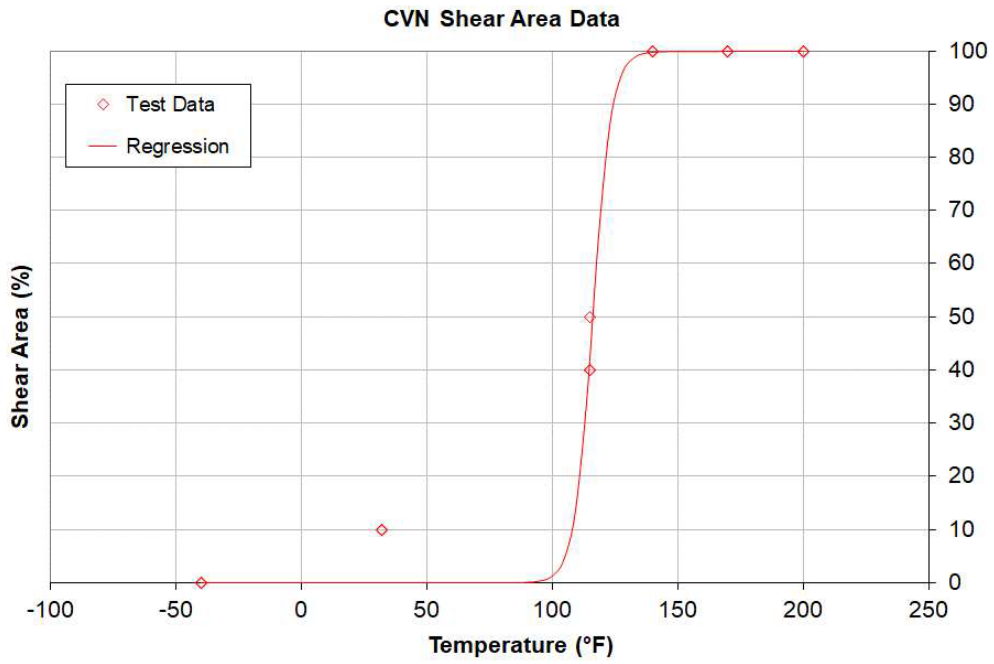

Figure A-15. Percent shear from Charpy V-notch tests as a function of temperature for circumferential seam weld (HAZ notch) specimens removed from JT 29783 of PS 2.

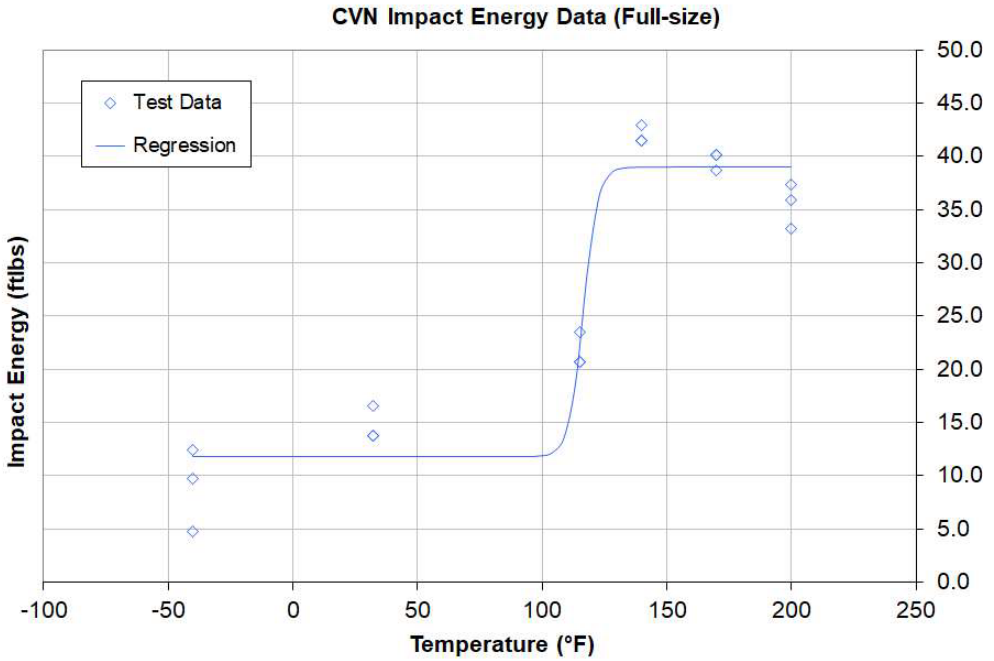

Figure A-16. Charpy V-notch impact energy as a function of temperature for circumferential seam weld (HAZ notch) specimens removed from JT 29783 of PS 2.